Doctoral Dissertation

Observational studies of auroras using commercial digital cameras

商用デジタルカメラを用いたオーロラの観測的研究

Sota Nanjo

Graduate School of Informatics and Engineering,

The University of Electro-Communications

January, 2024

Abstract

This thesis describes the evaluation of the performance of commercial digital cameras as an optical instrument for scientific studies of auroras, the development of automated observation methods synchronized with auroral appearances, and case studies derived from the developed observation methods. The commercial digital cameras used in this thesis are Nikon D5 and Sony α7SIII. For both cameras, optical calibration experiments at the National Institute of Polar Research have been conducted to estimate the transmission characteristics of the color filters and to evaluate the linearity of the RGB counts from the digital cameras to the incident light intensity.

The Nikon D5 is aboard the International Space Station (ISS) and occasionally takes continuous images (temporal resolution is 0.5–1.0 sec) of auroras for outreach purposes. These observations enable visualization of large areas of several thousand kilometers with high temporal and spatial resolutions, which has not been carried out by typical ground-based and satellite observations. In Chapter 2, we analyze cases of such ISS observations in which pulsating auroras (PsAs) were observed from the midnight to the morning side. The result shows that the color of the PsAs becomes whitish, i.e., the count ratio in the B and G channels increases in the morning side. Since previous studies have indicated that the average energy of electrons responsible for PsAs (PsA electrons) is higher in this local time sector, the result suggests that the average energy of the PsA electrons can be estimated from the B/G ratio in the digital image of PsAs.

For quantitative evaluation of the correspondence between the B/G ratio and the average energy of the auroral electrons, it is necessary to measure the relationship between the auroral color and the characteristics of auroral electrons simultaneously and then derive an empirical model. Since there is no measurement of auroral electrons onboard ISS, we have installed Nikon D5 at the Ramfjordmoen observatory near Tromsø, Norway, where the EISCAT radar, which can estimate the average energy of the electrons, was installed and was reproduced ISS observations on the ground. Chapter 3 describes the methodology of simultaneous observations and the results obtained from the observations. To clone the high temporal resolution of 0.5–1.0 seconds operated onboard the ISS, it

is suitable to take photographs only during the auroral appearance. Such an effort also enables us to reduce the wear and tear of the shutter unit as much as possible and to obtain more data. For this purpose, a deep learning model was created to automatically detect an aurora from images taken by the all-sky camera installed at the same observatory. Following the notification from this automated detection system, the shutter of the Nikon D5 is released only during the auroral appearance. Then, we compared the RGB values with the Rayleigh values measured by the photometer installed at the same observatory. The results showed positive correlations within a standard deviation between counts in the B and G channels of the Nikon D5 and the Rayleigh values at 427.8 nm and 557.7 nm from the photometer, respectively, and then the B/G ratio was correlated with the intensity ratio at 427.8 nm and 557.7 nm. The final goal of this research project is to estimate the average energy of the auroral electrons from the B/G ratio, but it is still halfway because we were unable to obtain an example of simultaneous observations by the EISCAT radar and the Nikon D5.

When the observations were made at the Ramfjordmoen field station with the Nikon D5, the still imagings were chosen to follow the settings of the digital camera observations from ISS. In Chapter 4, we took videos of auroras at the Swedish Institute of Spece Physics (IRF) in Kiruna, Sweden, to evaluate whether commercial digital cameras can visualize the fast temporal variations in auroras. To improve not only the temporal resolution but also the spatial resolution, a wide-angle lens (angle of view $\sim$70 degrees) was used instead of a fisheye lens. Since it is impossible to observe the entire sky with a wide-angle lens, we need to point the camera in the direction of the aurora to accumulate data efficiently. For this purpose, a model was created to detect the direction of auroral appearance from images taken by the all-sky camera at the IRF. The camera, Sony α7SIII, was installed on a gimbal, and the direction of the camera was controlled by operating the gimbal with a computer. Only lightweight and compact commercial digital cameras can be used in this system because a professional camera cannot be mounted on the gimbal due to its large volume and mass. This technique makes it possible to capture the characteristics of a short-lived aurora in a narrow region with high spatial and temporal resolutions. As one such example, we will present a case of the shock aurora, in which the automated digital camera observation visualized its propagation towards the nightside. In addition,

comparing observational results and the results of optical calibration experiments, we have revealed that Sony α7SIII can visualize fast ($\sim$3 Hz) internal modulations of PsAs.

The presence of the fast modulation in PsA may help to infer the dynamics of the magnetospheric plasma. To investigate the scientific value of the use of commercial digital cameras for detecting the internal modulation of the PsAs, we introduce a simultaneous observation of PsAs by the Arase satellite and ground-based all-sky cameras. During the event, the occurrence of internal modulation increased temporally. The wave data from the satellite show that the repetitive frequency of chorus elements, which is considered as the source of the internal modulation, was $\sim$6 Hz when the internal modulation was indistinct, while the repetitive frequency was $\sim$3 Hz when the internal modulation was distinct. The in-situ particle measurements suggest that this difference was caused by changes in the density and the temperature anisotropy of the hot electron. The internal modulation was clearly observed when the density of hot electrons decreased, and the temperature anisotropy relaxed after the injection. Observations of internal modulations from the ground using optical instruments, including commercial digital cameras, might allow us to estimate the parameters such as the density and temperature anisotropy of energetic electrons in the magnetosphere.

Commercial digital cameras cost about 1/10th of the cost of professional cameras for scientific use. Not only that, they are lightweight and compact, allowing them to be installed in many observatories. Besides scientists, photographers and tourists also use commercial digital cameras. While optical observations by scientists can only be made at dedicated observatories with good infrastructure, photographers and tourists can obtain data at various locations. These locations may fill the gap in the observable areas currently covered by scientists. This study has revealed that commercial digital cameras can be used to quantitatively estimate the intensity of auroras at 427.8 nm and 557.7 nm and detect the sub-second modulation of auroras. Based on the evaluation of the performance of commercial digital cameras, the number of optical data that can be used for scientific studies of auroras will increase drastically, which will further lead to a denser measurement network and the discovery of new phenomena.

Acknowledgments/謝辞

I would like to express my heartfelt gratitude to Prof. Keisuke Hosokawa for his significant contributions to the completion of this dissertation. Despite his busy schedule, he provided me with meticulous guidance throughout my research, serving as a pillar of support in my Ph.D. course. I have learned from him not only practical aspects such as how to advance research, attract audiences with presentation skills, and build logical papers and proposals, but also imbibed values of approaching every task with passion and maintaining a strong work ethic regardless of temporal fluctuations in motivation. Additionally, this dissertation describes the observation of auroras at the Swedish Institute of Space Physics (IRF) in Kiruna, Sweden, and I was able to conduct the observation thanks to him, who negotiated with a host researcher on my behalf. I express my gratitude once again for his invaluable contributions.

I have received valuable advice on interpreting the data obtained from the Arase satellite from Prof. Yoshizumi Miyoshi and Dr. Satoko Nakamura at Nagoya University. Prof. Miyoshi graciously served as my host researcher when we conducted collaborative research at Nagoya University. He meticulously taught me how theoretical formulas regarding the behavior of waves and particles in the magnetosphere reflect with the observational data. Dr. Nakamura not only offered advice in studies but also provided support in personal aspects such as mental health issues. During my doctoral course, she was my greatest source of emotional support. I might not have been able to complete my doctoral studies without her support.

Regarding the observation conducted in Tromsø, Norway, I have received substantial support from Assoc. Prof. Satonori Nozawa and the technical staff, Mr. Tetsuya Kawabata, at Nagoya University. Thanks to their assistance, I installed a camera at the Ramfjordmoen field station and had a stable observation. I express my gratitude to them

for their contributions. At Nagoya University, not only the individuals above but also the graduate students warmly welcomed me. I enjoyed random conversations with them during breaks from work.

Mr. Tomonori Abe at the students' counseling office provided me with mental support. I had various mental problems during my doctoral course, but through dialogue with Mr. Abe, I was able to ease my mind on many occasions mentally. I would like to express my gratitude to Mr. Abe for his kindness and for listening to me.

To expand the coverage of Tromsø AI, I installed an all-sky digital camera in Skibotn, Norway. This was made possible through the generous support of Dr. Magnar G. Johnsen, the head of the Tromsø Geophysical Observatory. He not only provided a space for installing the camera and transportation to Skibotn but also extended various kindnesses, including promoting Tromsø AI, providing K-index data, and offering an opportunity to give a seminar at the University of Tromsø.

At IRF, I had the privilege of working as a guest researcher under the supervision of Dr. Urban Brändström. Despite not knowing each other before, I am deeply grateful for his warm welcome and support. On our way back from the Nordic Observatory Meeting, we had an opportunity to visit the ALIS_4D facility in Silkkimuotka, where I was greatly impressed by the large machines that allow flexible adjustment of the direction of the camera. This experience remains vivid in my memory. He also showed a strong interest in my observation and provided me with opportunities to engage in regular meetings with a research group in IRF Lund that is working on the automated classification of auroral images. I extend my gratitude once again for his support. Domo arrigato!

During my stay at IRF, I wrote several manuscripts prompted by Dr. Masatoshi Yamauchi. He gave me much advice on the content of my writing, and it was a stimulating experience. Thank you very much.

During my stay in Kiruna with insufficient English skills, thrice-weekly bird feeding with Dr. Peter Dalin provided me regular solace. He graciously welcomed my interest in bird feeding and taught me much about the local birds around IRF. Over the course of my seven-month stay in Kiruna, while regrettably not acquiring significant knowledge of Svenska, I did learn many bird names in Svenska like talgoxe, nötskrika, tallbit, etc. Besides bird feeding, he allowed me to join the installation of his ground-based airglow

camera and engaged in discussions with him on the auroras that contaminated his data.

As mentioned above, I was affiliated with several research institutes during my doctoral course. However, I believe the individuals with whom I shared the most time were the students in the Hosokawa Lab. They graciously accompanied me for weight training at the gym in UEC and engaged in random conversations, for which I am deeply grateful.

Finally, I would like to express my utmost gratitude to my family for their understanding and support in pursuing my doctoral studies far from home. Thank you so much.

本論文の作成にあたり、多大なご尽力を賜りました細川敬祐先生に心より感謝いたします。細川先生には、ご多忙の中でも常に丁寧なご指導をいただき、研究生活の大きな支えとなっていただきました。細川先生からは、研究の進め方、聴衆を惹きつけるプレゼンテーション技術、論文や申請書の論理的な書き方などの実践的なことだけでなく、何事にも熱意を持って取り組むという価値観や、その時々のモチベーションに左右されずに仕事をこなす姿勢を学びました。また、本論文にはスウェーデン・キルナの宇宙物理学研究所（IRF）で行ったオーロラの観測が含まれますが、IRF での観測が行えたのも、細川先生が交渉を行って下さったお陰です。重ねて感謝いたします。

あらせ衛星が観測したデータの解釈には、名古屋大学の三好由純先生や中村紗都子さんから多くのアドバイスをいただきました。三好先生には、私が名古屋大学で共同研究を行う際の受入教員となっていただき、磁気圏における波動・粒子の振る舞いに関する理論式が観測データにどう結びついているかを丁寧に教えていただきました。中村さんには、研究のことだけでなくプライベートでも数多くの相談に乗っていただき、博士課程の期間中、精神面で最も大きな支えとなっていただきました。中村さんがいなければ、私は博士課程を修了することができなかったかもしれません。深く感謝いたします。

ノルウェー・トロムソでの観測に際しては、名古屋大学の野澤悟徳先生、技術職員の川端哲也さんに多くのサポートをしていただきました。Ramfjordmoen 観測所内にカメラを設置し、安定した観測が行えたのは野澤先生や川端さんのお陰です。厚くお礼を申し上げます。名古屋大学では、上記の先生方だけでなく、修士課程の学生にも仲良くしていただきました。感謝しています。

学生何でも相談室の阿部朋典様には精神面でサポートをしていただきました。私は博士課程在籍中に様々な悩みを抱え、体調を崩すことがありましたが、阿部さんとの対話を通じて精神的に楽になることが何度もありました。困ったときに駆け込める場所を作っ

てくださった学生何でも相談室や、親身に話を聞いてくださった阿部さんに感謝いたします。

また、Tromsø AI の観測領域を増やすため、ノルウェー・シーボトンに全天デジタルカメラを設置させていただきましたが、これはトロムソ地磁気観測所の Magnar G. Johnsen 所長のご厚意によるものです。Magnar 先生には、カメラの設置場所の提供やシーボトンまでの運転だけでなく、Tromsø AI の宣伝や K 指数の提供、トロムソ大学でのセミナー発表を行う機会を与えていただくなど、多岐にわたって親切にしていただきました。

IRF での観測では、Urban Brändström 博士に受入研究員となっていただきました。Urban 先生とはそれまで面識がなかったにも関わらず、私を受け入れてくれたことに深く感謝いたします。Nordic Observatory Meeting の帰り道には、Silkkimuotka にある ALIS_4D のハットを見学させていただきました。大きな装置でカメラの向きを自在に変化させる仕組みを見せていただいた時の感動は、今も忘れることができません。私の観測にも強い興味を持っていただき、私の開発したオーロラ自動検出モデルによる結果を観測装置のトリガとして採用していただいたり、私と同じくオーロラの観測画像の自動分類を試みている Lund の研究グループとも定期的な議論をする機会を与えてくださいました。重ねて感謝いたします。

IRF での滞在中には、いくつかの原稿を執筆しましたが、それらは山内正敏博士が声をかけてくださったことがきっかけになったものでした。執筆内容についてのアドバイスも数多くいただき、刺激的な経験をすることができました。ありがとうございました。

英語が得意ではない私のキルナ滞在に、定期的な安らぎを与えてくれたのは Peter Dalin さんとの週 3 回の野鳥の餌付けでした。彼は、餌付けに興味を持った私を快く受け入れてくれ、餌付けをしながら IRF 近辺に生息する野鳥のことを多く教えてくれました。延べ 7ヶ月のキルナ生活で、残念ながらスウェーデン語の知識はほとんど得られませんでしたが、野鳥の名前はスウェーデン語でたくさん覚えることができました。Peter さんとは野鳥の餌付けだけではなく、大気光の地上観測の立ち上げを拝見させてもらったり、大気光の観測データにノイズとして映り込んだオーロラに関する議論を行うこともできました。

上述の通り、私は博士課程の期間中にいくつかの研究機関のお世話になりましたが、最も多くの時間を共有したのは細川研究室に所属する学生たちだと思います。彼らには電通大内のジムでのウエイトトレーニングや日常的な雑談に何度も付き合っていただき、深く感謝しています。

最後に、実家から遠く離れた地で博士課程に進学することに理解を示し、支援して下

さった家族に最大の感謝を表明します。ありがとうございました。

2024 年 1 月　東京都調布市にて
南條壮汰

Contents

Chapter 1

General Introduction

1.1 The Earth's magnetosphere

The Earth has its own magnetic field. The magnetosphere is the region where the magnetic field affects the surrounding plasma environment. A dipole field can approximate the Earth's magnetic field (Alken et al., 2021). However, since it is compressed by plasma streams from the Sun (solar wind), the magnetosphere has a complicated structure, as shown in Figure 1.1. The magnetic field is highly stretched towards the anti-sunward direction (right side). This region of the stretched magnetic field is called the magnetotail, and most of the magnetospheric plasma, which originates from the Sun, is trapped near the equatorial plane on the nightside (plasma sheet). The trapped charged particles bounce along the stretched magnetic field lines. Such bouncing particles in the plasma sheet are sometimes accelerated by several mechanisms and precipitate into the atmosphere of the Earth.

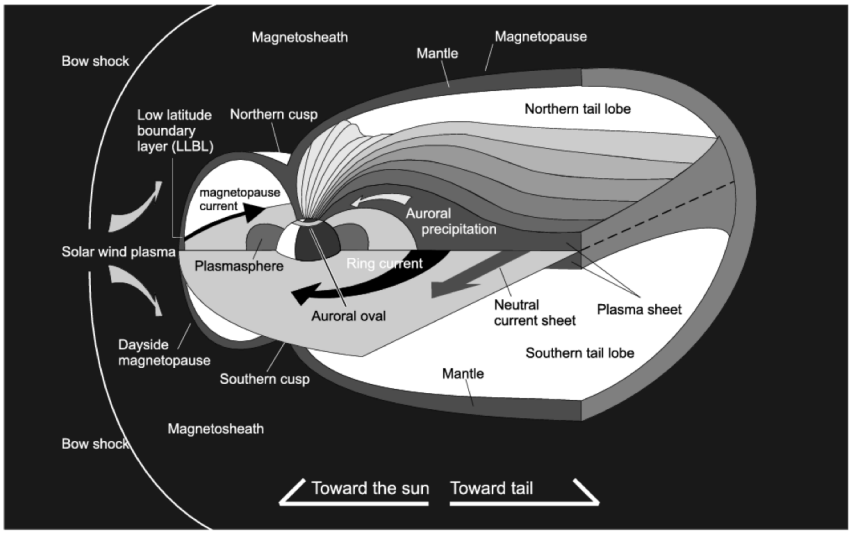

Figure 1.1: Schematic illustration of the Earth's magnetosphere (cited from Hosokawa (2002)). The Sun is to the left of the figure, and the solar wind blows from that side. The magnetic fields of the Earth are stretched toward the nightside on the right-hand side of the figure and forms the magnetotail.

The precipitation of trapped charged particles is particularly intense during high-speed solar wind, leading to disturbances known as magnetic storms. Magnetic storms are identified by a decrease in the Dst index (Sugiura, 1964) and the SYM-H index (Iyemori and Rao, 1996), both of which reflect variations in the westward current near the equatorial plane of the magnetosphere (ring current). These disturbances often continue for several days (Hutchinson et al., 2011). Charged particle precipitation is also intense during substorms, which occur on shorter timescales than magnetic storms (Meng and Liou, 2004). Substorms are initiated when the north–south (z-axis) component of the interplanetary magnetic field (IMF) turns southward (negative) through the inflow of energy from the solar wind to the magnetotail and its explosive release. Those are identified by the Auroral Electrojet (AE) index (Davis and Sugiura, 1966) and the SuperMAG AE index (Newell and Gjerloev, 2011), both of which are longitudinally averaged geomagnetic indices reflecting the planetary-scale status of substorms. The near-Earth side of the plasma sheet is called the radiation belt, where plasmas having even higher energy are distributed (Millan and Thorne, 2007). Since charged particles in the radiation belt can cause severe damage to satellites, they are sometimes called "killer electrons." The lower

cut-off altitude of particle precipitation (stopping height) depends on their energy, and higher energy particles precipitate down to lower altitudes. Killer electrons can precipitate to lower altitudes than typical particles in the plasma sheet, causing ozone depletion (Turunen et al., 2016). Given these considerations, it is important to investigate how electrons are energized, distributed, and precipitate into the ionosphere.

1.2 The atmosphere of the Earth

The precipitation of electrons along the magnetic field lines often reaches about 800 km or lower altitudes. This altitude region is called the ionosphere because a fraction of the atmospheric particles are ionized due to the extreme ultraviolet (EUV) emissions from the Sun. As a first approximation, the number density of ionized particles is determined primarily by the intensity of EUV emissions from the Sun and the density of Earth's atmosphere. This fact means that the variation of the ionosphere depends on various parameters such as solar activity, season, local time, and altitude (Brekke, 1997). In most cases, however, altitude is used as a primary parameter to describe the characteristics of the ionosphere. In descending order of altitude, the ionosphere is divided into three regions: the F region (above 150 km), the E region (90–150 km), and the D region (60–90 km). The dominant ion in the F region is O^+, while the E region is primarily composed of NO^+ and O_2^+. As mentioned above, the ionization is mainly caused by EUV emissions, resulting in higher ion and electron densities during the daytime and lower densities at night. However, when electrons precipitate into the ionosphere, an additional ionization is induced by the precipitation of electrons. In some cases, such electron density enhancement caused by the precipitating particles can be higher than in the daytime, even at nighttime.

The number density of the ionized particles is several orders of magnitude lower than that of the neutral particles in the ionosphere. Figure 1.2 displays the altitude profile of the number density of electrons and neutral particles during daytime and nighttime. The number density of the neutral atmosphere increases notably in the D and E regions. Figure 1.3 shows the number density of representative neutral atoms and molecules as a function of altitude. The left and right panels show the distributions in the densities

during low and high solar activity. Nitrogen molecules, oxygen molecules, and oxygen atoms dominate the D and E regions. Electrons precipitated from the magnetosphere often collide with these atmospheric particles in the D and E regions, leading to the atmospheric illumination known as aurora, which will be described in Section 1.3.

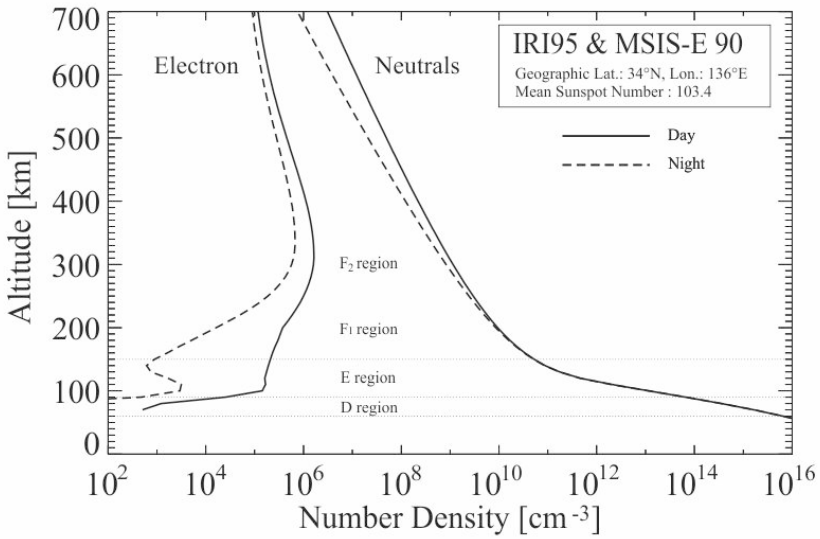

Figure 1.2: Typical ionospheric density profile of the electrons as a function of altitude deduced from International Reference Ionosphere (IRI) 95 model (Bilitza, 1997), together with the density profiles of the neutral particles is deduced from MSIS-E 90 model (Hedin, 1991). The solid and dashed lines show the daytime and nighttime profiles, respectively (cited from Hosokawa (2002)).

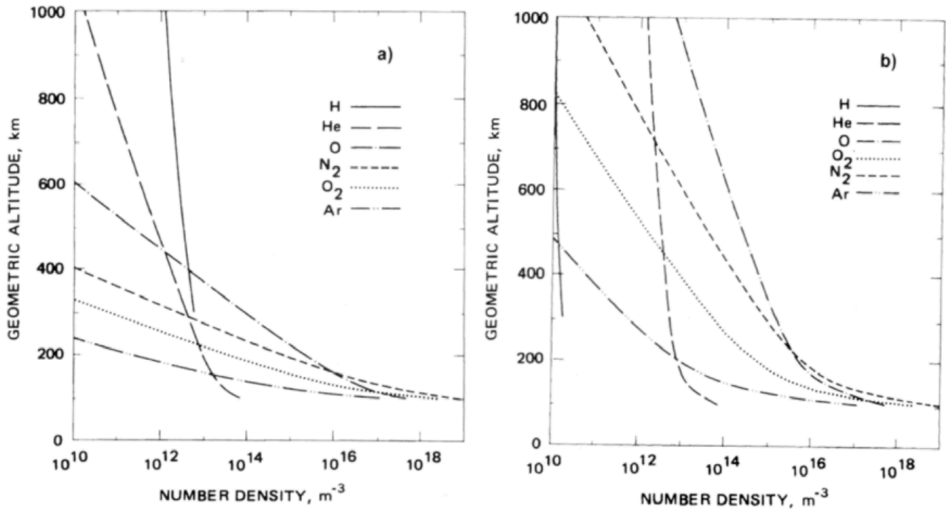

Figure 1.3: The altitude profiles of neutral densities during the period of the lower solar activity (left panel) and the period of the higher solar activity (right panel) (cited from Brekke (1997)).

1.3 Auroras

1.3.1 Auroral emissions

The electrons penetrated from the magnetosphere can collide with atmospheric particles in the lower part of the ionosphere, changing the status of the particles to an excited state. Such excited particles eventually return to their original state (or lower energy state) and emit the excess energy (excitation energy) as an optical emission. This emission is often visible from the ground and has been known as an aurora (e.g., Akasofu, 1965). Auroras are not always visible, even if a collision occurs between the charged and neutral particles. Whether a particle is excited or not depends on the energy of the precipitating particles, the composition/density of the atmospheric particle, and its state. In addition, excited particles can lose their excitation energy by colliding with surrounding neutrals before producing emissions, in which case auroral emission cannot be seen (atmospheric quenching). As mentioned in Sections 1.1 and 1.2, the composition of the atmospheric particles and the energy of the precipitating particles depend on altitude; thus, we should describe the process producing the auroral emission for different altitude regions. Since

the auroras investigated in this thesis are caused by precipitations of electrons, those created by protons (proton aurora) are not mentioned here.

In the region above ∼200 km altitude, the "red line" at 630.0 nm is the dominant auroral emission. This reddish emission is produced through the transition of oxygen atoms from excited state ^1D to the ground state ^3P, which is expressed as follows:

$$\mathrm{O}(^1D) \rightarrow \mathrm{O}(^3P) + h\nu \ (\lambda = 630.0 \text{ nm}). \tag{1.1}$$

Here, h is Planck's constant, and $h\nu$ is the excitation energy, i.e., the difference in energy between the ^1D and ^3P levels. Since $\mathrm{O}(^1D)$ has a long lifetime of about 110 seconds (Jones, 1971, 1974), this emission is categorized as the forbidden lines, and it cannot produce visible emission at lower altitudes because of the quenching due to high atmospheric density. At altitudes from 100 to 200 km, there are sufficient oxygen atoms and nitrogen molecules. At these altitudes, the "green line" at 557.7 nm is dominant, which is also produced by excited oxygen atoms, which is described as follows:

$$\mathrm{O}(^1S) \rightarrow \mathrm{O}(^1D) + h\nu \ (\lambda = 557.7 \text{ nm}). \tag{1.2}$$

This line has a lifetime of about 0.7 seconds (Jones, 1971, 1974), and the green line is also a forbidden line, but the atmospheric density is sufficiently low to cause this emission in these altitudes. The green line is the most intense auroral emission, and the greenish color seen in auroral photographs is due to this line. At altitudes of 80–100 km, the forbidden lines do not occur due to the increased atmospheric density, and only the permitted lines with lifetimes close to zero can be emitted. In this altitude region, the emissions of nitrogen molecules and nitrogen molecular ions are likely to occur. Unlike oxygen atoms, the structures of these molecules are complex. Hence, they do not emit a monochromatic single peak emission like the green and red lines but produce multiple band-like emissions. The band emission of nitrogen molecular ions is called the first negative (N_2^+ 1NG) distributing in 390–470 nm, while that of nitrogen molecules is called the first positive (N_2 1PG) above 650 nm. As a result of the combination of two band emissions, the aurora at this altitude range (i.e., below 100 km) shows a white or pink color.

In addition to the color, aurora can be classified by the spatial and temporal variations in their shape. The most famous classification is the two-class classification: discrete and

diffuse auroras. These two classes are considered to be representatives of the two major processes causing electron precipitation (magnetically field-aligned acceleration/wave-particle interaction). The following sections describe those two broad categories of auroras in detail.

1.3.2 Discrete auroras

Discrete auroras have solid spatial structures described by arcs, curtains, or curls (Tsurutani et al., 2023). Compared to diffuse auroras (see Section 1.3.3), they can be seen over a wider altitude range from 80 to 300 km (Jones, 1971), often emitting both the green and red lines (Semeter et al., 2001). The band emissions of nitrogens are also observed at their lower altitude limit if the energy of the precipitating electrons is sufficiently high.

Figure 1.4 shows the global distribution of auroras (Akasofu, 1976). The figure is in the polar coordinate system with the magnetic latitude (MLAT) in the r direction and the magnetic local time (MLT) in the ϕ direction. The upper side is the direction of the Sun. The solid lines indicate discrete auroras and are generally distributed at higher latitudes than diffuse auroras.

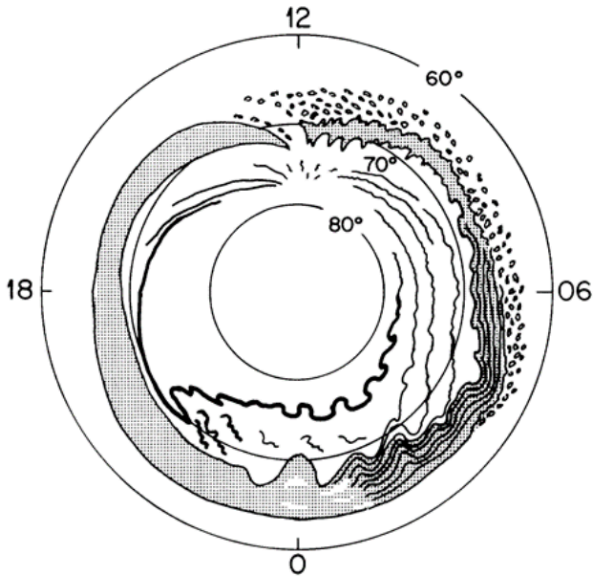

Figure 1.4: Schematic illustration showing the spatial distribution of the discrete, diffuse and omega band aurora (cited from Akasofu (1976)).

With the development of low-Earth orbiting satellites, the acceleration mechanism of electrons that produce discrete auroras has been investigated. The particle observation by the Injun-5 satellite has revealed a so-called inverted-V structure in the electron energy-time spectrogram in which a "monoenergetic" peak increases in time and reaches the peak and then decreases (Frank and Ackerson, 1971; Gurnett and Frank, 1973). Gurnett (1972) has proposed a U-shaped equipotential structure, which accelerates electrons by the field-aligned electric field, to explain the inverted-V structure. The conceptual diagram is shown in Figure 1.5. The existence of this structure has been confirmed by in-situ measurements using the S3-3 satellite, which has an apogee of 8000 km (Mozer et al., 1977, 1980). Simultaneous observations of the particle measurements by the FAST satellite and optical observations by the all-sky camera and an aircraft equipped with a TV camera showed that there is a correspondence between the inverted-V structure and the discrete auroral structure (Stenbaek-Nielsen et al., 1998). These results suggest that the discrete aurora is produced by electrons accelerated by the U-shaped equipotential structure between the ionosphere and magnetosphere.

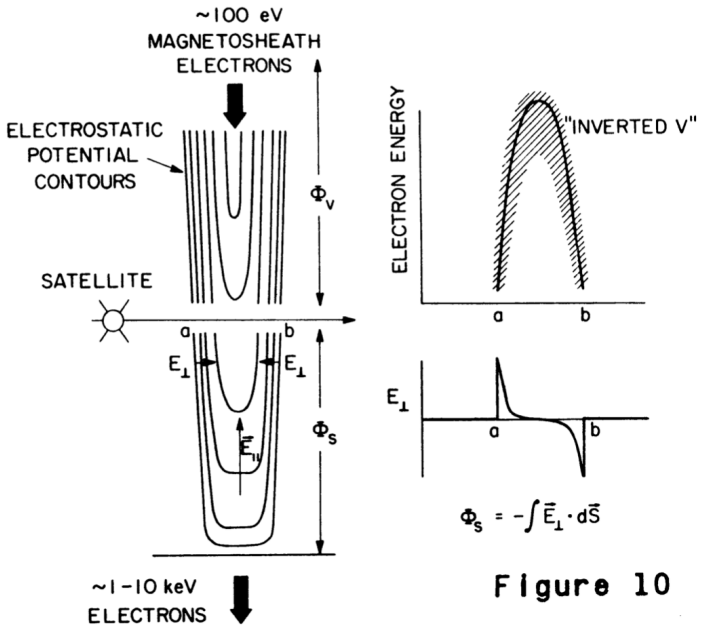

Figure 1.5: Schematic illustration showing the qualitative forms of the U-shaped equipotential structure and the inverted-V (cited from Gurnett (1972)).

1.3.3 Diffuse auroras

Unlike discrete auroras, diffuse auroras have a narrow altitude range of 80–110 km (Brown et al., 1976; Kataoka et al., 2013). Some of them change their brightness quasi-periodically, known as pulsating auroras (PsAs). In Figure 1.4, patchy PsAs are shown in the lower latitude part in the morning sector. They have a broad local time distribution but are known to occur more frequently in the morning sector. PsA is also known to be more frequently observed during the recovery phase of the substorm (Partamies et al., 2017).

In addition to the occurrence distribution, PsA is characterized by their periodicity. Two widely known pulsating periods exist: the main pulsation and the internal modulation. The periodicity of the main pulsation ranges from a few to a few tens of seconds (Lessard, 2012; Yamamoto, 1988), while the internal modulation has a few hertz periodicities (Royrvik and Davis, 1977). The main pulsation is sometimes called ON-OFF switching because the brightness changes like a switch on and off of light. The internal modulation is embedded within the bright time (ON phase) of the main pulsation. The average energy of precipitating electrons responsible for PsA (PsA electrons) tends to be higher than that of discrete auroras, ranging from a few to several tens of keV (Sandahl et al., 1980; Nishiyama et al., 2011), as inferred from its lower emission altitude. In addition to the green-line emission, the band emissions of nitrogen molecules are often observed. Especially in the morning sector, high-energy (> 1 MeV) electrons called killer electrons from radiation belts have been observed within a region of PsA (Miyoshi et al., 2020), which may cause ozone depletion (Turunen et al., 2016).

The precipitation mechanism of the PsA electrons has been discussed in close association with the natural electromagnetic waves at the Very Low Frequency (VLF) range occurring near the equatorial plane of the magnetosphere (Tsuruda et al., 1981). Later, it has been suggested that the main modulation of PsA is related to the burst-like periodic generation of the whistler-mode chorus waves in the magnetosphere (Thorne et al., 2010). Their correspondence was confirmed by the conjugate observation with the Time History of Events and Macroscale Interactions during Substorms (THEMIS) satellite and ground-based all-sky camera (Nishimura et al., 2010). Figure 1.6 shows a schematic diagram showing this conjugate observation. The result showed the one-to-one correspondence between the temporal variations of PsA and the chorus wave. Later, Kasahara et al.

(2018a) has demonstrated that the chorus waves indeed change the pitch angle of electrons in the magnetosphere, and the resultant precipitations of electrons contribute to the optical emission of PsA by investigating the in-situ observation of the Arase satellite and optical observation with a ground-based camera. The high-speed measurements of the Arase satellite also enabled us to see the correspondence between tiny chorus elements and the internal modulation of PsA. Hosokawa et al. (2020) suggested that the existence of the internal modulation of PsA depends on the discreteness of the internal structure, also known as the element structure, of the chorus wave. Figure 1.7 shows the time series of the optical pulsations of PsA from the electron multiplying CCD (EMCCD) camera and the intensity of chorus waves observed by the Arase satellite at the magnetic conjugate point of PsA. The left panel shows the main pulsation without internal modulation, and the right panel shows that with internal modulation. In both panels, there is a correspondence between the sub-second variations of PsA and the intensity of the chorus waves. That is, the existence/absence of the internal modulation is controlled by that of the element structure in the chorus waves.

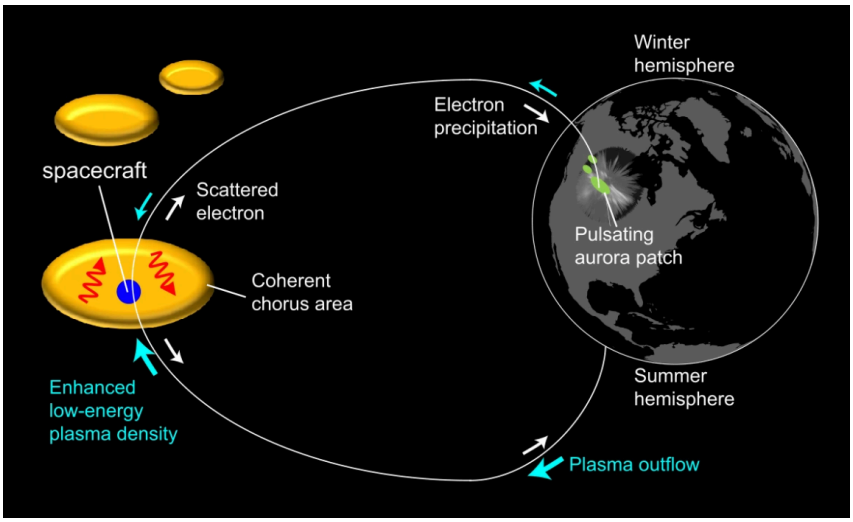

Figure 1.6: Schematic illustration showing the conjugate observation of PsA from the ground and in the magnetosphere (cited from Nishimura et al. (2015)).

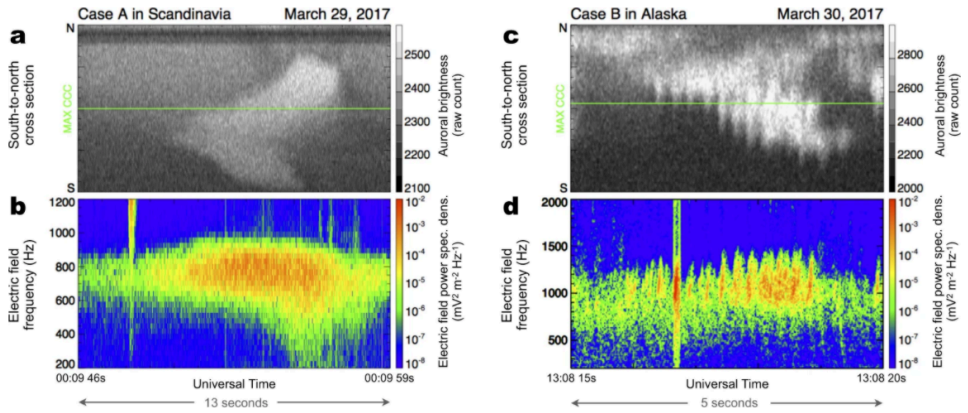

Figure 1.7: A comparison between the PsA modulations (upper) and chorus waves (lower) (cited from Hosokawa et al. (2020)). The presence/absence of internal modulation is consistent with the discreteness of chorus waves.

1.4 Observations of auroral phenomena

1.4.1 Measurements of the auroral ionosphere

As mentioned above, auroras are visualized when the magnetospheric plasma (mostly electrons) is accelerated/scattered by some process and precipitated into the ionosphere along the magnetic field line. In this sense, two-dimensional imaging of auroral phenomena with a camera implies two-dimensional visualization of the dynamics of the magnetospheric plasma. Other than cameras, many other instruments are used to observe aurora-related phenomena and corresponding variations of physical quantities. Optical instruments such as photometers and spectrometers are used for precise measurements of auroras, but they generally do not provide spatial characteristics of auroras as two-dimensional images. Active radio instruments such as incoherent scatter radars and ionosondes are used to measure the electron density in the altitudes of auroras. Passive radio instruments such as riometers, which measure cosmic noise absorption, are also frequently used to detect electron density enhancement in the low-altitude part of the ionosphere. However, these radio observations cannot track the fast (sub-second) variations of aurora due to the infinite time constant of recombination (Hosokawa et al., 2010). Fluxgate and proton magnetometers measure the geomagnetic field variations caused by the enhancement

of ionospheric currents during auroral phenomena, but it is rather difficult to infer the small-scale spatial structure only from data from magnetometers. Sounding rockets and low-Earth orbiting (LEO) satellites sometimes carry out in-situ measurements of precipitating electrons at altitudes of around a few hundred kilometers, but their observations are one-dimensional along their orbit.

The only way to measure magnetospheric plasma directly is in-situ observation by satellites in the magnetosphere. However, since the satellite can only measure the particle and field at a single point, it is impossible to visualize how the spatial structure of the plasma environment changes over time. Furthermore, it is difficult to distinguish the temporal variation and spatial distribution only from the single point observations by moving satellites. Considering the factors mentioned above, auroral imaging is the only way to capture both the spatial and temporal variations of the magnetospheric plasma environment in a two-dimensional fashion. Namely, the camera is an instrument not only for measuring auroras but also for allowing us to visualize the dynamics of magnetospheric plasma, which is closely connected to the behavior of aurora via magnetic field lines. In the following, a brief introduction to the optical observations of aurora will be described. In particular, the recent progress in citizen science using commercial digital cameras will be summarized, which is closely related to the primary motivation of this thesis.

1.4.2 Optical observations using cameras

The first auroral imaging was made by Brendel in 1892 (Baschin, 1900; Schröder, 1997). Birkeland (1913) is one of the first persons who revealed the macroscopic dynamics of the aurora at multiple locations. Subsequently, auroral imaging has been generally performed by capturing the entire sky to obtain a wider field of view (FoV), which is still the case today. Nowadays, scientists use a fisheye lens for auroral imaging in most cases, but in the 1940s, a bowl-shaped mirror was used to observe the reflection of the aurora on the mirror (e.g., Stoffregen, 1956).

Many all-sky cameras are in operation in the Nordic countries, Canada, Alaska, and Antarctica these days. The Magnetometers – Ionospheric Radars – All-sky Cameras Large Experiment (MIRACLE) network by the Finnish Meteorological Institute (FMI), the Sodankylä Geophysical Observatory (SGO) of the University of Oulu covers the entire

sky over Finland (Syrjäsuo et al., 1998) by multiple all-sky cameras. Auroral Large Imaging System 4D (ALIS_4D) by the Swedish Institute of Space Physics covers most of the sky over northern Sweden (Brändström, 2003). The EMCCD camera network by the Japanese Pulsating Aurora Project covers most of the skies over the northern Nordic countries (Hosokawa et al., 2023). The THEMIS all-sky imagers cover a longitudinally extended large area across Alaska and Canada (Mende et al., 2008). The data from these observations are widely used for recent auroral research and can be considered the flagship optical observations. Some CCD sensors used for the optical observations listed above can perform high-speed imaging with a temporal resolution of 0.01 seconds thanks to their high sensitivity (quantum efficiency). However, such high-speed imaging systems tend to be large and heavy because of a large heat sink and fan to cool the sensor.

Small and low-cost cameras have also often been used for observations of auroras. Ogawa et al. (2020b) have installed several small CCD cameras from Watec Co., Ltd. at the same observatory to simultaneously observe an aurora at various angles of view and wavelengths. In addition to the Watec camera, the CMOS cameras from ZWO Co., Ltd. are also used in the Nordic countries, for example, for the Boreal Aurora Camera Constellation (BACC) project. Although the temporal resolution of these cameras is lower than that of the flagship cameras, they are inexpensive and small in size, allowing multiple cameras to be installed easily.

Interference filters are often used in optical observations with cameras and photometers. As mentioned in Section 1.3.1, the spectrum of auroral emissions is discrete. Some are prompt emissions, such as the band emission of nitrogen molecules, but there are also forbidden lines, such as 557.7 nm and 630.0 nm. If all of these emissions are received in a single channel, it is difficult to estimate the timing of the precipitation of electrons causing the emission, which is fairly important for comparing the optical data from the ground with those from magnetospheric satellites. To solve this problem, interference or notch filters are used to transmit only specific wavelengths or bands. For example, the EMCCD cameras in the Pulsating Aurora Project remove green and red lines and capture only prompt emissions with BG3/RG665 glass filters (Samara et al., 2012). ALIS_4D and Optical Mesosphere Thermosphere Imagers (Shiokawa et al., 1999) are equipped with a filter wheel that has several filters so that the multiple emission lines (or bands) can

be observed sequentially through rotation of the filters. However, these cameras observe only one wavelength or band at a moment, and multiple wavelengths or bands cannot be observed simultaneously. This is because the CCD sensors in these cameras have only a single channel.

1.4.3 Commercial digital cameras as optical instruments

Watec and ZWO provide color cameras with multi-channel sensors that can capture multiple wavelength bands simultaneously, but one problem common to all of the above cameras is that they require an observatory with good infrastructure, such as a stable power supply. The sky must be clear to observe the aurora on the ground since auroras are higher than clouds. No matter how sophisticated the cameras are, it is impossible to observe auroras if the sky is cloudy. In this sense, observing auroras only at specific observatories would be a severe disadvantage; in simpler terms, researchers cannot change observation points as they seek clear skies. Commercial digital cameras can solve this problem. Since commercial digital cameras are battery-powered, they can capture the aurora without stable infrastructure. Such mobility would enhance the possibility of observing auroras that conventional optical observation networks cannot cover. Therefore, the commercial digital camera would be an essential instrument for increasing the number of datasets used in the analytical study of auroras.

The number of scientific studies using photographs captured with commercial digital cameras by citizen scientists, such as photographers and auroral guides, has been increasing in the recent decade (e.g., Palmroth et al., 2020; Semeter et al., 2020; Chu et al., 2020; Martinis et al., 2022). In particular, the discovery of Strong thermal emission velocity enhancement (STEVE), a new phenomenon that looks like an aurora but has a continuous spectrum, i.e., different phenomena from the aurora, from photographs observed by citizen scientists, has significantly impacted the aeronomy research community (MacDonald et al., 2018). However, these studies have used limited information: a vague quantity of "color" and the location and time of appearances. Since CMOS sensors in commercial digital cameras have three RGB channels and can observe three different bands simultaneously, the data in each color channel might have contained mixed contributions of the forbidden lines and prompt emissions. Besides, if the brightness of an aurora can be mea-

sured in multiple channels, it may also be possible to estimate the average energy of the auroral electrons because the response of each emission line would be different depending on the energy of incoming electrons. If this could be done, the data obtained by citizen scientists (which are posted like flooding on social media) could be used even for more precise scientific research. Currently, however, almost all commercial digital cameras used for citizen science have not been calibrated quantitatively; thus, they are still not recognized as proper scientific instruments. In order to broaden the use of commercial digital cameras in scientific research, scientists must evaluate the quality of the data from various digital cameras. In particular, the advantages/disadvantages and limitations of auroral observations with commercial digital cameras should be diagnosed using well-calibrated cameras to observe various types of auroral phenomena.

1.5 Motivations and Purposes

To address the issues described in Section 1.4, the main purposes of this study are 1) to verify how reliable auroral photographs and movies taken by commercial digital cameras as a data set for quantitative research of aurora, 2) to know what kind of physical parameter can be estimated from the multi-channel color observations of commercial digital camera, 3) to understand what characteristics of aurora can be captured by commercial digital cameras and how such observations can be used for studying magnetospheric dynamics. In response to these goals, Chapter 2 analyzes images of PsAs taken from the International Space Station (ISS) using the Nikon D5. We have found that the color of PsAs tends to be more whitish in the morning side, where the average energy of the electrons responsible for PsAs is higher, i.e., the count value in the B channel increases. Since this tendency has theoretical support, that is, the higher energy electrons contributed to the prompt emission of nitrogen, mentioned in Section 1.3.1, we came up with the idea that the average energy of auroral electrons may be estimated from the count ratio in RGB channels (in particular, the B/G ratio).

In Chapter 3, to investigate the correspondence between the B/G ratio and the average energy of the auroral electrons, we installed a Nikon D5 in Tromsø, Norway, and attempted simultaneous observations with the European Incoherent SCATter (EISCAT)

radar (Rishbeth and Williams, 1985), which can estimate the average energy of auroral electrons. This subject corresponds to the first and second purposes mentioned above. To implement an automated digital camera observation in Tromsø, a system for the classification of the aurora was developed based on deep learning. The developed system showed a good performance with the F1 score of 93%, which is sufficient for being applied to the automated observations of auroras. As a by-product, the solar cycle and seasonal dependence of aurora appearance were derived by processing the digital camera images with the classification system, which is fairly consistent with the results of a previous limited number of statistical studies. Although a direct comparison between the Nikon D5 and the EISCAT radar has not been made yet, a comparison with the photometer shows that the B/G ratio positively correlates with the ratio of the brightness at 427.8 nm to the brightness at 557.7 nm, proving the validity of using the B/G ratio as an index of the average energy.

In Chapter 4, we operated the Sony α7SIII in Kiruna, Sweden, to capture videos of auroras rather than still images. The reason for conducting video recording is to investigate the potential utility of video data of auroras flooding on social media. For this video recording measurement, a system for pointing the camera in the direction of the aurora was implemented by combining the above-mentioned aurora detection system with a gimbal. The data from such an auroral measurement show that the video taken with a commercial digital camera allows visualization of the development of so-called shock aurora toward the nightside and the fast ($\sim$3 Hz) internal modulation of PsAs. This subject also corresponds to the first and second purposes.

In Chapter 5, we analyzed an event in which simultaneous observations of PsAs were made using high-speed cameras and the Arase satellite to discuss the scientific value of capturing the fast modulation of PsAs. This subject also corresponds to the third purpose. The results show that when fast modulation is observed in the PsA, the element structure of the whistler-mode chorus wave must appear at about 3 Hz, and this is evident when the density of high-energy electrons begins to decrease after the particle injection from the plasma sheet. This suggests the possibility of inferring the state of the magnetospheric plasma by observing the fast modulation of PsAs, which can also be observed with a commercial digital camera. In Chapter 6, the overall evaluation of commercial dig-

ital cameras for the research of auroras is summarized, and future direction is discussed following the results of this thesis.

Chapter 2

Colors and Periodicities of PsAs Observed Onboard ISS

2.1 Introduction

As already introduced in Section 1.3, auroras have been classified into two broad categories: discrete and diffuse auroras. Discrete auroras are generally bright with distinct shapes like arcs, curtains, and curls. They sometimes appear in a wide altitude range, e.g., from 90 to 300 km (Jones, 1971), which implies that electrons causing discrete auroras have a broad-band energy distribution. By contrast, diffuse-type auroras often show emissions only in a narrow range of altitudes, e.g., from 80 to 110 km (Kataoka et al., 2013; Brown et al., 1976). Thus, the energies of electrons causing diffuse auroras tend to be higher than those producing discrete auroras. Such differences in the energies of electrons responsible for discrete/diffuse auroras are often manifested in the colors of the auroras.

Discrete/diffuse electron auroras almost always show a greenish color at 557.7 nm, an emission of excited atomic oxygens. This most prominent oxygen emission is caused by typical auroral electrons with characteristic energies of a few keV and seen at $\sim$110 km altitude. At higher altitudes above 200 km, the red-line emission of oxygen atoms at 630.0 nm is produced by the softer component of electron precipitation. Different emissions can be observed below the layer of the green-line emission, i.e., near the bottom of auroral emission. Examples of these emissions include the first positive (1PG) band emission (650–700 nm: dark red) of nitrogen molecules N_2 and the first negative (1NG)

band emission (390–470 nm: bluish) of nitrogen molecule ions N_2^+ (Jones, 1971, 1974). These emissions, often seen as white/pink auroras below the greenish emission, are known as indicators of more energetic electron precipitation, with energies that are sometimes higher than 10 keV. Thus, the altitude distribution of the colors of an aurora is known to represent the energy distribution of precipitating electrons in, at least, a qualitative manner.

Diffuse auroras often show quasi-periodic variations called ON–OFF switching, commonly known as pulsating auroras (PsAs). PsAs are typically observed in the local time sector from the midnight to morning sector during the recovery phase of auroral substorms (Nishimura et al., 2020, and references therein). They are likely to occur under moderately disturbed conditions with a solar wind speed of ∼500 km/s, an IMF intensity of ∼8 nT, and an AE index of ∼400 nT (Partamies et al., 2017). Early ground-based observations of PsAs and VLF waves suggested that PsAs are caused by pitch angle scattering of energetic electrons by whistler-mode chorus waves (e.g., Tsuruda et al., 1981; Ozaki et al., 2012). After that, in a recent decade, several conjugate observations of PsAs with ground-based optical instruments and in-situ magnetospheric satellites revealed that the origin of a PsA is the interaction of energetic electrons with whistler-mode chorus waves in the magnetosphere (Nishimura et al., 2010; Jaynes et al., 2013; Kasahara et al., 2018a; Ozaki et al., 2019; Hosokawa et al., 2020). The period of ON–OFF switching is known to be in the range from 2 to 40 s (e.g., Lessard, 2012; Yamamoto, 1988; Nishimura et al., 2020). Although the source of its periodicity is the quasi-periodic nature of VLF chorus waves (Tsurutani and Smith, 1974; Sazhin and Hayakawa, 1992), the mechanism to control the periodicity has not been identified yet. It may depend on some macroscopic parameters such as the lengths of local magnetic field lines, which are determined by the magnetic latitude (MLAT) and/or the magnetic local time (MLT), as suggested by Thomas and Rothwell (1979). To evaluate such dependence on MLAT and MLT, it is essential to observe PsAs in wide MLAT and MLT regions simultaneously.

In the ON phase of PsAs, because the higher-energy electrons are likely to precipitate (McEwen et al., 1981b; Miyoshi et al., 2010), the emissions of 1PG and 1NG become intense. Ono (1993) measured PsAs using a multi-wavelength photometer with a high temporal resolution (10 Hz) at the Syowa Station in Antarctica. He theoretically esti-

mated the characteristic energies of PsA electrons from the emission-intensity ratios of 844.6 nm (O) and 427.8 nm (1NG) to 670.5 nm (1PG). However, because of the narrow FoV of the photometer, it was difficult to estimate the spatial distribution of the characteristic energy of PsA electrons. To investigate the characteristics of the energies of PsA electrons in detail, it is necessary to develop an easier way to perform such multi-spectral optical observations with sufficient spatial and temporal resolutions over a wide area.

Recently, digital single-lens reflex (DSLR) cameras have been used for auroral observations, especially in the framework of citizen science (e.g., MacDonald et al., 2018; Palmroth et al., 2020). Sigernes et al. (2008) suggested that the R, G, and B channels correspond to 630.0 nm and the 1PG band, 557.7 nm, and the 1NG band, respectively, by analyzing the relationship between the well-known emission lines of auroras and the transmission characteristics of the color filter of several DSLR cameras. Although the accuracy may be lower than those from the optimized multi-wavelength observations, these transmission characteristics could allow us to estimate the characteristic energies of auroral electrons. If the color images are obtained with wide FoVs covering a variety of MLAT/MLT ranges, we can discuss the spatial characteristics of auroral electrons in a wide region.

Nanjo et al. (2020) have developed a method for projecting images captured using DSLR cameras onboard the International Space Station (ISS) onto the geographic coordinate system using the calibration method developed by Hozumi et al. (2016) for estimating the several imaging parameters. They have also confirmed that the ON–OFF switching of PsAs can be captured using projected images from these DSLR cameras due to the high temporal resolutions less than one second. The camera onboard the ISS sweeps a wide area ($\sim$5 h in the MLT direction) in a short time interval ($\sim$10 min) because the orbital period of the ISS is short ($\sim$90 min). The images can then be used to investigate the spatial characteristics of 1) the periodicities of PsAs and 2) the energy of PsA electrons. In this Chapter, using DSLR camera observations from the ISS, the spatial distribution of the periodicity is derived over a wide area, and factors influencing it are discussed in close connection with the generation mechanism of PsA. We also evaluated whether the characteristics of the energy of PsA electrons can be estimated from ratios of the RGB channels based on the wide-FoV observations from the ISS.

2.2 Observations

2.2.1 The events

We analyzed two PsA events (hereafter Events 1 and 2) captured by a DSLR camera onboard the ISS during its excursion to high-latitude regions. Event 1 was observed for ∼9 min, from 07:44 to 07:53 UT, on 12 November 2018, in which the ISS was on a pass from southern Alberta to southern Quebec, Canada, in the Northern Hemisphere. On the other hand, Event 2 was observed for ∼8 min, from 18:07 to 18:15 UT, on 18 August 2018, when the ISS was above the Indian Ocean in the Southern Hemisphere. Figure 2.1 summarizes the background conditions of the geospace environment during Events 1 (left) and 2 (right). The top panels show the H component of the SYM index (Iyemori and Rao, 1996) in November 2018 and August 2018, respectively. These one-month plots of SYM-H indicate that both events did not occur during magnetic storms with clear initial, main, and recovery phases. At the same time, however, these were not always completely quiet intervals, as indicated by the slight decreases in the SYM-H index during the events. In particular, Event 1 had a minimum SYM-H index of −30 nT, corresponding to a weak magnetic storm, according to the definition by Loewe and Prölss (1997).

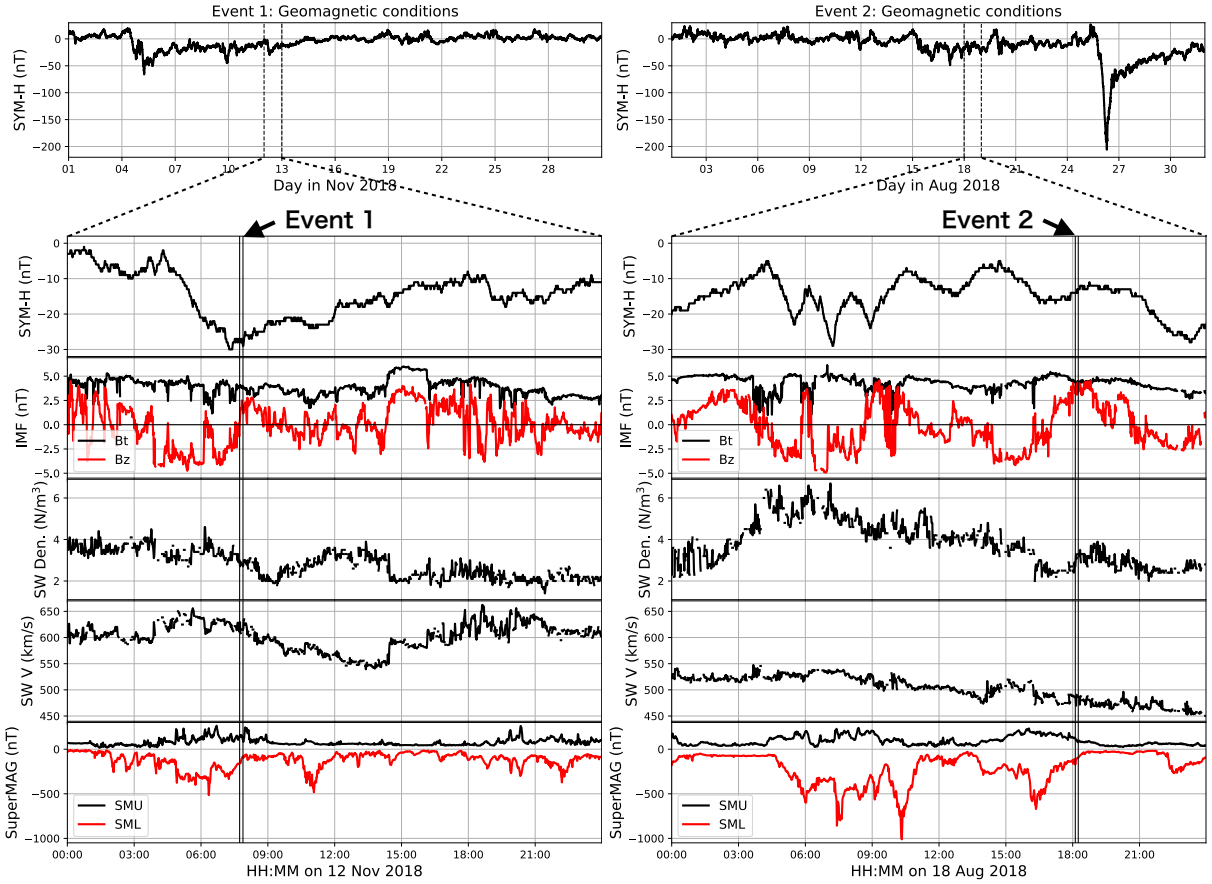

Figure 2.1: Background geomagnetic conditions for Events 1 (left) and 2 (right). Top panels show SYM-H indices for one month. Vertical dashed black lines mark days of Events 1 and 2. Second panels show SYM-H indices for one day. Third panels show interplanetary magnetic field in GSM coordinates. Black curves represent absolute values of the B, and red curves represent B_z component. Fourth panels show solar wind plasma densities. Fifth panels show solar wind speeds. Bottom panels show SuperMAG AE indices. Black curves represent SMU indices, and red curves represent SML indices. Pairs of vertical solid black lines mark the start and end, respectively, of Events 1 and 2.

The second to bottom panels of Figure 2.1 show one-day plots of various background parameters, such as SYM-H, interplanetary magnetic field (IMF) in the GSM coordinate system, solar wind density, solar wind speed, and SuperMAG auroral electrojet indices (Newell and Gjerloev, 2011). The pairs of vertical black lines mark the starts and ends of the events. Although no strong magnetic storms occurred in both Events 1 and 2,

the SYM-H index fell to nearly a few tens of nT below zero. The IMF B_z values were negative for several hours before the start of both events. The solar wind speed was high during Event 1, exceeding 600 km/s, whereas that during Event 2 was moderate, at ∼500 km/s. The SuperMAG upper/lower (SMU/SML) indices indicate that small substorms occurred immediately before Events 1 and 2 and that the observations were made during the late recovery phases of those substorms. No clear differences in the background conditions were observed between the two events, except that the solar wind speed was higher during Event 1. However, based on the SYM-H index, Event 1 occurred during a very small storm, as already mentioned, implying that the background condition was relatively more disturbed during Event 1 than Event 2.

We used DSLR camera images obtained during both events, which are publicly available online with Photo IDs from `https://eol.jsc.nasa.gov/`. The Photo IDs of the images from Event 1 range from ISS057-E-87611 to 88270, whereas those from Event 2 range from ISS056-E-146410 to 147974 and 149138 to 149543. Although the Photo IDs for Event 2 have a gap, the images were obtained continuously without any data loss. During both events, Nikon D5, with AF-S NIKKOR 24mm f/1.4G ED lens for Event 1 and AF-S NIKKOR 28mm f/1.4E ED lens for Event 2, was used for the imaging. The settings of the imaging were as follows: the exposure duration was 0.20 s for Event 1 and 0.25 s for Event 2, the ISO speed rate was 12800 for Event 1 and 10000 for Event 2, and the imaging interval was 0.67 s for Event 1 and 0.75 s for Event 2. Because the temporal variation of the ON–OFF switching of the main pulsation was a few to a few tens of seconds, these exposure durations and imaging intervals were sufficient for the periodicity analysis of the main pulsations of PsAs. To analyze the DSLR camera images as scientific datasets, we employed the mapping technique described by Nanjo et al. (2020). The auroral emission altitude was assumed to be 100 km in the mapping process.

We also used data from the RGB channels to estimate the energies of precipitating electrons. The sensitivity characteristics of each RGB channel of Nikon D5 were provided by de Miguel et al. (2019). According to their results, RGB sensitivity peaks at approximately 460, 540, and 610 nm, respectively, and the FWHM is ∼100 nm. Their Figure 1 showed that the greenish emission at 557.7 nm corresponds to the G channel. Their data also implied that the band emissions of N_2 and N_2^+ (1NG and 1PG bands

responsible for more energetic electrons) correspond to R and B channels, respectively. However, because the R channel is sensitive at 630.0 nm, it is safer to use the B channel as a proxy for more energetic electron precipitation. Thus, we employ the B/G ratio as an index for the ratio of harder/typical electron precipitation, which is expected to represent the energies of PsA electrons qualitatively. The relevant datasets on NASA's website are available in two types: 8-bit JPEG images and 12-bit raw images (.NEF format). Since raw processing simply replaces the raw array with an RGB array using a Bayer filter pattern (Bryce, 1976), no adjustments of the black level or white balance were performed. After raw processing, a median filter was applied because there were many hot pixels in the raw images. We used JPEG images to show the spatial structures of the auroras in 2D and employed raw images for more quantitative analysis of the time series and B/G ratios.

2.2.2 The time-series analysis

In this study, we intended to extract the periods of ON–OFF switching from successive DSLR camera images from the ISS through a time-series analysis. Because the FoV of the camera changed rapidly, we created a grid map with a resolution of 0.3°/1.2 min in the MLAT/MLT coordinate system covering the observed region and used the points, which continued to be within the FoV for at least 40 s, for the time-series analysis. The upper panel in Figure 2.2 shows an example of the time-series data from the camera in the region of the PsA. Characteristic temporal variations of the PsA, i.e., successive ON–OFF switchings, are present in all RGB channels. Here, however, only the G channel data were used to extract the periods because the signal-to-noise ratio of the G channel is better than that of the other two channels. The color channels of Nikon D5 have wide band transmission characteristics (FWHM: ∼100 nm); thus, the original time-series data contained large numbers of unwanted signals as compared to those in typical monochromatic observations using narrow band-pass filters (Grandin et al., 2017; Samara et al., 2012). To reduce contamination due to this effect, we used spline interpolation to smoothen the original signal and applied a low-pass filter to remove temporal variations with periods less than 2 s. In addition, because DSLR camera images from the ISS are captured in the direction of the rim of the Earth, the length of the optical depth changes depending

on the looking direction. Because of this effect, the time-series data shown in Figure 2.2 include a decreasing trend. To remove this trend, we also applied a high-pass filter and subtracted the trend, which had a temporal variation longer than 20 s. This effect is discussed in detail in Section 2.4.2. The G channel curve after the aforementioned signal processing is shown in the figure as a lime-green curve (labeled "processed G"). The ON–OFF switching of the PsA remains in the processed G curve, whereas most of the unwanted signal and background trend has been removed from the original G curve.

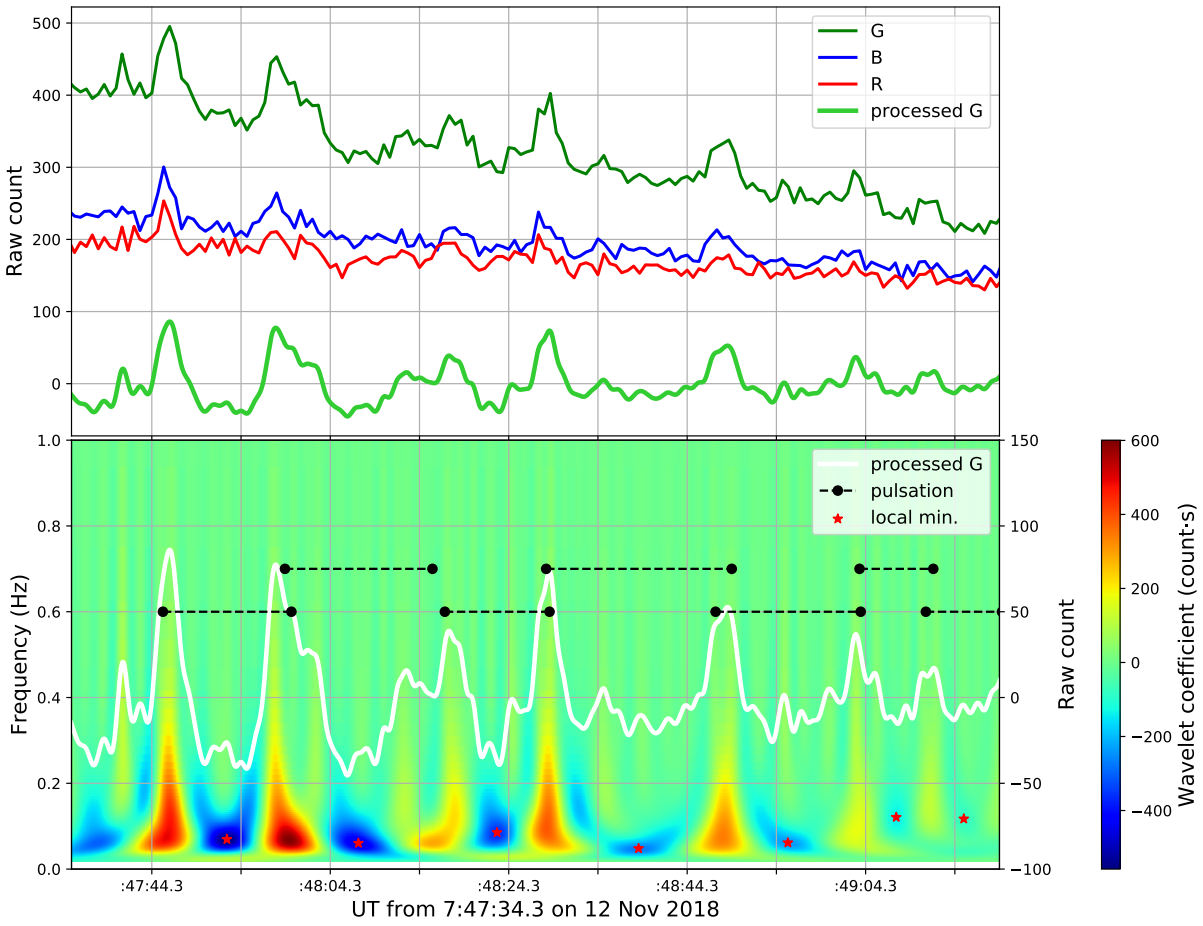

Figure 2.2: (Upper) Time-series data of PsA luminosities from 07:47:34 UT to 07:49:20 UT during Event 1. Each RGB curve corresponds to the raw count in the RGB channels of the DSLR camera. Lime-green curve labeled "processed G" represents the G-channel time series, which has been processed with the method described in the text. (Lower) Wavelet coefficient derived from wavelet transform. Black dashed lines show pulsation periods derived from local minimum values in the wavelet coefficient.

After waveform processing, we applied a wavelet transform (Daubechies, 1990) to the processed G data to extract the period of the ON–OFF switching. A Mexican hat wavelet was used as a mother wavelet. The lower panel of Figure 2.2 shows the wavelet coefficient, an integral value of products of the time-shifted mother wavelet, and the processed G. The processed G is overplotted with a white line in the same panel for reference. The Mexican hat wavelet has an upward convex shape. Thus, when the wavelet coefficient is negative (positive), the waveform at that timing is downward (upward) convex, which would correspond to the OFF (ON) phase of the PsA. We identified such candidate times of the ON and OFF phases using positive and negative thresholds for the wavelet coefficient. The duration of the period can be regarded as the peak-to-peak length of the processed G. Thereby, the period is likely to correspond to the reciprocal of the frequency at which the wavelet coefficient reaches its local minimum. We also determined the start/end times of the period by subtracting/adding half the duration of the period to/from the time when the wavelet coefficient attains a local minimum. To improve the accuracy of the data, we used the periods with their ON phases at both the start and end of the extracted period. The extracted periods and the local minimums of the wavelet coefficient are plotted in Figure 2.2 as black dotted lines and red stars, respectively. The start and end times of each black dotted line roughly correspond to the local maximum of the processed G, indicating that the periods were extracted correctly with an accuracy of a few seconds. According to the sampling theorem, periods of less than 1.3 and 1.5 s cannot be detected in Events 1 and 2, respectively. We have confirmed that the detected periods satisfy the sampling theorem. If periods that do not satisfy the theorem are detected, they should be excluded from the analysis. The signal processing described above was applied only to the periodicity analysis, and the unprocessed raw value was used for the B/G ratio analysis.

2.3 Results

2.3.1 Spatial distribution of periodicities of PsAs

Figure 2.3 summarizes the results of the periodicity analysis during Event 1. In the top panel, the estimated periods of the PsA are plotted as colored dots, which have been

superimposed on the background full-color auroral image in the altitude-adjusted corrected geomagnetic (AACGM) coordinate system (Shepherd, 2014). As shown in Figure 2.2, multiple periods were sometimes extracted at a single location. In such cases, we simply plotted the median value of the extracted periods. Hereafter, we call this type of plot a "banana plot." Note that this background image was created via overplotting all images captured during Event 1 (more than 900) in descending order of Photo ID. Thus, the background image does not always represent the actual and instantaneous structures of the aurora but demonstrates only the large-scale distribution of the aurora. In these plots, no dots are plotted when/where optical pulsations were not detected.

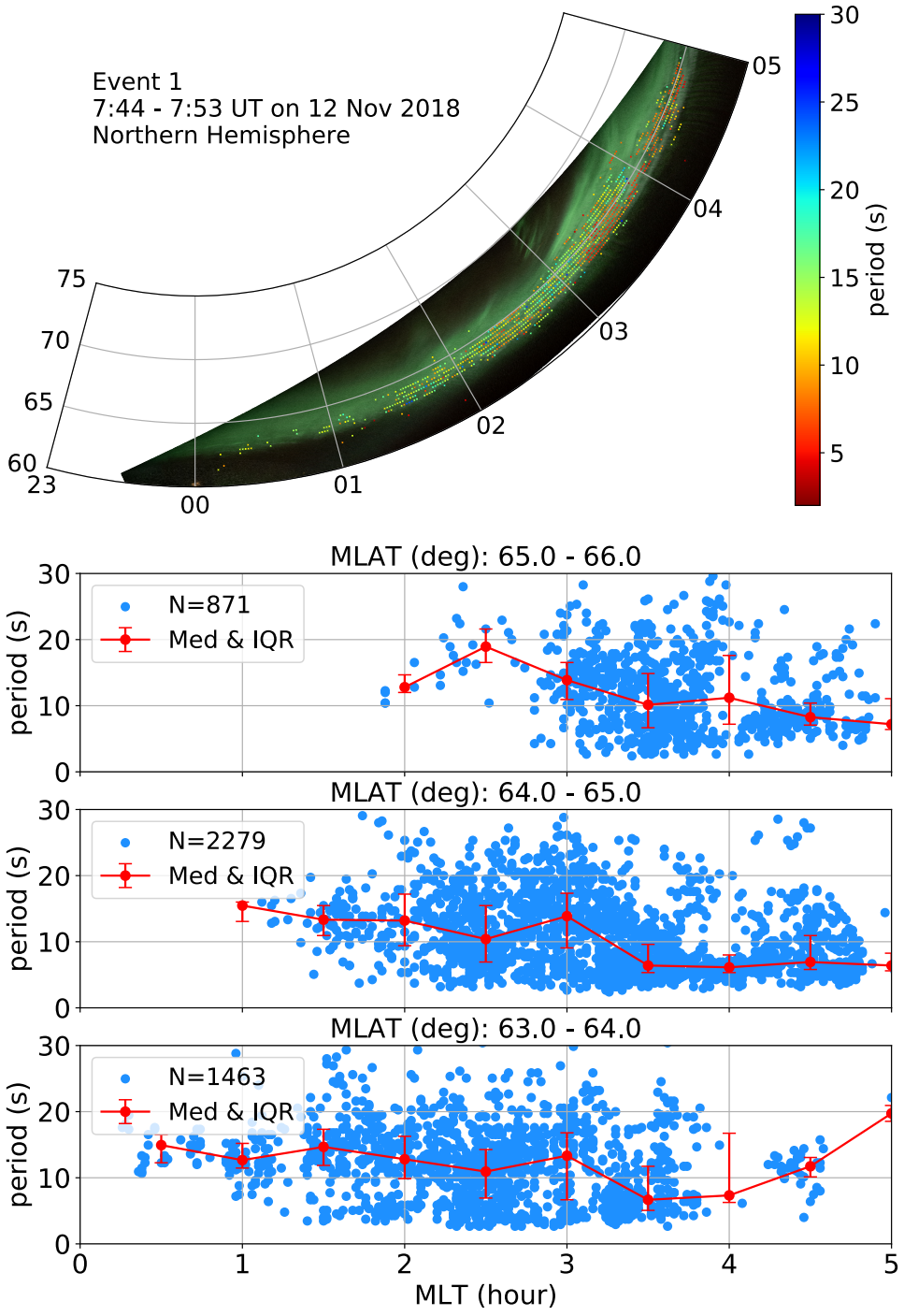

Figure 2.3: (Top) PsA observed from ISS during Event 1 in the AACGM coordinate system. Color dots show median values of pulsation periods at each point. (lower three) All extracted periods of PsA in MLAT ranges 65–66° (second), 64–65° (third), and 63–64° (Bottom). Red curves show the median (dots) and interquartile range (error bars) for every half-hour in MLT.

In the top panel of Figure 2.3, the colors of the dots are mainly greenish and yellowish, indicating that the periodicity of the PsA during Event 1 was ∼10–20 s, which is most clearly observable in the local time sector before 03 MLT. However, the red dots dominate the late MLT sector (>03 MLT), indicating that the periodicity becomes shorter ∼5–10 s in the late-morning side. To visualize the dependence of periodicity on MLT in more detail, we plotted all the extracted periods as a function of MLT in the lower three panels. Here, we have sorted the data points into three latitudinal ranges: 65–66° (top), 64–65° (middle), and 63–64° (bottom) MLAT, with which we may determine the MLAT dependence of the periodicity. The median (dots) and interquartile range (error bars) (i.e., 25th–75th percentile) are plotted with red color for every half-hour in MLT. The red curves in the lower three panels demonstrate a gradually decreasing trend in periodicity for later MLT, with some exceptions (e.g., small peaks at 03 MLT in the bottom two panels). This trend is consistent with the existence of reddish points in the later MLT (after 03 MLT) in the banana plot. However, if we examine the entire distribution of the periods in the lower three panels in detail, short periods are observed in the midnight sector (a certain number of <5 s points before 02 MLT) and, conversely, longer periods in the morning sector (>10 s points after 03 MLT). Namely, even at a single location, there was a wide variety of periodicity, indicating that the period of the PsA was highly diverse.

The same periodicity analysis was applied to Event 2 from the Southern Hemisphere, summarized in Figure 2.4 in the same format as that of Figure 2.3. During Event 2, auroras were already visible in earlier local time sectors. However, the PsA was observed only after 23 MLT; thus, only the data from 23 to 05 MLT are displayed in the banana plot. The background full-color image of the auroras reveals several discrete arcs in the higher latitude part of the FOV (mostly poleward of the −70° MLAT circle). Signatures of PsA are seen over a wide MLT range, from 23 to 04 MLT, at the lower latitude part (∼ −65° MLAT). During this interval, the optical signatures of the PsA were relatively dimmer than those in Event 1; however, the time-series analysis was able to extract their periods. In contrast to that in Event 1, the periodicity had no clear dependence on MLT, i.e., there were no systematic changes in the colors of the dots. The lower three panels show the periodicity with respect to MLT in three MLAT ranges: −66 to −67° (top),

−65 to −66° (middle), and −64 to −65° (bottom) MLAT. The total number of extracted periods was a few times lower in Event 2 than in Event 1. As already inferred from the banana plot, the periodicity had no systematic dependence on the MLT and MLAT. However, the periods sometimes changed in a few seconds, even for small differences in MLT. For example, at ∼1.5 MLT, as shown in the middle panel, the median of the periods became longer than that in the surrounding MLT sectors, and there were a few samples with periods shorter than 10 s. Although Events 1 and 2 had differences in terms of their periodicities exhibiting (or not exhibiting) dependence on MLT, the results are similar in the sense that the periodicities were highly diverse and had broad distributions even at single locations.

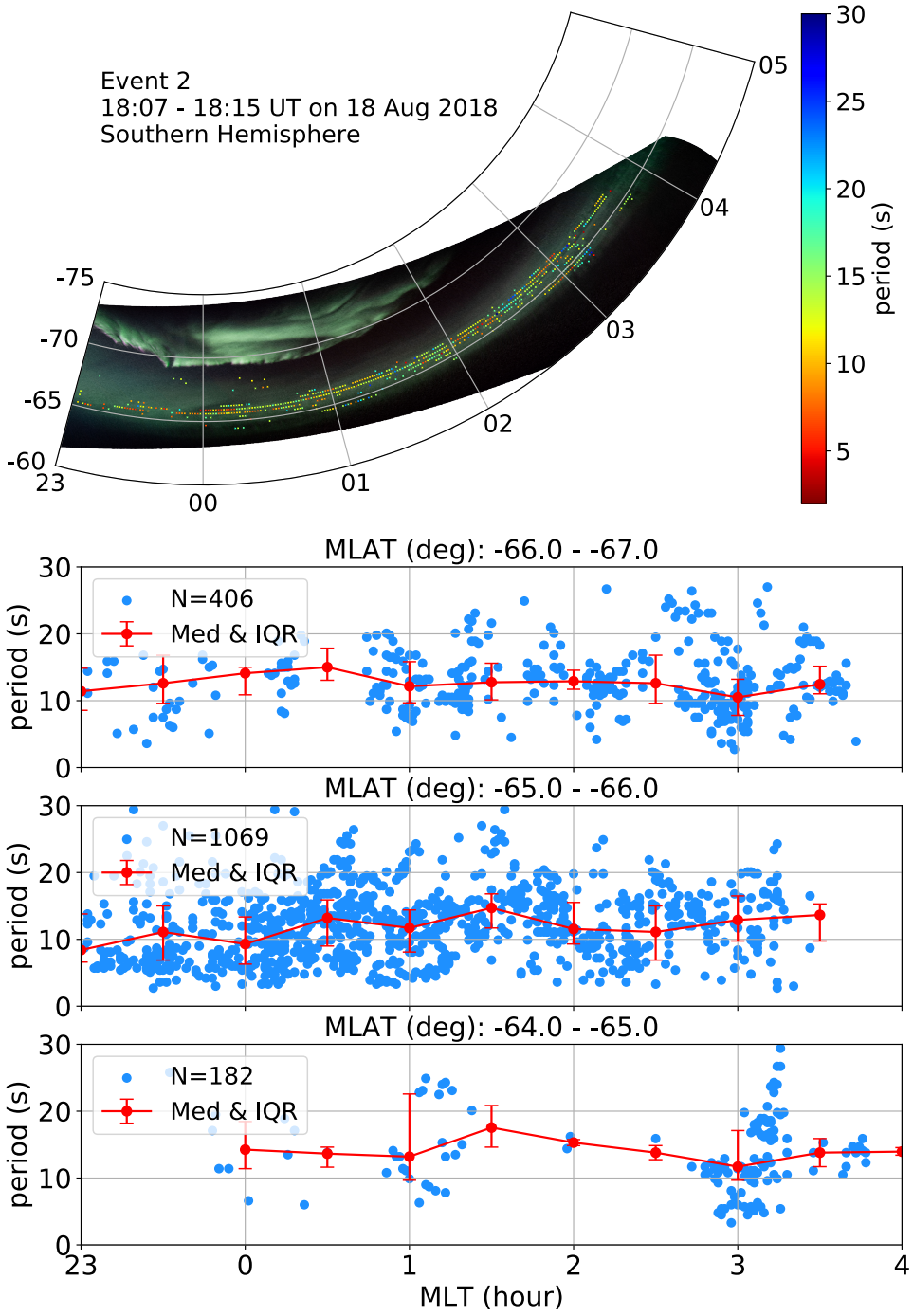

Figure 2.4: (Top) PsA and discrete aurora observed from ISS during Event 2 in the AACGM coordinate system. Color dots show median values of pulsation periods at each point. (lower three) All extracted periods of PsA in MLAT ranges −66 to −67° (second), −65 to −66° (third), and −64 to −65° (Bottom). Red curves show the median (dots) and interquartile range (error bars) for every half-hour in MLT.

2.3.2 Spatial distribution of B/G ratio

Here, we evaluate the feasibility of using RGB-color DSLR images for estimating the energies of precipitating electrons using the blue-to-green ratios (B/G ratios) of the ISS images. If the assumption that the B and G channels are respectively sensitive to the 1NG emission and the green line is actual, then the higher B/G ratio means the higher energy of PsA electrons. The validity of this assumption is discussed in detail in Section 2.4.2. The banana plot in Figure 2.5 shows the B/G ratios calculated from the raw RGB images of Event 1. The B/G ratio values are displayed with a color scale from 0.3 to 0.8, where values in the regions without auroral emissions are colored black. The FoV of a single image is traced using a dashed white line in the banana plot. This fan-shaped FoV swept the entire area as the ISS progressed along its orbit; thus, the data shown in the banana plot contain both temporal and spatial variations, and this type of plot can be used only for visualizing large-scale distributions of the parameter. The distribution of B/G ratios in the MLAT and MLT coordinate system exhibited an increasing trend from the midnight to morning sector, shown by the reddish points in the equatorward part of the oval in the 04–05 MLT sector.

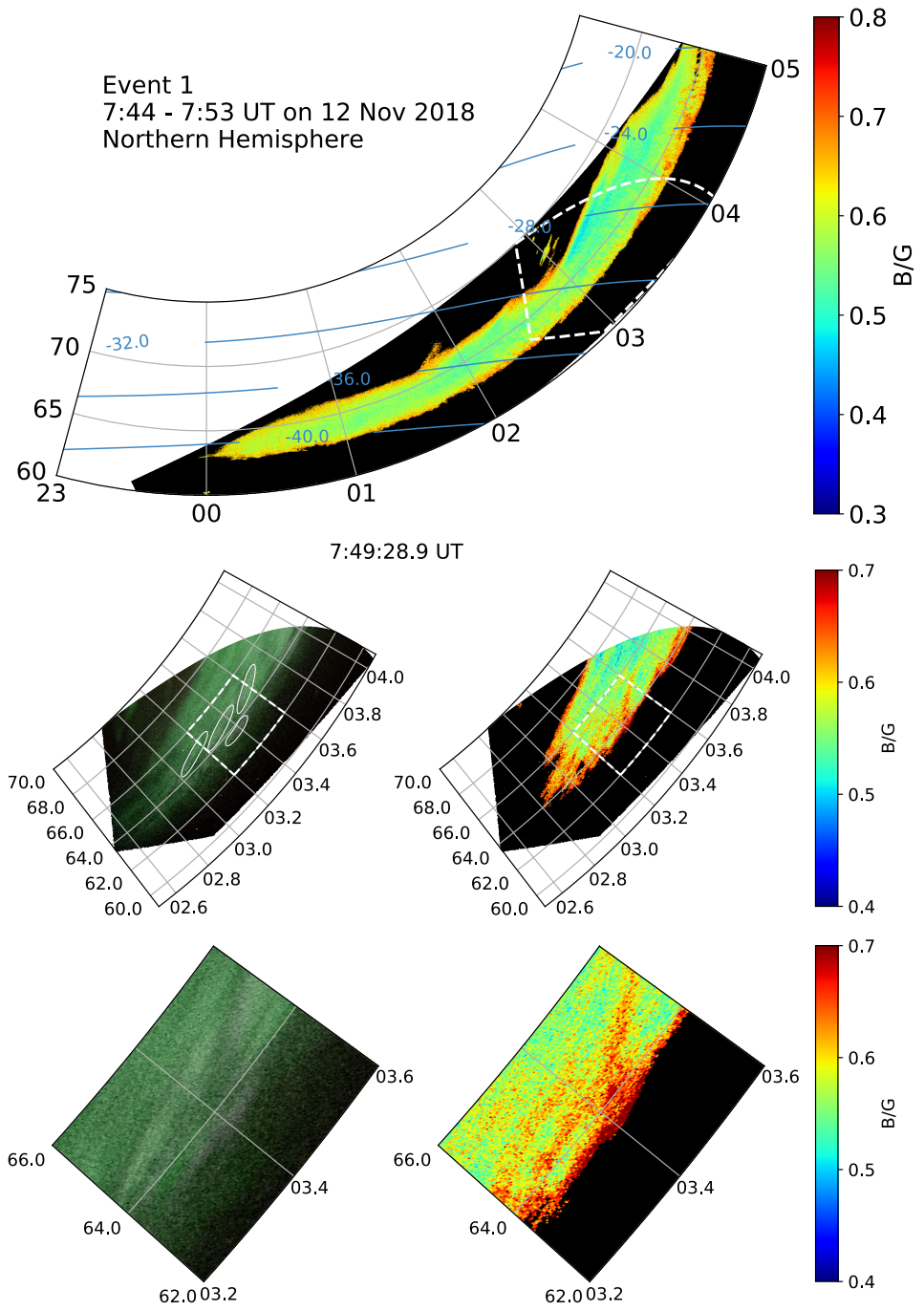

Figure 2.5: (Top) B/G ratios of PsA observed from ISS during Event 1 in the AACGM coordinate system. White dashed fan-shaped region shows FOV at 07:49:28.9 UT (corresponds to the middle panel). Blue contour lines show the solar elevation angle at 07:53 UT. (Middle) RGB image (left) and B/G ratios (right) of PsA observed at 07:49.28.9 UT. White dashed box shows the region magnified in the bottom panel. (Bottom) Magnified images from the middle panel.

The middle panels show the RGB image (left) and B/G ratio image (right) at 07:49:28.9 UT. These are not combined images but, rather, snapshot images captured within the FOV shown by the dashed white lines in the banana plot. Detailed spatial structures of PsA patches are outlined with solid white lines, which are quite different from what is shown in the banana plot. From these snapshot data, patches of the PsA were observed only on the equatorward part of the aurora oval, in which the B/G ratio was significantly higher. To compare the spatial structures of the PsA patches with the B/G ratios more directly, the data in the white dashed boxes in the middle panels are magnified in the bottom panels. According to the image, the B/G ratio increased to $\sim$0.7 within the brighter region (pinkish and whitish patches in the RGB image). By contrast, within some darker regions (dim areas in the RGB image), the B/G ratio decreased below the background level at $\sim$0.5.

The top and middle panels of Figure 2.6 display the B/G ratio data of Event 2 in the same format as that of Figure 2.5. The bottom panel of Figure 2.6 shows the B/G ratio along the cross-section at $-65.4 \pm 0.0005^\circ$ MLAT in the banana plot as a function of MLT. The red curve represents the median calculated for every half-hour in MLT. In the banana plot, two L-shell aligned regions are visible, which may be a signature of a double oval (Elphinstone et al., 1995). The one at the high-latitude side was a discrete aurora; the B/G ratio was mostly low in this region. However, the B/G ratio was locally high in the pre-midnight sector poleward of -70° MLAT. This reddish area could correspond to the lower-altitude border of the discrete aurora, which appears in pink in the RGB image (see Figure 2.4). This localized enhancement was introduced because we mapped the rim-direction images onto the horizontal plane, which caused us not to recognize the altitude variation in emission color as a horizontal spatial structure. The effects of the rim-direction observation are discussed in detail in Section 2.4.2.

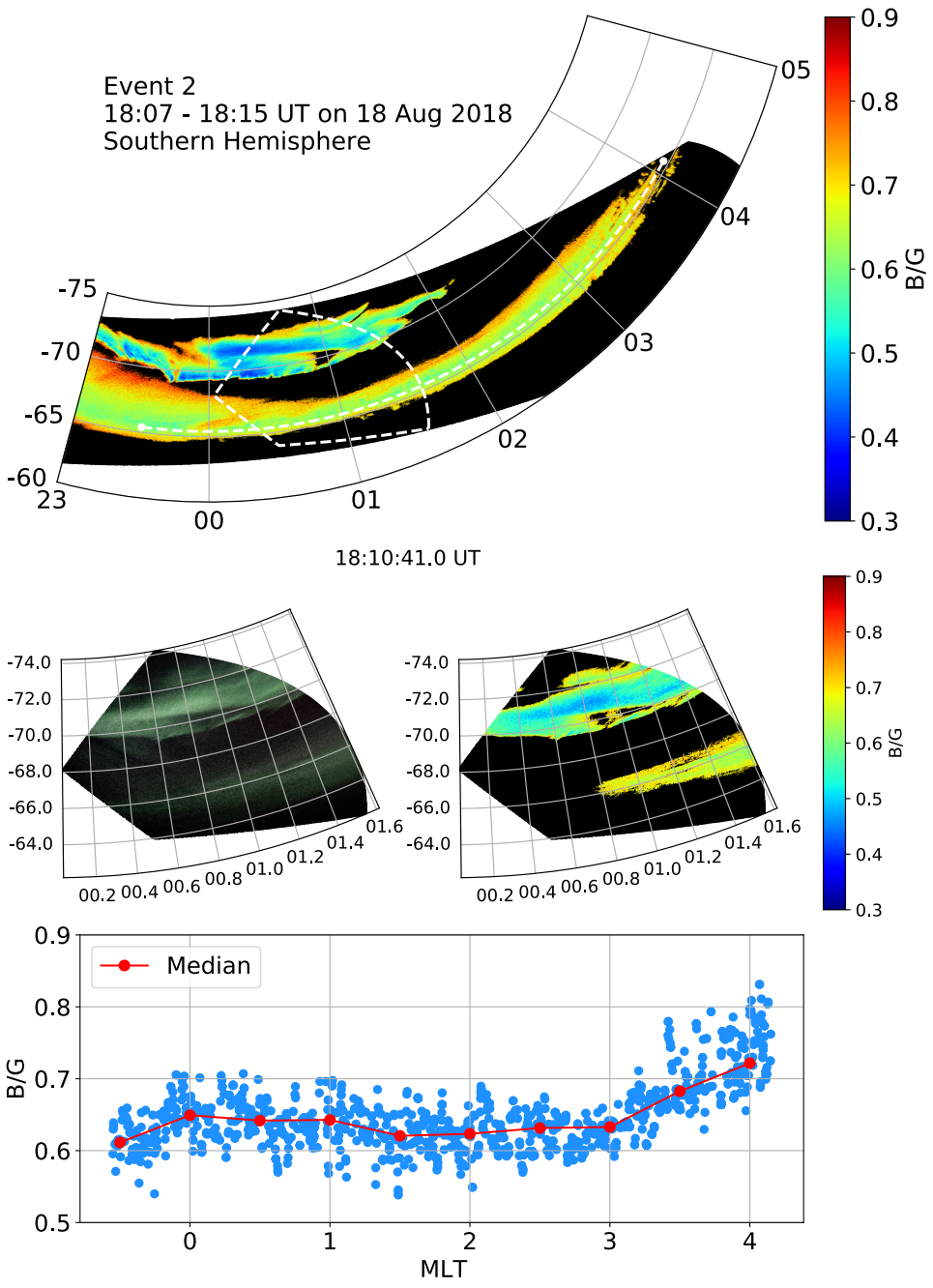

Figure 2.6: (Top) B/G ratios of PsA and discrete aurora observed from ISS during Event 2 in the AACGM coordinate system. White dashed fan-shaped region shows FOV at 18:10:41.0 UT (corresponds to middle panel). White dashed line shows a cross-section plotted in the bottom panel. Blue contour lines show the solar elevation angle at 18:15 UT. (Middle) RGB image (left) and B/G ratios (right) of PsA observed at 18:10:41.0 UT. (Bottom) B/G ratios on white dashed line in the top panel (at $-65.4°$ MLAT) as a function of MLT.

The other oval feature at the low-latitude side comprises diffuse auroras; the B/G ratio was higher than that in the discrete aurora at the higher latitude. These trends can also be observed in the middle panels, where snapshots of the RGB and B/G ratios are shown. Moreover, the pre-midnight sector shows some high B/G ratio values at -70° MLAT, but the optical emission was dim in that region, which implies that, when using the B/G ratio, we should check whether the aurora is sufficiently bright in the region of interest. Furthermore, the B/G ratio becomes slightly higher in the morning sector than in the midnight sector. This tendency was observed during Event 1 and was also identified for Event 2, in the bottom panel of Figure 2.6. In the region of the PsA, which belongs to the main oval, it was challenging to identify the brighter and darker regions from single images (i.e., in the middle panels). However, the B/G ratio exhibits a slightly increasing trend in the top and bottom panels; the B/G ratio attains a minimum ($\sim$0.6) before 00 MLT and a maximum value ($\sim$0.7) at $\sim$04 MLT. Although distinguishing the brighter and darker regions of the PsA in Event 2 was difficult, the B/G ratio tended to be higher in the morning sector than in the midnight sector for both Events 1 and 2.

2.4 Discussion

2.4.1 Spatial distribution of periodicities of PsAs

Thomas and Rothwell (1979) measured the periodicities of PsAs at two sites: Poker Flat ($\sim 63^\circ$ MLAT), Alaska; and Andøya ($\sim 67^\circ$ MLAT), Norway. Their results showed that the periodicity is longer at higher latitudes and that the pulsating periods are close to the bounce period of a few keV electrons. Therefore, they suggested that the periodicity of PsA is associated with the bounce period of trapped electrons in the magnetosphere. Duncan et al. (1981) operated photometers at four sites in Canada and performed a similar analysis of the latitudinal dependence of the periodicity. Their results also showed that the period was longer at higher latitudes, but the dependence was observed only in a limited period range of less than 10 s. Both sets of data were obtained at different times and locations with insufficient FoVs not covering the entire region of the PsA; thus, it was difficult to investigate the spatial (i.e., latitudinal) dependence of the periodicity in detail. In this study, we examined the spatial (MLAT and MLT) dependence of the

periodicity under almost the same geomagnetic conditions by capturing entire regions of the PsAs in a quiet, short time interval. This large-scale observation of PsAs may provide clues regarding the factors influencing the periodicity.

Both the banana plot and scatter plots in Figure 2.3 show that, for Event 1, the periodicity of the PsA exhibited no monotonic dependence on MLAT but tended to be shorter in the morning sector. At the MLAT from 64 to 65°, the median period was 14 s in 1.5 MLT and was shortened to 7 s in 4.5 MLT. To confirm whether this trend reflects the change in the bounce period of the trapped electrons, we calculated the lengths of the magnetic field lines using the T04 model (Tsyganenko and Sitnov, 2005). At 64.5° MLAT, the length of the field lines was 13 R_E for both 1.5 and 4.5 MLT, and the bounce period of electrons with 3-keV energy was 5.3 s. The change in the bounce period was less than 0.1 s for the 3-h difference in MLT, and there was no trend for the bounce period to shorten by 8 s in the morning sector. The typical period derived from our analysis was 10 s. If this pulsation period is determined by the bounce period of the trapped electrons, the energy of the electrons was 800 eV, which is exceedingly low to explain quasi-periodic optical emissions of PsA at lower than 100 km reported in Partamies et al. (2017). In contrast to Event 1, which exhibited a shorter pulsating period in the morning sector, Event 2 demonstrated no monotonic spatial dependence on MLT, as shown in both the banana plot and scatter plots in Figure 2.4. Three scatter plots show that the typical pulsation period was ∼15 s, and that the energy of electrons with a bounce period of 15 s at −65.5° MLAT was ∼500 eV at both 00 and 03 MLT, which was also lower than the typical energy band of electrons causing the main pulsation. Therefore, the results of this study do not lead to the suggestion that the periodicity of a PsA is influenced by the bounce period of the trapped electrons.

In the banana plot and median of scatter plots in Figure 2.3, the pulsation period of the PsA tended to shorten toward the morning sector. However, in Figure 2.4, no such noticeable shortening trend was observed in the MLT direction. Since this chapter conducted the event study, the results may not exhibit universal characteristics of PsA. In both Events 1 and 2, however, the pulsation period had broad distributions that could exceed 20 s even at a single point (e.g., at 03 MLT in the middle scatter plot in Figure 2.3). Hence, a single indicator, such as the median, may not be the best

parameter to describe spatial dependence. Even in Event 1, the shortening trend was not necessarily monotonous because there was a location at ∼03 MLT where the period became locally longer. Based on these observations, it would be appropriate to infer that the periodicity of a PsA does not have a clear and monotonic spatial dependence on MLT/MLAT and that their beats change locally. Thus, the periodicity of PsA should depend on some local parameters, such as the gradient of magnetospheric electron density and temperature, rather than on parameters that change monotonically on large scales, such as the bounce period of trapped electrons or the magnetic field intensity. In support of inconsistency with the length of the magnetic field line, Li et al. (2011) reported that the modulation of chorus waves is related to the electron density variation at the source region. Ozaki et al. (2015) demonstrated that the periodicities of PsAs and chorus waves change depending on the curvature of the magnetic field line at the equatorial source region. Our results also suggest that the periodicities of PsAs are closely associated with the generation process of chorus waves controlled by the local parameters (density, temperature, and gradient of the magnetic field line, etc.) in the magnetosphere. Davidson (1979) has suggested the relaxation-oscillation model as an origin of the periodicity of PsA. Demekhov and Trakhtengerts (1994) have suggested the flow-cyclotron maser model to explain the periodicity. Such a spontaneous process should also be the essential factor controlling the periodicity of PsA.

2.4.2 Validity of B/G ratio as proxy for the energy of PsA electron

McEwen et al. (1981a) performed multi-wavelength optical observations with a ground-based photometer and direct simultaneous observations of the precipitating electrons with a sounding rocket. They compared the values of characteristic energy (E_0) from the rocket observations with that estimated from the intensity (Rayleigh) ratios of the 557.7-nm and 427.8-nm emissions. Both E_0 values, i.e., those from in-situ observations and estimated from the optical observations, were high during the ON phase of the PsA and low during the OFF phase and agreed quantitatively within 1 keV. Steele and McEwen (1990) also performed simultaneous observations of discrete and diffuse auroras using particle observations from a low-altitude orbiting satellite and optical observations with a photometer.

They determined a negative correlation between the intensity ratio 5577/4278 and E_0 and inferred that E_0 is expressed by the following equation: $5577/4278 \sim 5.6E_0^{-0.3}$. Note that their ratio has an inverted numerator and denominator to the B/G ratio. Although they suggested that the estimation of E_0 using the 6300/4278 ratio was more accurate than that using the 5577/4278 ratio, the lifetime of the 630.0-nm emission (∼110 s (Jones, 1971, 1974)) is exceedingly long to infer the energies associated with auroras that have fast temporal variations, i.e., shorter than several tens of seconds. Hence, the 5577/4278 ratio is more suitable than the 6300/4278 ratio for estimating the energies of PsA electrons.

Because our analysis used the DSLR camera with broader transmission characteristics than a typical photometer, we should not simply regard the B channel as the 427.8-nm emission and the G channel as the 557.7-nm emission without any evidence. Since the DSLR camera used in this study is mounted on the ISS, it is impossible to conduct a calibration experiment and derive transmission characteristics of RGB channels. However, de Miguel et al. (2019) derived the transmission characteristics of the same model of the DSLR camera used in this chapter (Nikon D5). According to their Figure 1, the band where the relative response of the B channel exceeds 10% is 400–520 nm. According to Jones (1974), there are many other emission lines of auroras in this bandwidth besides 427.8 nm, but all emission lines, which are brighter than 10% of those of the 427.8-nm emission, belong to the 1NG band. The auroral spectra in Svalbard, Norway, as measured by Sigernes et al. (2008) (their Figure 7), also showed no bright emission lines in this band other than the 1NG band. However, because the emission intensity at 557.7 nm is 6–7 times greater than that at 427.8 nm, contamination of the green line should be considered separately. In the transmission characteristics of the B channel of de Miguel et al. (2019), the relative responses for the 427.8-nm and 557.7-nm emission are 60% and 5%, respectively. Thus, when the ratio of the emission intensities at 427.8 nm and 557.7 nm is 1:6, the ratio of their contributions to the B channel is 2:1. Since 33% of the total is due to the emission at 557.7 nm, we cannot conclude that the B channel detects only the 427.8 nm emission. By contrast, applying the same procedure, the contribution ratio in the G channel is calculated to be 1:180, indicating that the G channel is almost entirely composed of the 557.7-nm emission. Therefore, compared to the G channel, the B channel has a more significant contribution of the 1NG band, including 427.8 nm, and

is more sensitive to high-energy electron precipitation. Although the G channel contains the emission at 630.0 nm, its contribution was found to be less than 1% by applying the same calculation. This estimation is based on a theoretical calculation using the results of the previous studies, but in the upper panel of Figure 2.2, the peak of the intensity in the B channel occurred slightly (<1 s) earlier than that in the G channel at some points (e.g., at 7:47:45 and 7:48:27). The 1NG band is emitted immediately after excitation, whereas the emission at 557.7 nm is delayed by 0.7 s from excitation (Jones, 1971, 1974). Therefore, the timing difference in the emission peaks of the B and G channels suggests that they are sensitive to the 1NG band and the 557.7 nm emission, respectively.

Due to its wide bandwidth, the DSLR camera receives various background lights besides auroras. These include, for example, airglow, city lights, and reflected light from the ground and clouds. However, these may not have systematic dependence on the B/G ratio. In the current cases, there were no city lights in the auroral region. The banana plots in Figures 2.3 and 2.4 also show that the non-auroral region is almost completely dark. Therefore, the contamination of reflection light and airglow on the B/G ratio could be minor. Comparing Figure 1 in de Miguel et al. (2019) with the spectrum of the night airglow (Broadfoot and Bellaire Jr., 1999; Krassovsky et al., 1962), there are no bright emission lines in the B channel band. The G channel band contains emissions at 557.7 nm (OI) and at 589.6 nm (NaD). The intensity (Rayleigh) of the OI emission is ∼10% of the PsA emission at 557.7 nm, and the NaD emission is several times fainter than the OI emission. Considering these points, the contribution of the G channel is mostly (∼90%) due to the PsA emission at 557.7 nm, and the B channel has almost no atmospheric light effect; thus, the qualitative features of the B/G ratio is not interfered with by the non-auroral emissions. In addition to the background light, in the morning sector, the purple aurora often appears due to the resonant scattering by sunlight (Shiokawa et al., 2018, 2019). Such a purple emission is seen in the higher-altitude parts of discrete auroras. Although it has not been reported that a PsA is also colored purple due to the resonant scattering, we have drawn contours of the solar elevation angle at an altitude of 100 km in the banana plots in Figures 2.5 and 2.6 to evaluate the effect of sunlight. In the aurora oval in Event 1, the solar elevation angle took a maximum of -20° at 5 MLT. Since the astronomical twilight ends at a solar elevation angle of -18°, the oval is unlikely to be

affected by sunlight. The oval in Event 2 also has solar elevation angles less than $-20°$, which supports that the sunlight does not affect the increasing trend of the B/G ratio.

In addition to the wide wavelength bands, the observations from the ISS have a different spatial resolution than the typical ground-based observation. Because the camera captures auroras in the rim direction and then we project the image onto the horizontal plane, there is a spatial distortion in the shape of auroras. This effect is smaller if an aurora is thinner in the altitude direction. As shown by Nanjo et al. (2020), because PsAs are generally thinner than discrete auroras, patches of PsAs whose horizontal extent is several tens of kilometers can be projected and resolved with similar accuracy to observations by ASIs.

The incident angle of the line-of-sight (LOS) vector depends on the location in the ISS image. Therefore, the B/G ratio can be biased in some locations. The incident angle is more significant at the back of FOV (often at the morning side) and smaller at the front of FOV (i.e., closer to the camera). Because it also depends on the projected altitude of the aurora, further attention is needed when the blue and green emissions are emitted at different altitudes. According to Jones et al. (2009), the altitudinal thickness of a PsA is 15–25 km; thus, we assumed that the 1PG was emitted at 90–100 km (B layer) and that the green line was emitted at 100–115 km (G layer). In Event 1, because the difference between the incident angle at 100 km and that at 115 km was small (less than $1°$), the difference in the incident angle between the two layers was not considered. The thicknesses of the B and G layers were assumed to be 10 and 15 km, respectively. Therefore, the LOS vector penetrated the B and G layers with distances of $10 \sec\theta$ and $15 \sec\theta$ km, respectively. Here, θ is the incident angle. Because the value of $10 \sec\theta / 15 \sec\theta$ is equal to 10/15, the B/G ratio does not depend on the incident angle of the LOS vector.

Because the PsA patches were not large in most cases, it was not clear whether the LOS vector penetrated through the auroral emission layer all the way from the top to the bottom. The horizontal size of a patch is several thousands of km^2 (Humberset et al., 2018; Partamies et al., 2019), and the vertical thickness is 15–25 km (Jones et al., 2009). As an example, let us consider an aurora that is 100 km in the horizontal direction and 25 km in the vertical direction. A LOS vector penetrating the emission layer from the top to the bottom has an incident angle of $76°$ ($= \arctan(100/25)$) or less. Because the

incident angles of the LOS vectors in the middle panel of Figure 2.5 range from 30 to 75°, this effect can be canceled at least at one point of each PsA patch in FOV. Near the edges of the patches, however, it was unlikely that the LOS vector penetrated from the tops to the bottoms of the patches. In this case, a single LOS vector may penetrate the patch and background precipitation regions, but the background precipitation will not be affected significantly because the flux is ∼1/10 of the ON phase of the patch (Miyoshi et al., 2015b). This effect would be small based on the averages of B/G ratios inside the patches. Therefore, because of the influence of the incident angle, B/G ratios in rim-direction observations should be used to estimate energy variations in wide areas of more than a few hundred kilometers rather than to estimate the fine-scale energy variation in a single patch.

The above-mentioned geometric problems do not have to be concerned if both layers were distributed at the same altitude, as in Figure 7 in Partamies et al. (2017). However, because the same altitudinal distribution means that there is little difference in the energy of PsA electrons, the B/G ratio may not work as an index of the energy of PsA electrons. By contrast, if PsA electrons have relatively higher energy and the quenching of the 557.7-nm emission occurs, the B/G ratio will be higher. Therefore, the B/G ratio might be more effective in moderate to severe events where the auroral color changes than in quiet ones where no quenching of the 557.7-nm emission occurs at all regions and times.

2.4.3 Spatial distribution of B/G ratio

Hosokawa and Ogawa (2015) investigated the ionospheric E region electron density profile for 21 intervals of a PsA using data from the European Incoherent Scatter (EISCAT) radar. The results suggested that the peak altitude decreases and the peak electron density increases in the morning sector. Later, Partamies et al. (2017) analyzed the peak emission altitude for ∼400 cases of a PsA using the all-sky cameras of the MIRACLE network. They concluded that there is no significant MLT dependence on the altitude of PsAs before 6 MLT. Tesema et al. (2020) combined ground-based optical observations and particle observations from the low-Earth orbiting satellites DMSP and POES to derive the MLT dependence of the flux of PsA electrons. They found no overall MLT dependence in the flux, but they also noted a slight increase in the flux after 6.5 MLT at a higher energy

band (>30 keV) simultaneously. Kawamura et al. (2020) measured a lifetime of oxygen atoms that produce the 557.7-nm emission by a photometer at Tromsø, Norway. They estimated the altitude of PsAs by using the measured lifetime. Their result exhibited that the altitude decreased in the morning sector, especially after 6 MLT. A common implication of these studies is that the energy of PsA electrons increases after 6 MLT.

In this study, the B/G ratio increased from 3.5 MLT in Event 1 to 3.0 MLT in Event 2. Although there is a 3-h difference in the timing of the increase between the previous and present studies, the qualitative increasing trend in the morning sector is consistent. The difference in the timing may be because the present study is a case study while the previous studies are statistical studies. Another possible cause is the difference in latitude. Hosokawa and Ogawa (2015) and Kawamura et al. (2020), who suggested the increase in the energy of PsA electrons, performed their observations in Tromsø, Norway (MLAT: 66.7°). The increase in the B/G ratio observed in Event 1 started at an earlier MLT and lower MLAT, and it started at 3.5 MLT in regions with an MLAT lower than 65°. The increase in the B/G ratio at 66.7°MLAT was observed from ∼4.5 MLT, which is still different from the timing in the previous studies, but the difference in the MLAT may explain the gap. Based on the factors mentioned above, the B/G ratio, which can be a proxy for the energies of precipitating electrons, becomes higher in the morning sector, suggesting that the energies of PsA electrons are higher in the morning sector.

Sandahl et al. (1980) launched a sounding rocket into a PsA and observed the characteristic temporal variations of electron energy spectra. Their in-situ observation showed that pulsation in the electron energy spectrum occurs only in the energy range above 3–4 keV. More recently, Miyoshi et al. (2015b) compared in-situ energy spectra from the REIMEI satellite with simultaneously obtained optical data at the magnetic footprints of the satellite. They determined that the ON–OFF switching of optical pulsation is caused by energetic electrons above 3 keV and that continuous (i.e., without pulsation) background precipitations occur below 1 keV which has been known as drizzle precipitations (Evans et al., 1987). In our analyses, the behavior of the B/G ratio is in good agreement with the aforementioned energetic characteristics of PsA electrons. That is, the energy is higher within the brighter (white/pink) regions than in the background regions. Furthermore, we observed stable, faint-green emissions in areas where optical pulsation was

not detected (i.e., areas without dots in the banana plot of Figures 2.3 and 2.4), which may correspond to the background continuous precipitations suggested by Miyoshi et al. (2015b).

Brown et al. (1976) set up two video cameras 10 km away from each other and tried to estimate the lower cut-off altitude of PsA and discrete aurora emissions. The altitude of PsAs was then determined to be relatively lower than that of discrete auroras. In some cases, the altitudes were less than 90 km. More recently, Kataoka et al. (2013) conducted a similar experiment using two DSLR cameras 8 km away from each other. They estimated the altitude distributions of PsAs and discrete auroras by producing an altitude map of the emissions in 2D. Through this approach, they demonstrated that discrete auroras showing ray structures exhibit broad altitude distributions mainly in 100–130 km and, sometimes, up to ∼250 km, whereas optical emissions of PsAs are distributed in a narrow altitude range, from 80 to 90 km. The results of these previous studies indicated that the energies of precipitating electrons are higher during a PsA than during a discrete aurora. In our study, the B/G ratio was demonstrated to be higher in the region of PsA compared with that of the discrete aurora. This result is in good agreement with those of previous studies because a high B/G ratio may be a sign of higher-energy electron precipitation causing auroral emissions at lower altitudes.

As shown in the banana plot of Figure 2.5, in the morning sector of Event 1, the B/G ratio increased significantly in the equatorward part. By contrast, the B/G ratio distribution in Event 2 did not exhibit a similar characteristic. This tendency may be explained by the precipitation of relativistic or sub-relativistic electrons from the radiation belt, as reported by Miyoshi et al. (2015a), Miyoshi et al. (2020), and Miyoshi et al. (2021). As shown in the banana plots of Figures 2.3 and 2.4, the aurora oval was located ∼2° MLAT equatorward in Event 1 as compared with that in Event 2. From Figure 2.1, the SYM-H index decreased more, and the solar wind speed was higher in Event 1 than in Event 2. From the difference in background conditions between the two events, the radiation belt may have been more active in Event 1 than in Event 2, and more energetic electrons may have been precipitated into the ionosphere. This could be a reason for the higher B/G ratio in the equatorward side of the morning sector during Event 1.

2.5 Summary

We analyzed the periodicity and color (i.e., the ratio of blue and green channels) distributions of PsAs using DSLR camera observations from the ISS. The data were obtained in short periods, ∼10 min, during the midnight to morning sector (23–05 MLT). The results are summarized as follows:

1. The periodicities of the examined PsAs did not exhibit a systematic spatial dependence on MLAT or MLT, which was inconsistent with previous studies (Thomas and Rothwell, 1979; Duncan et al., 1981).

2. The periodicities of the examined PsAs varied widely from location to location, suggesting that local conditions in the magnetosphere, rather than the large-scale structure, contribute to determining periodicity.

3. B/G ratios were higher in the morning sector than in the midnight sector and higher in brighter regions than in darker regions, which are consistent with characteristics of PsA electrons reported by previous studies (Hosokawa and Ogawa, 2015; Miyoshi et al., 2015b). This result implies that B/G ratios could be used as proxies for the energies of precipitating electrons qualitatively.

4. In the morning sector, an increase in the B/G ratio in the equatorward part of the aurora oval was identified during a small magnetic storm, suggesting the precipitation of more energetic electrons from the radiation belt in the region of the PsA.

These results demonstrate that conjugate observations with satellites measuring the temperatures and densities of electrons will enable us to deeply discuss the factors that influence the periodicities of PsAs. As mentioned in Section 1.4, in the recent decade, citizen science has been conducted with commercial digital cameras, which has significantly contributed to scientific studies of auroras (e.g., MacDonald et al., 2018; Palmroth et al., 2020). However, most of these methods have been employed only for identifying the forms and locations of auroras, and their usage remains limited at this stage. The current analyses of two PsA events confirm the feasibility of estimating the energies of

precipitating electrons from full-color commercial digital camera images. In Chapter 3, we evaluate the possibility of using B/G ratios as more quantitative proxies for the energies of precipitating electrons, which will contribute to the further development of citizen science with DSLR cameras.

Chapter 3

Cloning the ISS Observation on the Ground

3.1 Introduction

The analyses described in Chapter 2 suggest that the B/G ratio obtained from the Nikon D5 onboard ISS helps evaluate the spatial characteristics of the average energy of auroral electrons. In order to investigate the correspondence between the B/G ratio and the characteristic energy of precipitating electrons more empirically, the Nikon D5 was installed at the Ramfjordmoen field station to make the same observations as the one done from the ISS. Since the European Incoherent SCATter (EISCAT) radar, which can estimate the average energy, is operative in the same location, the relationship between the B/G ratio and the average energy can be evaluated by observing the same aurora simultaneously. The primary consideration when performing such an observation is the wear and tear of the shutter unit of the camera. The time resolution of observations at the ISS is 0.5 to 1.0 seconds. The shutter unit of a DSLR camera generally breaks down after photographing several hundred thousand times. This means that observations can be stopped within a few weeks if we take photographs throughout the night. In order to obtain a large amount of data with a single camera, it is necessary to make observations only when the aurora appears. In order to implement this function, we have established a deep-learning model that can detect auroras in the all-sky image obtained by the digital camera installed at the same observatory for weather monitoring. This model can evaluate if the aurora currently appears over Tromsø. Because this information is beneficial not only for scientists observing auroras but also for tourists viewing auroras, we have developed a website to

monitor the classification results. In the following, we first describe how the model was developed and the accuracy evaluation of the model compared to visual classification results. Then, we describe the results of the observations by the Nikon D5 synchronized with the auroral appearance.

The occurrence of auroras has been studied with the naked eye since the 18th century. The annual and seasonal variations in the occurrence of auroral displays were investigated using 1000-time naked-eye observations at two sites in southern Finland over a 100-year period from 1748 (Nevanlinna, 1995). According to this study, the auroral occurrence has an 11-year cycle, similar to the solar activity, and a few auroras were observed during the Dalton Minimum, one of the periods of the lowest solar activity (Eddy, 1976). They also suggested that similar to the geomagnetic storms, the occurrence rate of auroras is higher in autumn/spring and lower in summer/winter. However, since they observed the aurora without any optical instruments, the statistical significance of their results is relatively low. Another study has visually classified images observed by all-sky cameras (ASCs) to derive the occurrence rate of auroras (Nevanlinna and Pulkkinen, 2001). They captured images for 100000 hrs using ASCs in Finland and Svalbard over a 24-year period from 1973 and derived the local time dependence of the auroral occurrence rate. Similar studies using ASCs in other high-latitude regions were conducted later, and a common tendency was that the auroral occurrence peaked just before/after the magnetic midnight (Sheret, 1963; Blackie, 1964; Blundell, 1967). However, classifying data with the naked eye is physically tough and time-consuming, and it is difficult to apply such an approach to analyze recent data with a much higher temporal resolution.

To classify the current large-volume optical data, it is more efficient to use an automated classification performed via artificial intelligence (AI) rather than using the human eye. Automated classification techniques for auroral images using hidden Markov models (Yang et al., 2012), k-nearest neighbor (kNN) (Syrjäsuo and Donovan, 2002, 2004) and support vector machines (SVMs) (Rao et al., 2014) had been developed in the last decade. To further improve accuracy, classification methods combining multiple algorithms were proposed and applied to the dayside auroras (Wang et al., 2010; Fu et al., 2009; Zhong et al., 2018). However, these algorithms have been difficult to use casually because their accuracy depends on manually selected feature values. This drawback was overcome by

the deep-learning technique, which automatically selects such values. A method for classifying daytime auroras using the deep neural network (DNN) was then proposed (Jia et al., 2015), but this method was not used for conducting a statistical analysis of the auroral occurrence because it cannot classify non-auroral images. Later, a study that classified gray-scale all-sky images including non-auroral images using DNN (Clausen and Nickisch, 2018) performed the classification with 82% accuracy; the images were classified into six classes: *Arc*, *Discrete*, *Diffuse*, *Cloudy*, *Moon*, and *Clear*. The authors of this study also suggested using other classes such as *auroral activity with moon contamination*, but whether it could show a high accuracy and yield classes that were more complex than the six example classes was not tested. Real-world optical data often include noisy auroral images, such as those with clouds, moonlight, and sunlight contamination. Any ambiguity in the definition of the auroral image hampers the automatic detection and the statistical analysis of the auroral occurrence. Therefore, it is important to distinguish the quality of the optical data, regardless of whether it is just an auroral image. A similar study using color all-sky images demonstrated that a DNN model called ResNet-50 (He et al., 2016) can classify the images into seven auroral classes with an average precision and F1 score of 92% and 90%, respectively (Kvammen et al., 2020). Here, precision and recall are the ratios of true positive (TP) to TP + false positive (FP) and that of TP to TP + false negative (FN), respectively. The F1 score is a harmonic mean of precision and recall. However, because the authors of this previous study did not train non-auroral images, such as those captured during cloudy conditions, it is still difficult to classify regularly captured color all-sky images and then perform a statistical analysis of the auroral occurrence rate. Thus, it is highly demanded to evaluate if machine-learning-based automated classification is sufficiently accurate for investigating the statistical characteristics of auroras, such as their seasonal and local time distribution. It is also needed to test the feasibility of operating a notification system for the auroral appearance in real-time.

In the current study, we automatically derived the yearly, monthly, and universal time (UT) variations of the auroral occurrence rate for the first time by classifying images captured over 10 years using digital cameras in Tromsø, Norway (69.6°N, 19.2°E). Refer to the following sections for details regarding the observation. We manually classified some of the observed images into eight classes, as shown in Figure 3.1, and then, the ResNet-50

model trained them. As described in a previous study (Clausen and Nickisch, 2018), we defined *Arc*, *Discrete*, and *Diffuse* as the classes of auroras that are not contaminated by moonlight or clouds and have a high quality. The *Arc* is a single or double stripe extending in the east-west direction, often observed before midnight as a precursor to auroral breakup (Karlsson et al., 2020). *Discrete* auroras are bright and curly auroras that can appear white or pink at the lower limit when they are particularly intense. The *Diffuse* aurora glows faintly and is mainly observed after midnight. The majority of *Diffuse* is a pulsating aurora (PsA) that shows quasi-periodic variations in its brightness, i.e., variations ranging from a few to several tens of seconds (Lessard, 2012; Nishimura et al., 2020). We also defined *Clear* as when no aurora was detected, even though any type of auroras was observable without the influence of moonlight or clouds. In the statistical analysis, these four classes were collectively referred to as the *Observable* classes, and only these classes were used to calculate the auroral occurrence rate. The definition of the auroral occurrence rate is the number of *Auroral* classes divided by the number of images of the *Observable* classes. To distinguish between the quality of the optical data, we defined *Noisy aurora* as the auroral images contaminated by moonlight or sunlight (*Aurora but bright*) and obscured by clouds (*Aurora but cloudy*). We have also added classes for the cloudy and dawn/dusk images. Although we can identify the *Dusk & Dawn* images by calculating the solar elevation angle, we prepared a specified class for them to simplify the overall workflow. A more detailed description of each class is given in the following section. In addition to the statistical analysis, we also introduce a real-time notification system for the auroral appearance using the classifier. If citizen scientists can use this system to catch the appearance of aurora quickly, they may be able to take more photographs with less effort. Therefore, this system will allow more citizen scientists to participate in research regarding space science more efficiently.

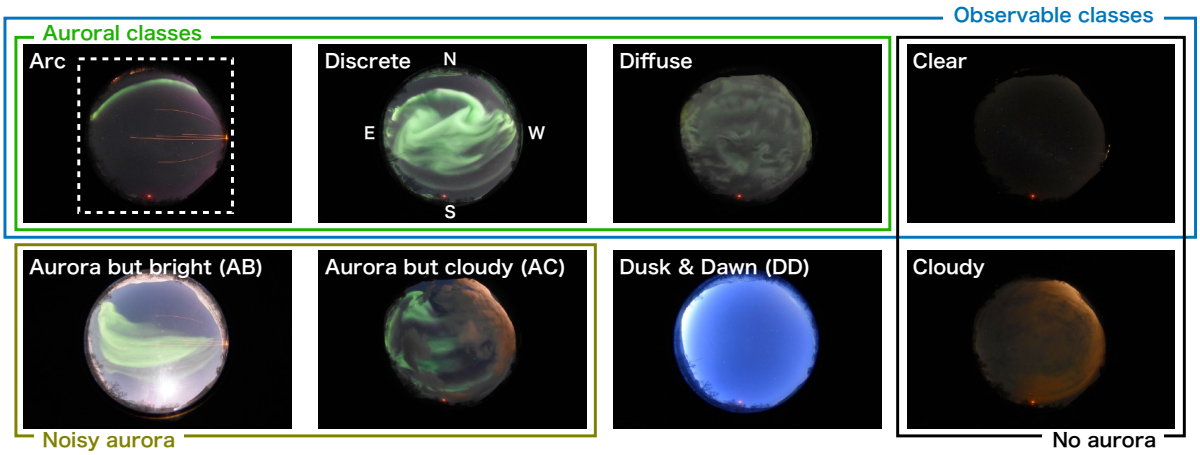

Figure 3.1: Sample images of the eight classes for the differentiation of all-sky images. The white dashed square in the image of the *Arc* class indicates the region used for training. For statistical analysis, we defined the auroral occurrence rate as the ratio of the *Auroral* classes (*Arc, Discrete, and Diffuse*) to the *Observable* classes (*Auroral* + *Clear*). *Noisy aurora* and *No aurora* classes are used in the bottom panel of Figure 3.3.

As already mentioned in the first paragraph of this section, the following sections describe the development of a deep learning model to automate observations with the Nikon D5. We also calculate the annual, seasonal, and local time dependence of the auroral occurrence rate with this model by classifying ten years of observation images obtained in Tromsø and then compare those with previous studies obtained by visual detection. The real-time classification by this model was used to implement a website, "Tromsø AI," that notifies users of the occurrence of auroras. Section 3.3 describes the observations made with the Nikon D5, which were the original motivation for developing the model. This includes an optical calibration experiment using a standard light source and a geometrical calibration using star positions. By using the results of the optical and geometrical calibrations, the observation results from the Nikon D5 are compared with those from the all-sky digital camera and photometer to evaluate the superiority of the Nikon D5 and the accuracy of the RGB values to Rayleigh values. This enables a discussion of how commercial digital cameras can be used for quantitative auroral research.

3.2 Automated detection of auroras in Tromsø, Norway

3.2.1 All-sky camera operated in Tromsø, Norway

Since 2011, Nikon digital cameras (D5000, D5100, and D7200) have been capturing all-sky images almost every night from September to March with a temporal resolution of less than one minute at Ramfjordmoen Research Station in Tromsø, Norway (69.6°N, 19.2°E); the station is operated by the UiT - the Arctic University of Norway. These images were not originally planned to be used for statistical analysis of the auroras, as they were obtained to evaluate weather conditions during the acquisition of atmospheric temperature/wind observations using a sodium LIDAR (Tsuda et al., 2013; Nozawa et al., 2014; Tsuda et al., 2015) and multi-wavelength observations of auroras using a photometer (Adachi et al., 2017; Nozawa et al., 2018; Kawamura et al., 2020). The digital cameras used were D5000 from 2010 to 2014, D5100 from 2015, and D7200 from 2016 to 2021. A Sigma 4.5mm f/2.8 EX DC HSM Circular Fisheye lens was used. The temporal resolution, exposure duration, and ISO sensitivity are 1 min, 15 sec, and 2500 during 2011–2013, and 30 sec, 8 sec, and 3200 during 2014–2021, respectively. Although the shooting settings varied yearly, the colors and shapes of the stars, clouds, and auroras in the JPEG images did not change significantly. The images taken by the digital camera are uploaded to the following URL: `https://www.isee.nagoya-u.ac.jp/~eiscat/obs/d5000/html/sky_image.html`. The original image size is 4496 × 3000 pixels, but the uploaded image has been downsampled to 722 × 480 pixels. In addition, the uploaded images are labeled with text giving the time and directions of the image. By classifying the uploaded images, we conducted a statistical analysis and developed a real-time notification system.

3.2.2 Setting of training and definition of image classes

The classification algorithm is based on the previous studies (Kvammen et al., 2020; Clausen and Nickisch, 2018), with minor modifications for noisy (i.e., contaminated auroral) images. One of our objectives is to detect an aurora in color all-sky images, including

cloudy ones. The previous study (Kvammen et al., 2020) showed that the ResNet-50 model classifies auroras into seven classes with high accuracy, but an image without auroras was not considered. Here, the ResNet-50 means a residual network having 50 layers. The ResNets have to skip connections between hidden layers, which makes it difficult to decrease accuracy even when the number of layers increases. The other study (Clausen and Nickisch, 2018) proposed a design of six classes that can classify actual auroral data correctly, although grayscale images were the target of the classification. Based on the results of these previous studies, we reconstructed the eight classes by renovating their definitions based on the latter study (Clausen and Nickisch, 2018) and classified images using the same model as the former study (Kvammen et al., 2020) (ResNet-50). To evaluate the auroral occurrence more accurately, we defined new classes of auroras with cloudy and moonlit conditions, which were not considered in the latter study (Clausen and Nickisch, 2018). The details of the definition of each class are described below. The percentage of the field of view occupied by clouds was estimated based on visual inspection. The threshold value for bright and dark was not determined using the solar elevation angle but by visually checking whether the darkness level was the same as at midnight on a new moon day. This brightness standard was applied not only to the effects of sunlight but also to those of moonlight. All images were downsampled to a resolution of 128 $\times$ 128 pixels as in the former study (Kvammen et al., 2020), as indicated by the white dashed square in the *Arc* panel in Figure 3.1, before being used for training. Other pre-processing was not performed.

After the pre-processing, we fine-tuned the pre-trained weights on the ImageNet dataset (Deng et al., 2009) using the training data. The batch size and epoch were 128 and 4, respectively. The stochastic gradient descent (SGD) was used as the optimizer, and the learning rate and momentum were given arguments of 0.001 and 0.9, respectively. The training program was written using Keras (Chollet et al., 2015).

The classes used for the classification are defined as follows:

Arc

Images with one or two auroral arcs extending in an east-west direction, a dark background, and less than 20% of the field of view occupied by clouds. These auroras often appear prior to the onset of substorms.

Discrete

Images with non-*Arc* discrete auroras, a dark background, and less than 20% of the field of view occupied by clouds. These are intense auroras that often appear with the auroral breakup.

Diffuse

Images with diffuse auroras (including pulsating auroras), a dark background, and less than 20% of the field of view occupied by clouds.

Aurora but cloudy (AC)

Images with auroras, a dark background, and more than 20% of the field of view occupied by clouds.

Aurora but bright (AB)

Images with auroras and a bright background, regardless of the cloud cover.

Clear

Images with no aurora, a dark background, and less than 20% of the field of view occupied by clouds.

Cloudy

Images with no aurora, a dark background, and more than 20% of the field of view occupied by clouds.

Dusk & Dawn (DD)

Images with no aurora and a bright background, regardless of the cloud cover. This class includes not only images brightened by sunlight but also those illuminated by moonlight.

The training and validation datasets manually labeled from the above definitions can be downloaded from the following URL: `https://tromsoe-ai.cei.uec.ac.jp/~nanjo/public/dataset/`, which can be used by the readers to evaluate the performance of the classifier with auroral images taken at different places by using different cameras.

Despite the detailed classification, some images do not belong to any of the above classes. We did not use such images in the training because they do not contain the aurora and therefore would not affect the task of extracting aurora-containing images (*Auroral* classes + *Noisy aurora*) from a large number of the regularly captured images.

3.2.3 Training and evaluation of the model

A total of 5,530,796 images were captured in Tromsø from the 2011 to 2021 season, of which 87,275 (1.6% of the data) were manually labeled and then used for the training and evaluation of the ResNet-50 model. The images were also manually divided into two categories, i.e., training and validation, for each class, as shown in Table 3.1. Because the inclusion of similar images in both categories leads to an unreasonably high accuracy, we ensured that no images observed on the same day were included in both categories. Figure 3.2 shows the confusion matrix that exhibits the classification results of the trained ResNet-50 model against the validation data. All the validation images were allocated to a class with the largest probability. The values in each panel show the classification rate for each class. For example, the top-left cell shows that out of 315 *Arc* images in the validation data, 96.2% were correctly classified as *Arc* by the trained classifier. The panels where the true label and predicted label coincide, which are correctly classified cases, are all reddish, indicating that the classification is highly accurate. The average precision and F1 score were 93.1% and 93.4%, respectively. Since one of the purposes of this study is to detect auroras automatically, it is particularly important to ascertain whether an image belongs to an *Auroral* class. To distinguish whether an image belongs to an *Auroral* class,

the precision and F1 score should be even higher, at 97.1% and 95.9%, respectively.

Label	Arc	Discrete	Diffuse	Clear	AB	AC	DD	Cloudy
Training	2352	3516	7114	7764	4309	2880	23599	20680
Validation	315	766	2133	1553	862	576	4720	4136

Table 3.1: Number of images per class used for training and validation of the model. Training and validation do not include images obtained on the same day.

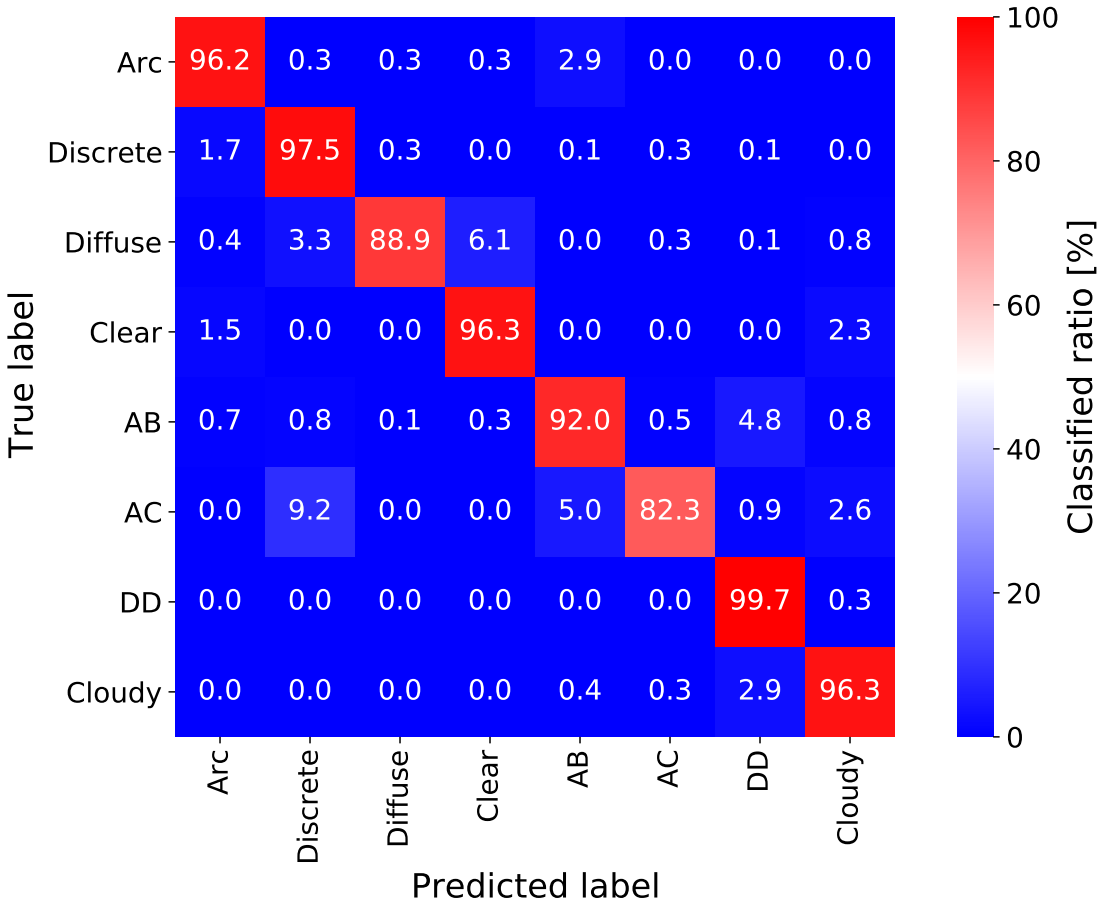

Figure 3.2: The classification result of the validation dataset by the trained ResNet-50 model. The top row shows that 96.2% of the 315 manually classified *Arc* images were correctly classified as *Arc*, while 2.9% were incorrectly classified as *Aurora but bright*. All the panels with matching true and predicted labels have high values of classified ratio, indicating high classifier accuracy.

Figure 3.3 shows the observation and classification results for images from a night that was not used for either training or validation. On this night, a typical substorm cycle, which comprised the *Arc*, *Discrete*, and *Diffuse* auroras (Akasofu, 1976), was observed twice. The format of Figure 3.3 follows that of a previous study about the automatic detection of auroras (Clausen and Nickisch, 2018). The top row shows the all-sky images at several representative times (T_0 to T_4), the second row is the time series of the north-south cross-section of the all-sky image (so-called keogram), and the third row shows the classification probability of each class. At T_0, which is shortly after sunset, the all-sky image and keogram are bluish. The classification result shows *Dusk & Dawn* with a 100% probability, which means the classifier works correctly. From 17:00 UT, the sky darkened completely, as shown in the all-sky image at T_1. The classification result for this period was *No aurora*, which is also correct because this label is a combination of *Clear* and *Cloudy*, as already shown in Figure 3.1. The green aurora appeared in the keogram from ∼19:30 UT and the classifier recognized it as *Arc* and *Discrete*. At T_2, a typical east-west arc was observed in the all-sky image, and the classifier detected *Arc* with a probability of 100%. At T_3, an auroral breakup occurred, with an active discrete aurora covering most areas of the sky. The classifier detected *Discrete* correctly. After that, the *Diffuse* aurora was detected until 23:00 UT and a dimmer diffuse aurora was also visible in the keogram and the all-sky image at T_4. The classifier detected the aurora almost successfully through the entire episode of the auroral substorm from 19:30 until 23:00 UT. Another substorm after midnight was also detected without any significant problems.

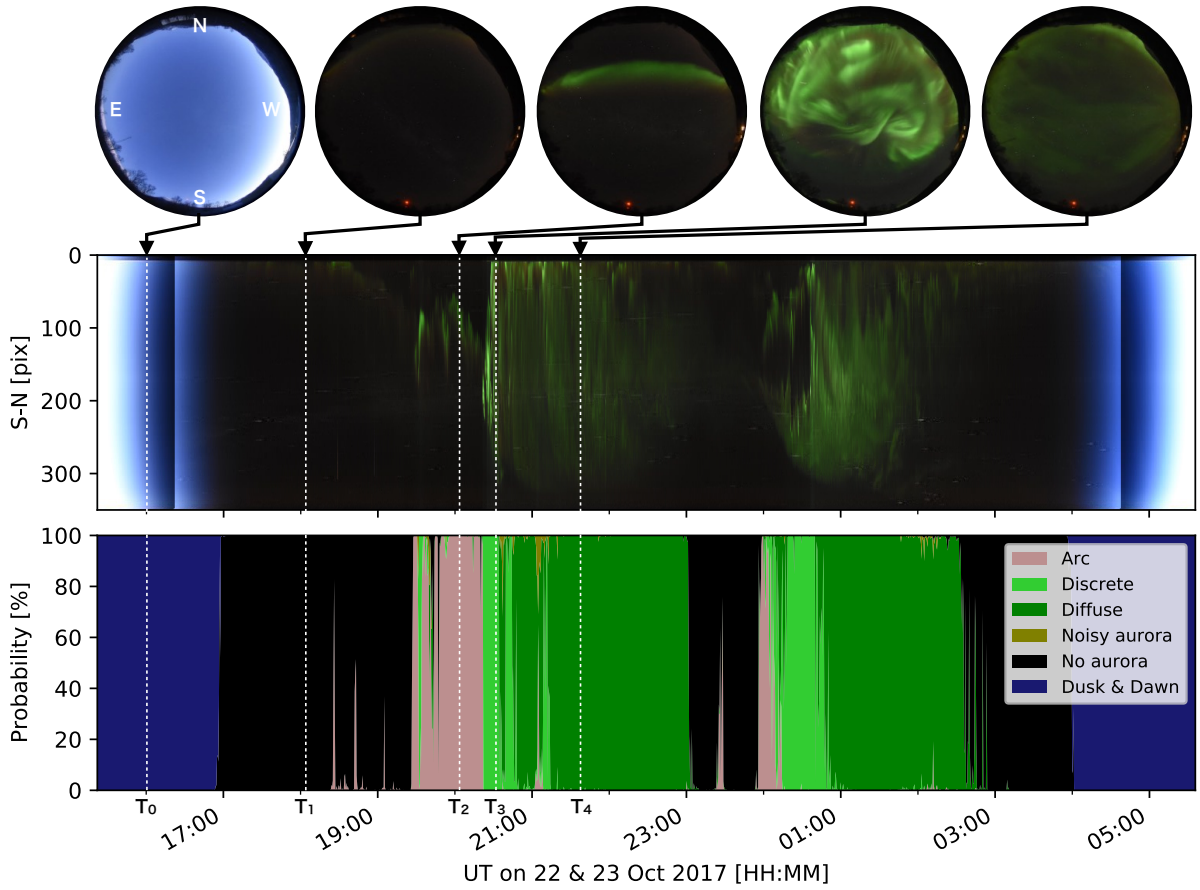

Figure 3.3: Observation and classification results on the night of 22–23 October 2017. The middle panel shows a keogram, a time series of the north-south cross-section of the all-sky image, and the bottom panel is the classification result for the same period. All-sky images at specific times (T_0 to T_4) are displayed on the top. T_0 to T_4 are 16:00:01, 18:00:05, 20:04:39, 20:30:40, and 21:30:11 UT, respectively. From 19:30 to 23:00 UT, the typical substorm signature, characterized by a sequential appearance of *Arc*, *Discrete*, and *Diffuse*, was classified almost perfectly. A similar substorm occurred again from midnight and was also classified correctly.

Interestingly, at 18:30 and 23:30 UT, the classifier detected *Arc* with a probability of ∼60%, and the faint aurora was visible near the northern limit (upper part) of the all-sky image at these times. These arcs appeared in a much smaller area than the typical aurora seen during substorms; thus, the classifier may not respond with a high probability value. These very faint auroras could be noise in the statistical analysis because the classifier

sometimes responded and sometimes did not. Based on this, we defined the auroral appearance as when the sum of the probabilities of the *Auroral* classes exceeded 80%. This threshold value was used for the statistical analysis presented in the next section. Although all detections were performed automatically, we eventually created images in the same format as that shown in Figure 3.3 for all observation dates over 10 years and visually confirmed that the classification results were correct to the same level as that demonstrated in Figure 3.3.

3.2.4 Statistical analysis of the auroral occurrence

Figure 3.4 shows the distribution of the auroral occurrence rate as a function of month and year over 10 years. The vertical axis is the month, and the horizontal axis is the year of the optical season, i.e., from September to March of the next year. Again, the auroral occurrence rate is defined as the number of the *Auroral* images divided by that of the *Observable* images. Each square panel filled with colors indicates the occurrence rate, the number of the *Auroral* images, and that of the *Observable* images. While the number of images varies widely from month to month, as it is affected by the length of cloudy periods and the temporal resolution, the occurrence rate is less affected by these factors. In September 2014 and 2018, when the numbers were unavailable, the camera was not operative due to the delay in starting the observation. The panel is mostly bluish throughout the decade from November to January, indicating a lower auroral occurrence rate. To make it easier to observe this tendency, we have added the right panel, which shows the monthly variation of the occurrence rate derived by summing the numbers over the decade. The panel clearly demonstrates the decreasing trend of auroral occurrence in the winter solstice. Furthermore, it was found that there was no significant difference between the auroral occurrence rate in the autumn and spring equinoxes, i.e., the graph was nearly line-symmetrical with respect to December. The same method was applied to plot the upper panel, which shows the annual variation of the auroral occurrence rate. There was no peak in the 2013 season when the sunspot number reached its maximum during solar cycle 24. Instead, the 2015 season, which corresponds to the early declining phase of the solar cycle, has a peak in the occurrence rate. The auroral occurrence rate attained its minimum during the 2019 season when the sunspot number reached its

minimum.

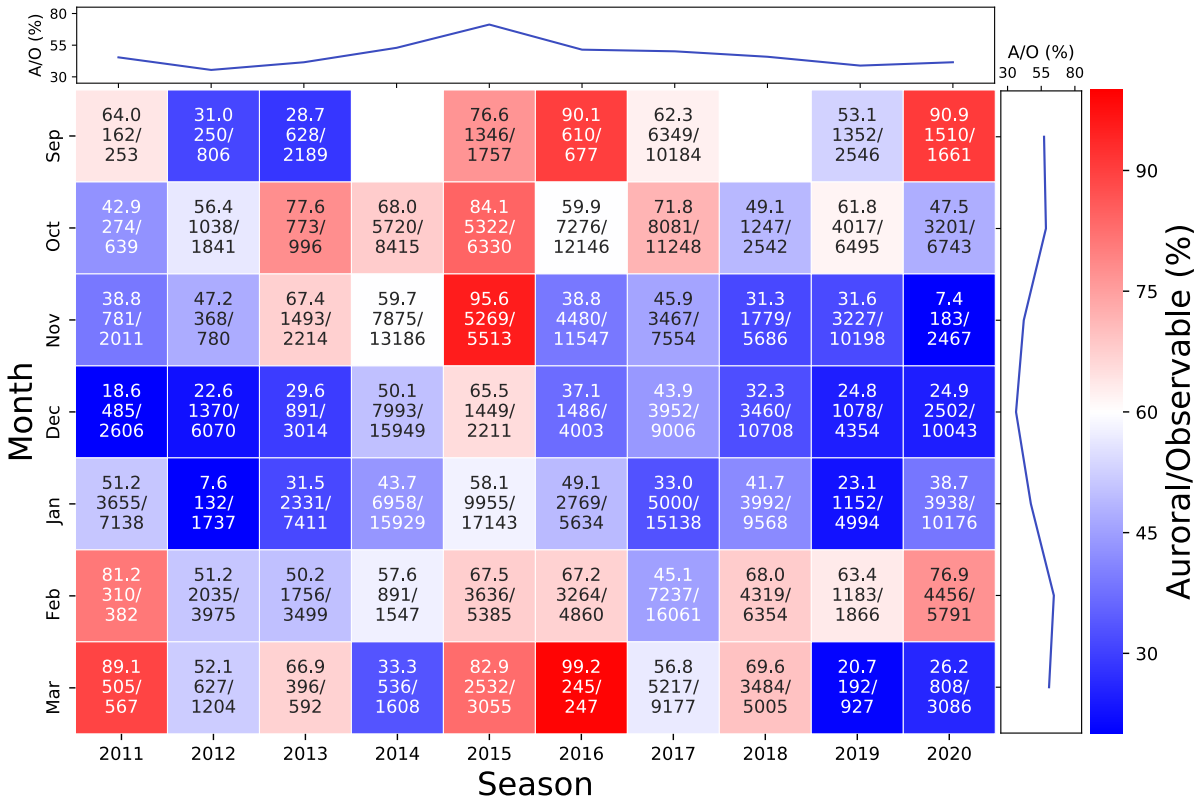

Figure 3.4: Monthly occurrence rate of the aurora from 2011 to 2020. Each panel shows, from top to bottom, the occurrence rate, number of *Auroral* classes, and number of *Observable* classes. The red panels indicate a high occurrence rate, and the blue panels indicate a low occurrence rate. The blue line in the upper panel shows the annual variation in the occurrence rate obtained by data integration. Similarly, the blue line in the right panel shows monthly variation in the occurrence rate. The occurrence rate was the highest in the 2015 season and tended to be higher in fall and spring than in winter.

Since all the images used in this study were captured in Tromsø, it is likely that local parameters representing the level of geomagnetic disturbances, such as the K-index (Bartels, 1949), rather than macroscopic/global parameters, such as the sunspot number, would correlate well with the auroral occurrence rate. The K-index represents the geomagnetic disturbance on a 10-point scale (0–9) with a three-hour temporal resolution; the higher the K-index, the more likely it is for an aurora to appear. Figure 3.5 shows the annual variation of the auroral occurrence rate shown in Figure 3.4 and the ratio of

time when the K-index was above 4 during a local night in Tromsø, i.e., 15–03 UT. Note that only days with more than 100 *Observable* images were included in the calculation. The blue and red lines met their minimums in the 2012 and 2019 seasons. A maximum existed in the 2015 season, indicating that the level of local geomagnetic disturbance and automatically derived auroral occurrence rate are positively correlated over a long period of 10 years.

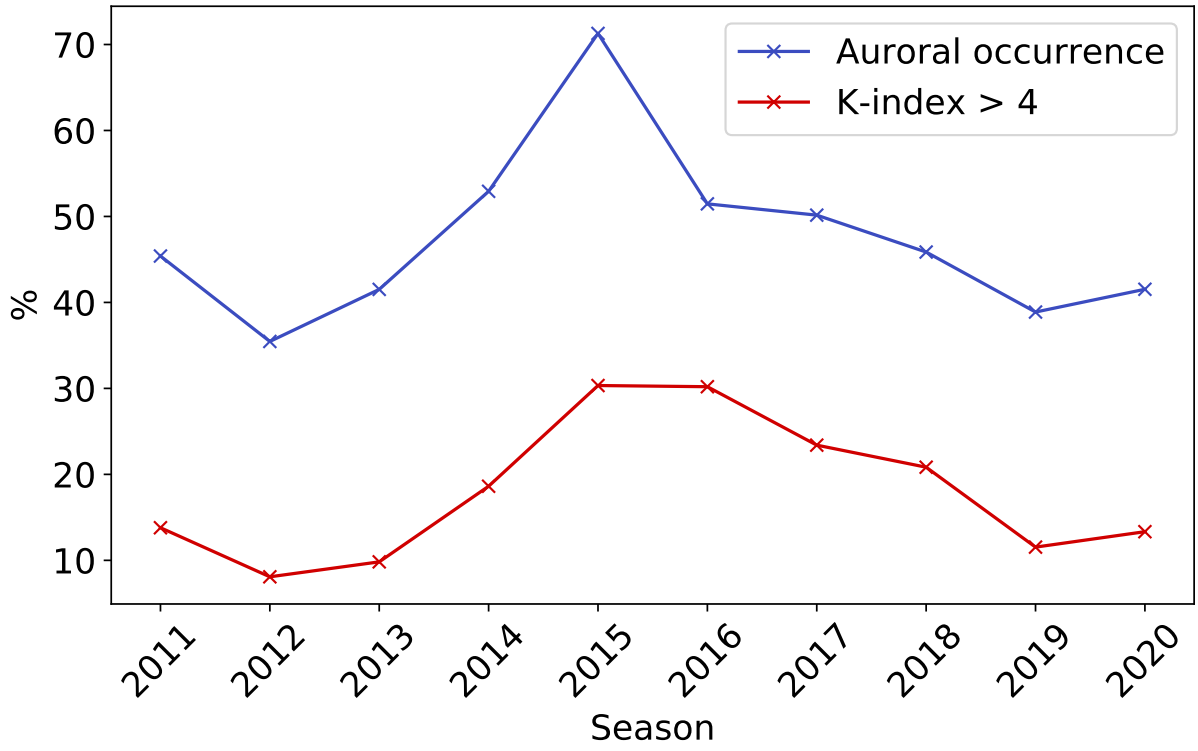

Figure 3.5: The blue line shows annual variation in the occurrence rate of aurora. The red line shows the percentage of times when the K-index was 4 or higher during clear nights in Tromsø. Years with higher K-index have higher occurrence rates.

Figure 3.6 shows the monthly variation of the auroral occurrence rate shown in Figure 3.4. The blue line covers all UT, while the red line covers only 19–02 UT, i.e., when the sky is completely dark from September to March. The occurrence rate of the red line, which is for limited UT periods, is higher than that in the blue line, suggesting that the auroral occurrence rate is lower in the early and later UT. In both lines, the auroral occurrence rate attains its maximum in October and February and a minimum in December. This

means that regardless of the length of the dark hours, the occurrence of auroras is higher in autumn and spring and lower in winter. Especially, the blue line shows a nearly two-fold difference between the auroral occurrence rates in October and December. It has been pointed out since the beginning of the 20th century that the frequency of magnetic storms is higher near the spring and autumnal equinoxes and lower around the summer and winter solstices (Cortie, 1912). This effect may be due to the Russell–McPherron (R–M) effect (Russell and McPherron, 1973), in which the z component of IMF in the GSM coordinate system has a systematic shift to negative (i.e., southward IMF) during equinoxes due to the seasonal change of the tilt of the Earth's dipole axis. The monthly variation of the auroral occurrence rate is qualitatively consistent with the characteristics of the R–M effect.

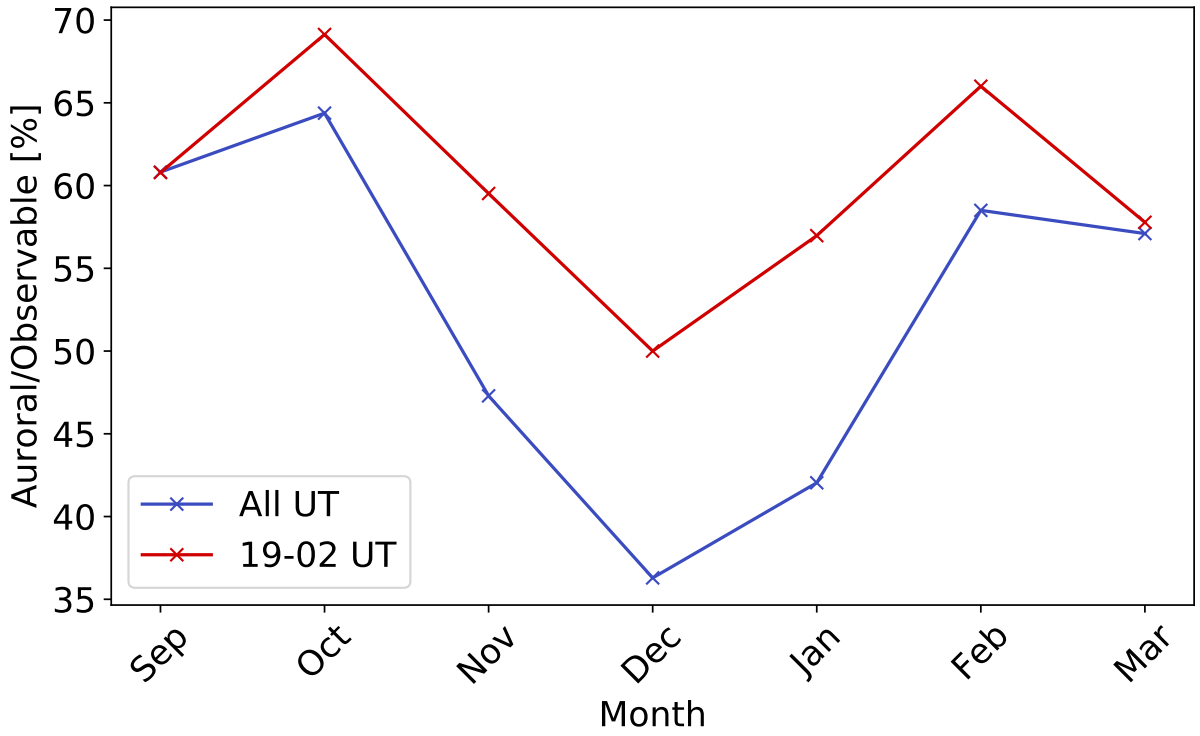

Figure 3.6: Monthly variation in the occurrence rate of aurora for all UT (blue line) and 19 to 02 UT only (red line). During 19 to 02 UT, the sky is completely dark in all the months from September to March in Tromsø. For both lines, the occurrence rate is the lowest in December, which includes the winter solstice, and it is higher near the spring and autumn equinoxes.

Figure 3.7 shows the UT distribution of the *Observable* classes obtained over 10 years. Panel (a) shows the number of images, panel (b) shows the composition ratio of panel (a) for each UT bin, and panels (c) to (e) show the values of panel (b) for each *Auroral* class. In panel (a), while more than 25,000 images were stably classified as *Observable* in 19–02 UT, the number of the images increased/decreased in 15–18/03–06 UT, respectively. This is due to the monthly change in the length of the dark time. To reduce this effect, the composition ratio of each class in each UT bin is shown in panel (b). The lower ratio of the *Auroral* classes to the *Clear* class in the early and late UT was consistent with the suggestion from Figure 3.6 that auroras occur less frequently in these UT periods. The ratio of the *Auroral* classes reached its maximum at 22 UT, which roughly corresponds to 01 MLT. This result is consistent with the results of previous studies obtained by visual detection (Sheret, 1963; Blackie, 1964; Blundell, 1967). Panel (b) shows that discrete auroras dominate in the evening and diffuse auroras dominate from the magnetic midnight (00 MLT $\sim$ 21 UT) to the morning. The comparison between panels (c) and (d) shows that the ratio of *Arc* is higher than that of *Discrete* in 15–18 UT, which may be due to the tendency that intense discrete auroras occur after the appearance of an arc-type aurora (Karlsson et al., 2020), as seen in Figure 3.3. The *Discrete* auroras had a wide plateau at 18–21 UT ($\sim$21–00 MLT). By contrast, the ratio of *Diffuse* auroras gradually increased from the evening hours, peaked at 01 UT ($\sim$ 04 MLT), and then decreased towards dawn. This trend is consistent with other statistical analyses performed visually and using automated detection techniques (Syrjäsuo and Donovan, 2004; Partamies et al., 2017; Nevanlinna and Pulkkinen, 2001).

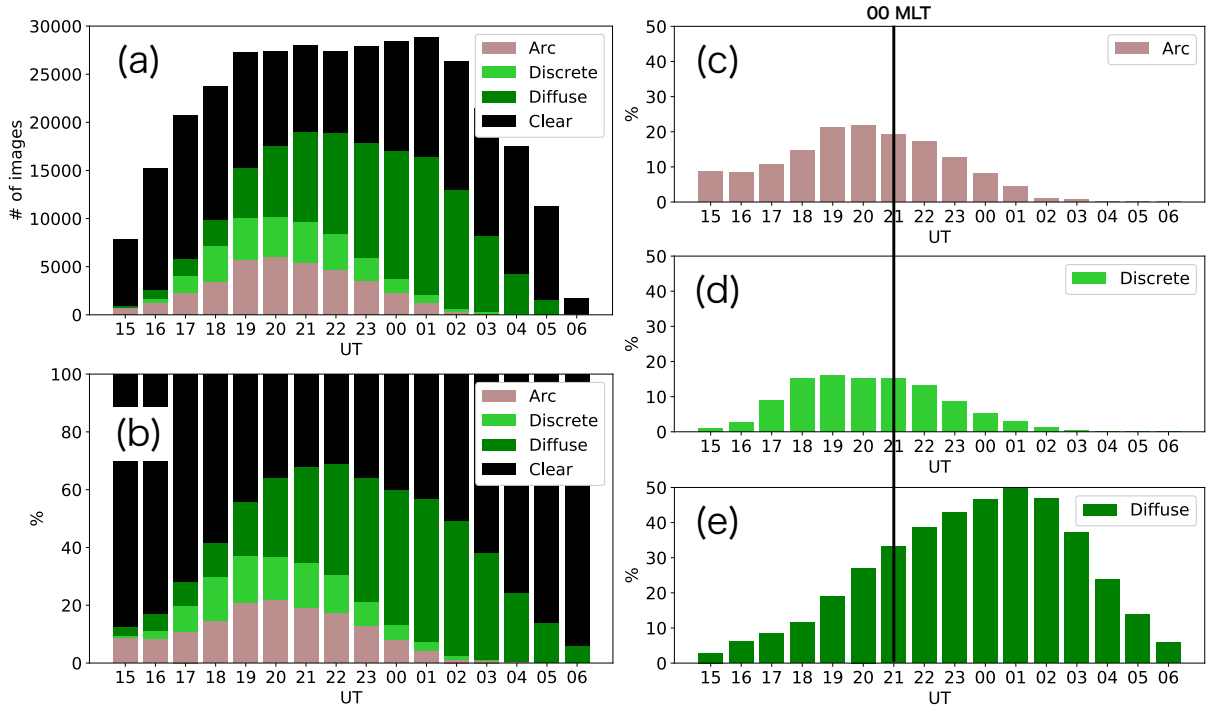

Figure 3.7: (a) Histogram showing the composition of images of *Observable* classes obtained over 10 years. A decrease in the number of images in 15–18 UT and 03–06 UT is due to the difference in the length of the dark time. (b) The composition ratio of the number of images in the *Observable* classes. The occurrence rate of the aurora was maximized at 22 UT (01 MLT). (c)–(e) Composition ratios of panel (b) for each *Auroral* class. The occurrence rate of discrete auroras (*Arc* and *Discrete*) peaked before 00 MLT and was almost zero after 01 UT (04 MLT). *Diffuse* was most likely to occur at 01 UT (04 MLT), and the occurrence rate was widely distributed across other UTs.

Figure 3.5 shows the positive correlation of the auroral occurrence rate with the ratio of the highest K-index time. Both reached their maximum in the 2015 season, an early declining phase of solar activity. The Kp-index, which is a global version of the local K-indices (Bartels, 1949), increases during the phases of declining solar activity (Rangarajan and Iyemori, 1997), and our results demonstrate that the occurrence of auroras also increases in the early declining phase of the solar cycle. During this early declining phase, the auroral occurrence rate exceeded 70%. In contrast, before the solar maximum and during the solar minimum (the 2019 season), it was ∼35%, i.e., half the occurrence rate at the peak. Figure 3.6 shows that the auroral occurrence rate tends to be higher in

spring and autumn and lower in winter. Compared to the lowest auroral occurrence rate in December, the highest value in October was 65%, showing nearly a two-fold difference. This is most likely due to the R–M effect (Russell and McPherron, 1973), which explains why geomagnetic storms are more frequent in the spring and autumn equinoxes and less frequent in the winter and summer solstices. This tendency has already been reported in previous studies (Nevanlinna, 1995; Silverman, 1992), but because these previous studies have classified the images by the human eye, not all the images were classified by a stable/unique standard. In this study, since the classification is performed using a computer, the images taken over 10 years can be classified by the same standard in a short calculation time.

Panels (c) to (e) in Figure 3.7 show the occurrence rate of auroras from each *Auroral* class as a function of UT. For discrete auroras, which consists of *Arc* and *Discrete* auroras, the occurrence rate peaked in the pre-midnight sector and decreased sharply in the morning sector, as shown in previous studies (Gillies et al., 2014; Syrjäsuo and Donovan, 2004). A slightly larger composition ratio of the *Arc* auroras compared with that of the *Discrete* auroras may reflect the fact that arc-type auroras are the main element of auroras that tend to appear under all geomagnetic conditions (Partamies et al., 2015). The occurrence rate of *Diffuse* peaked in the morning sector, which is also consistent with previous studies (Jones et al., 2011; Syrjäsuo and Donovan, 2004; Partamies et al., 2017; Bland et al., 2019; Nishimura et al., 2020). Diffuse auroras could originate from magnetospheric waves, such as whistler-mode chorus (Nishimura et al., 2010; Jaynes et al., 2013; Kasahara et al., 2018a; Hosokawa et al., 2020) and electrostatic electron cyclotron harmonic (ECH) waves (Fukizawa et al., 2018, 2020), the former often being widely distributed from the midnight to noon sector (Li et al., 2009) and the latter from the pre-midnight to morning sector (Ni et al., 2011). In panel (e), the occurrence rate of diffuse auroras decreased in the morning sector owing to the effect of sunlight, but their occurrence over a wide range of UT was generally consistent with the distribution of the magnetospheric waves. These results indicate that a large number of the images taken in the last decade were classified successfully. The dependences of the occurrence rate obtained in this study will be useful not only for data analysis but also for a wide range of applications, from planning campaign observations to personal travel.

3.2.5 A notification service for auroral activity: Tromsø AI

The results of the previous section have quantitatively revealed the annual, monthly, and UT variations of the auroral occurrence in Tromsø. However, such overall statistical characteristics cannot be used to detect the auroral appearance at specific moments in the future. To overcome this limitation, we developed "Tromsø AI" (`https://tromsoe-ai.cei.uec.ac.jp/`), a web application that allows AI to monitor the auroral activity in Tromsø in real-time, instead of the human eye. Panel (a) in Figure 3.8 shows the top page of the website at 01:08:03 UT on 19th January 2021. The all-sky image in the "Latest View" shows a dynamic discrete aurora, and its classification result, listed in the "Latest Status", indicates that the image belongs to the *Discrete* class with 99% probability. This page has a desktop notification feature of the auroral appearance, which sends a notification card shown in the upper right if an image belongs to the checked classes in the box at the top of the page (i.e. if the sum of the probabilities of the checked classes exceeds 80%). Note that a desktop notification must be allowed in both the OS and the browser to use this function. The bottom of the page provides an ongoing keogram in the same format as that in Figure 3.3, showing the auroral activity up to that time of the night. In addition, a user can browse all observation results for the last ten years by clicking on the "Archive" link at the bottom of the title. Panel (b) in Figure 3.8 shows the page for the archived data. Users can select a season from the pull-down tab to view the calendar for the corresponding period (from September to April). Clicking on a date in the calendar will display the keogram and movie for that night. Each date in the calendar has a fraction, the numerator of which is the number of images classified as *Auroral* classes, and the denominator is the total number of images obtained that night. Days with many *Auroral* images are shown in green color on the calendar.

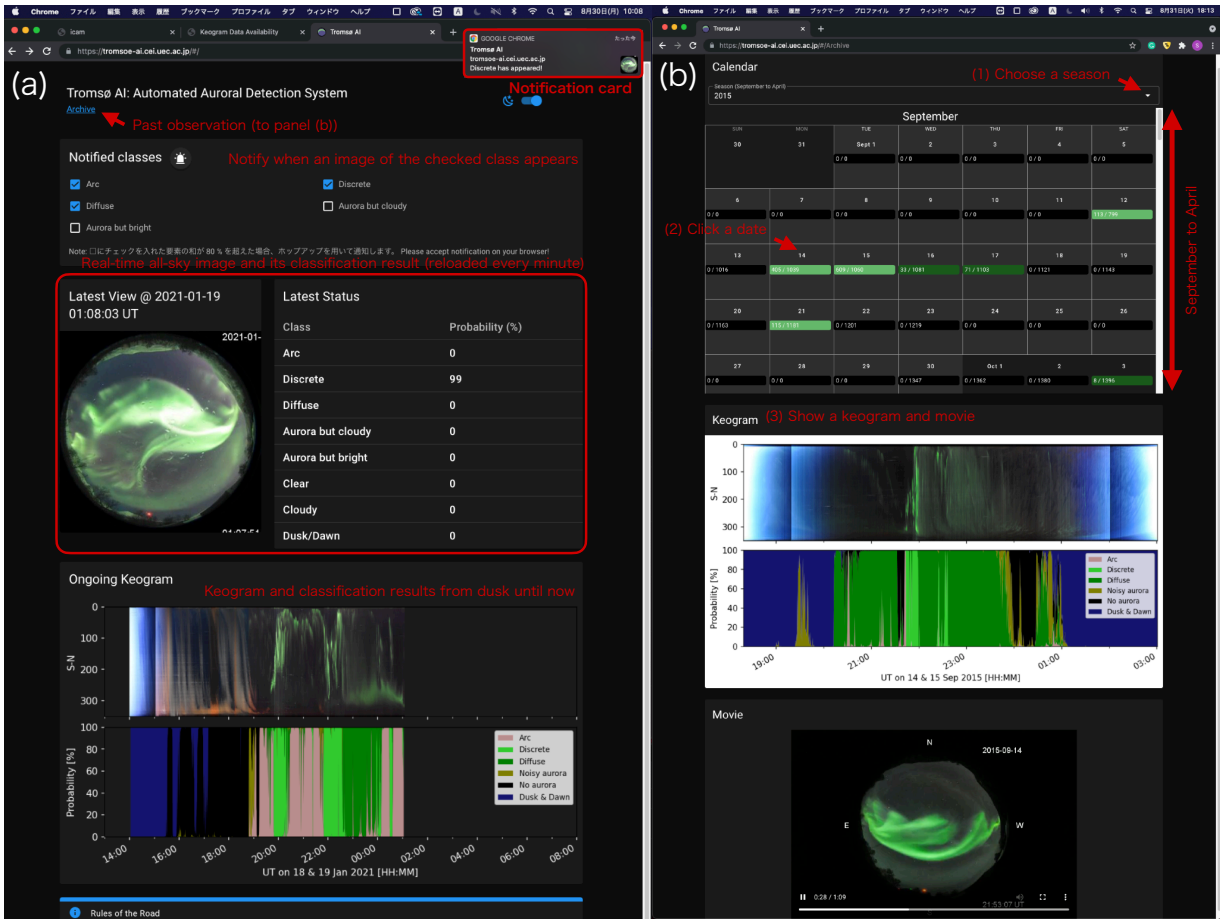

Figure 3.8: (a) Top page of Tromsø AI. The all-sky image and the classification result are displayed in real-time in the central part. In the lower part, the ongoing keogram from the sunset is displayed in the same format as Figure 3.3. A desktop notification appears in the upper right when an image of the classes checked in "Notified Classes" is displayed. By clicking "Archive" below the page, the user can view the archive page shown in panel (b). (b) Users can view a keogram and all-sky movie on any day by selecting a season from the drop-down menu and clicking on a date in the displayed calendar.

The website shown in Figure 3.8 was created to promote citizen science and to provide easy access to past observation data. This website provides instant updates on the appearance of auroras in Tromsø. Furthermore, if this system is installed at multiple observatories, the broader distribution of auroras can be obtained in real-time. Moreover, unlike professional optical instruments, digital cameras can obtain color information. As suggested in Chapter 2, the energy of precipitating electrons can be estimated qualita-

tively based on the color of a digital image, which can help enhance the contribution of citizen scientists to professional space science. The current aurora notification system can help citizen scientists know when the aurora appears and start their observation promptly. If they can capture more optical data with less effort by using the system, the threshold for participating in auroral science would become lower. Therefore, the system introduced here is a promising approach to reveal new features of auroras and improve our understanding of the processes underlying these phenomena.

3.3 Automated observations in Tromsø, Norway

In Chapter 2, we have shown that the B/G ratio of auroras observed from the ISS using the Nikon D5 might be qualitatively correlated with the average energy of the auroral electrons. For quantitative evaluation, we installed the Nikon D5 at the same observatory as the EISCAT radar, which can estimate the average energy of the electrons, and took photographs of auroras. In order to prevent damage to the shutter unit, we used Tromsø AI to make observations only when the aurora appeared. Specifically, when the probability of auroral appearance exceeded 80% according to the model, 1,200 images were taken with a time resolution of 0.5 seconds. Thus, the duration of each observation is about 10 minutes. The exposure time was 0.25 seconds, and the ISO sensitivity was 20000. We will introduce the calibration experiment necessary for the observation and the results obtained from the actual observation below.

3.3.1 Optical calibration

To confirm whether the count values recorded by the Nikon D5 are linear to the incoming light intensity, we conducted optical calibration with an integrating sphere at the National Institute of Polar Research (NIPR) (Ogawa et al., 2020a). We changed the spectrum of the light source inside the integrating sphere in four steps, as shown in the left panel of Figure 3.9. The Nikon D5 was placed inside the integrating sphere to examine the response in count values by changing light intensity. As shown in the legend in the right panel of Figure 3.9, the exposure time and ISO sensitivity settings were varied in five different measurement sets. Although there are three count values for the RGB channels,

only the most sensitive green counts were plotted. The counts due to dark current noise were also measured with the lens covered. The results of the above measurements are shown in the right panel of Figure 3.9. The count values increased linearly with the light intensity inside the integrating sphere for all five settings. It was also confirmed that in pairs where the product of ISO sensitivity and exposure time is equal, for example, when the exposure time is 0.25 s and ISO 20000 and when the exposure time is 0.50 s and ISO 10000, the mean value of the counts is equal within a standard deviation.

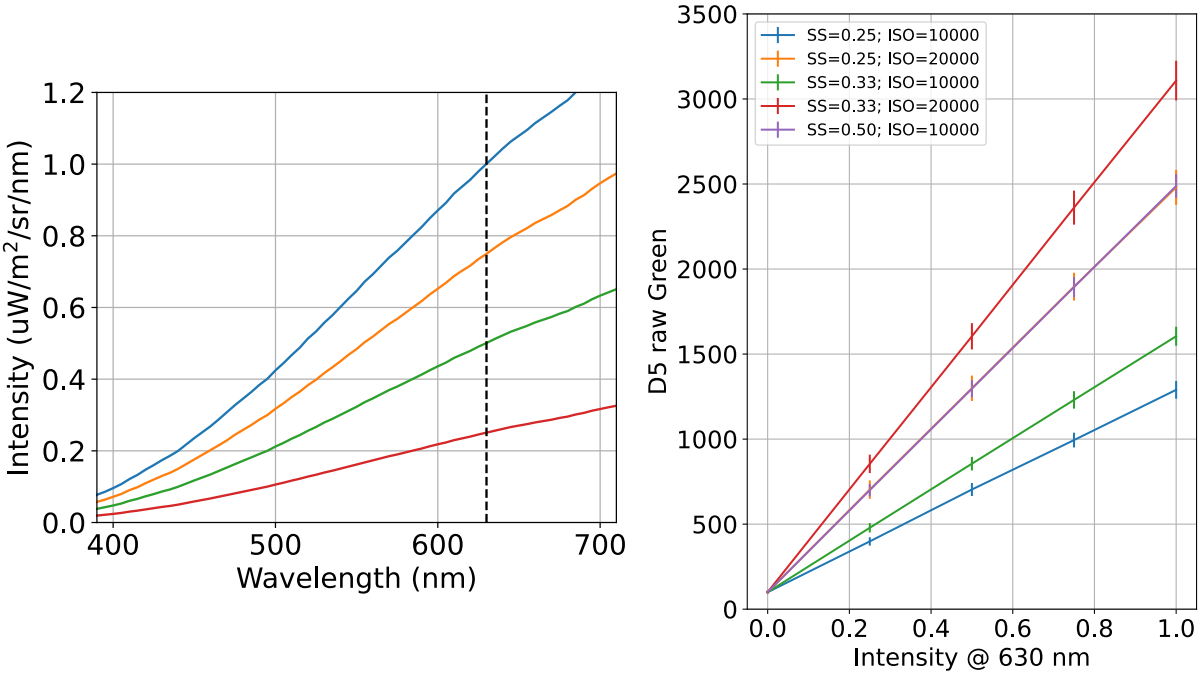

Figure 3.9: (Left) The spectrum of the light inside the integrating sphere. (Right) The count values in the Green channel of Nikon D5. Five settings in the legend were examined. SS stands for the shutter speed. The horizontal axis indicates light intensity at 630.0 nm inside the integrating sphere. The error bars are the standard deviation values of the center pixel among 1000 images.

To evaluate the variability of the count values, 1,000 images were taken at an exposure time of 0.25 s and ISO 20000, the settings used in the actual observations in Tromsø. The brightness in the integrating sphere was 0.75 at 630 nm (corresponding to the yellow spectrum on the right panel of Figure 3.9). The standard deviation of count values obtained from 1,000 images at a single point was calculated for the RGB channels separately, and

this process was repeated for all pixels to obtain the scatter plots in Figure 3.10. In addition, the scatter distributions were approximated by a quadratic polynomial.

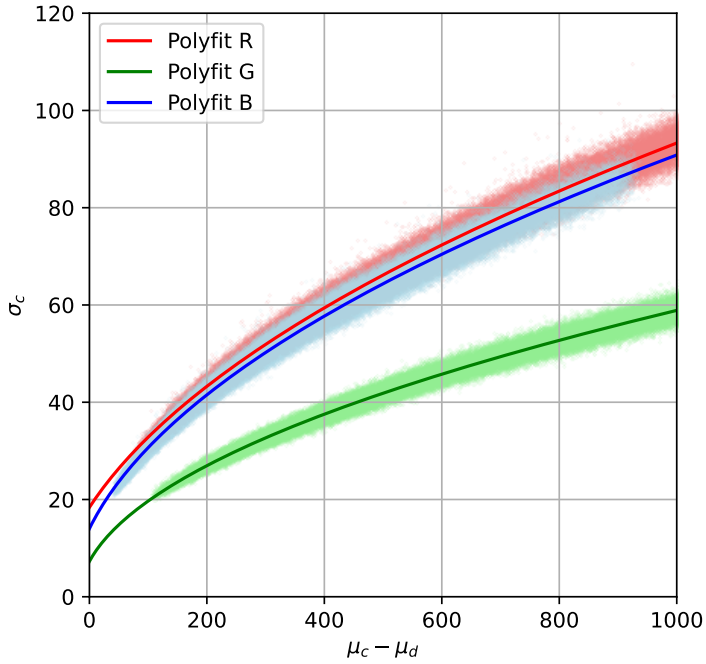

Figure 3.10: Evaluation of the signal-to-noise ratio of the count values by Nikon D5. The horizontal axis represents values subtracted by the dark count from the original count values. The vertical axis represents the standard deviation at each pixel among 1000 images.

To derive the transmission characteristics of the color filter of the Nikon D5, another experiment was conducted using a monochromator at NIPR (Ogawa et al., 2020a). As shown in the left panel of Figure 3.11, the wavelength of the light source was changed from 400 nm to 700 nm with 10 nm steps, and the Nikon D5 captured the light to examine the RGB value response. The exposure time was 0.25 s, and two ISO sensitivities, 8000 and 20000, were tested. The results are shown in the right panel of Figure 3.11. It was confirmed that multiplying the count value with an ISO sensitivity of 8000 by 2.5 yields the count value with an ISO sensitivity of 20000. In addition to the transmission characteristics, black lines are drawn at 427.8 nm, 557.7 nm, and 630.0 nm, the bright lines among the auroral spectrum. From this panel, we can confirm that the band emission of the nitrogen molecule, represented by 427.8 nm, roughly corresponds to the B channel and

the green line to the G channel, but the B channel is also slightly sensitive to the green line at 557.7 nm. The difference in count values is about 15-fold, but the contribution of the green line cannot be ignored because the green emission can be much stronger. On the other hand, although the green channel is also sensitive to the nitrogen band emission, the contamination would be negligible because 557.7 nm is usually brighter than the band emission of nitrogen molecules.

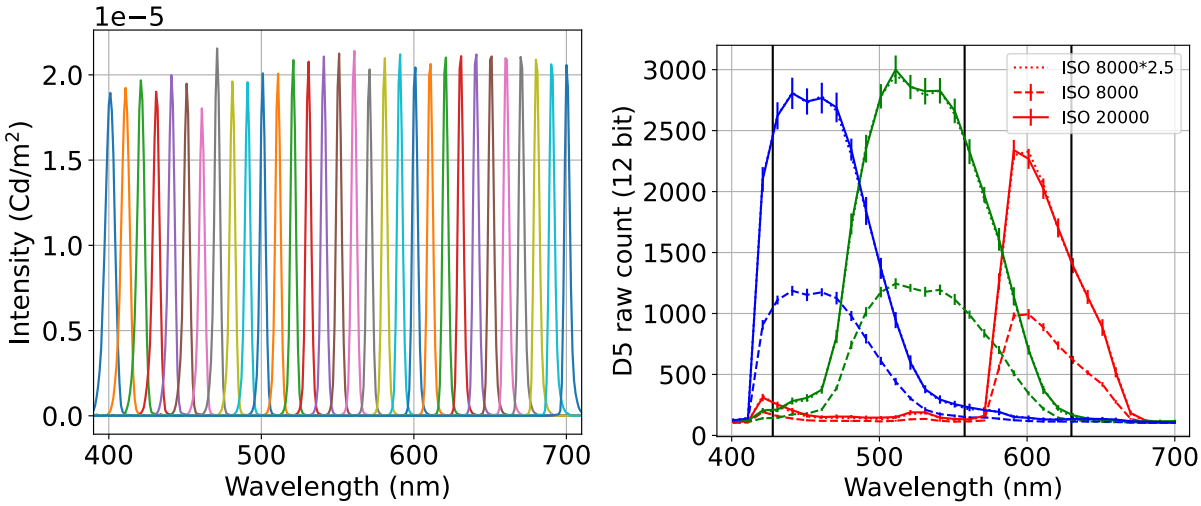

Figure 3.11: (Left) The spectra of the light source from the monochrometer. The measurements were conducted with 31 individual spectra. (Right) The transmission characteristics of the color filter of Nikon D5 were measured through the experiment with the monochrometer.

3.3.2 Geometrical calibration

After the optical calibration experiments, the Nikon D5 was installed on 7 September 2022 at the Ramfjordmoen field station near Tromsø, Norway. It was installed next to the all-sky digital camera used for Tromsø AI, as shown in Figure 3.12. This observation aims to compare the color of the aurora from the digital camera with the characteristics of auroral electrons derived from the EISCAT radar. Since the EISCAT UHF radar measures the altitude profile of the electron density at the magnetic zenith, the comparison requires a geometrical calibration of the image from Nikon D5. The geometrical calibration enables comparison not only with the EISCAT radar but also with the other ground-

based cameras and photometer. Although we conducted a special experiment for about 30 hours to observe auroras simultaneously with the EISCAT radar, the aurora did not appear during these hours; thus, we introduced only comparisons with the all-sky camera and the photometer.

Figure 3.12: The Nikon D5 (left) and the color all-sky digital camera used for Tromsø AI (right), both of which are operative at the Ramfjordmoen field station near Tromsø, Norway.

We used an open-source software called Astrometry.net (Lang et al., 2010) for the geometrical calibration. This software takes an image of the night sky with stars as input and outputs the camera's pointing, scale, and orientation of that image. The Python library astromtery_geomap takes the output from Astrometry.net, camera location, and imaging time as input and outputs the elevation and azimuth angles of each pixel of that image. By combining both software, the FoV calibration of the image from the Nikon D5 has been done, and the result is shown in Figure 3.13. The stars identified by Astrometry.net are circled, and the elevation and azimuth angles calculated by astrometry_geomap, as well as the latitude and longitude at 100 km altitude calculated from them, are drawn as the white contour lines. The cross mark in the lower center indicates the direction of the magnetic zenith, which is the pointing direction of the EISCAT radar and the photometer.

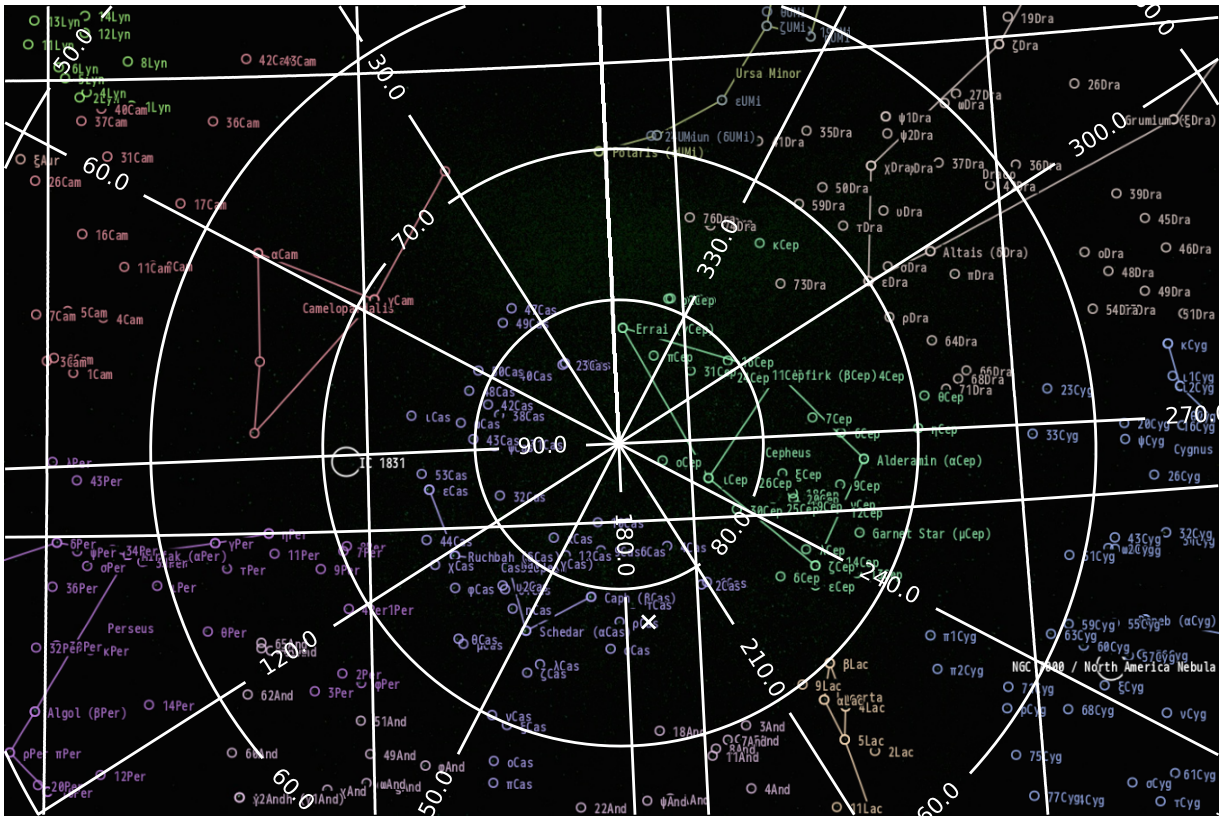

Figure 3.13: The sky image captured by the Nikon D5. The stars identified by Astrometry.net are circled, and the contour lines of azimuth, elevation angles, latitude, and longitude at the 100 km altitude are drawn. The cross mark represents the magnetic zenith, which is the direction of the measurements of the EISCAT radar and the photometer.

3.3.3 Comparison with the all-sky camera observation

Figure 3.14 compares the observation by the Nikon D5 and that by the all-sky digital camera. Panel (a) is a north-south keogram taken with the all-sky digital camera. There were two periods when the brightness of the aurora became particularly intense, starting at around 21:15 UT and 21:32 UT. The two white rectangles in the keogram indicate the observation interval and latitudinal coverage of the Nikon D5. Panel (b) is an all-sky image taken at 21:17 UT, where the poleward expansion was seen following an auroral breakup. The white rectangular area indicates the FoV of the Nikon D5. Panel (c) is a keogram taken by the Nikon D5. This panel corresponds to the first rectangle in panel (a),

and by comparing the two panels, we can see that the spatial and temporal resolutions of the observation have been improved by using the Nikon D5 with the narrow FOV lens. Panel (d) is an image from the Nikon D5 taken at around 21:17:17 UT, corresponding to when the all-sky camera took the panel (b). Comparing the two images, the morphology of the aurora is generally consistent, but pink emission can be seen in several locations in the Nikon D5 image. This emission might be a band emission by nitrogen molecules, which is replaced by a strong green emission after 0.7 s and thus should not be seen in the all-sky digital camera image taken with an 8-second exposure (panel b). Since the Nikon D5 observation has an exposure time of 0.25 s, it would be able to capture the band emission of nitrogen molecules.

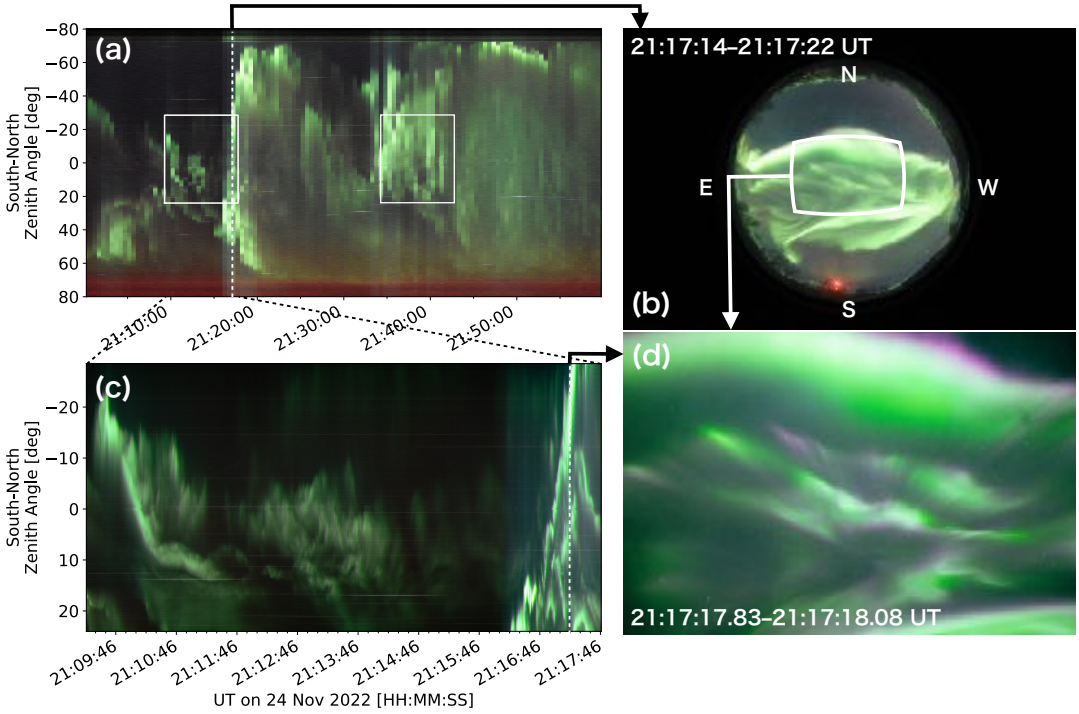

Figure 3.14: (a) The north–south keogram taken by the all-sky camera from 21 to 22 UT on 24 November 2022. The white rectangle regions correspond to the observation areas of the Nikon D5. (b) The all-sky image at the time is indicated by the white dashed line in panel (a). The exposure is from 21:17:14 to 21:17:22 UT. The white rectangle region corresponds to the FoV of Nikon D5. (c) The north–south keogram derived from the Nikon D5. (d) The image at the time is indicated by the white dashed line in panel (c). The exposure is from 21:17:17.83 to 21:17:18.08 UT.

3.3.4 Comparison with the photometer observation

The upper panel of Figure 3.15 shows the temporal variation of RGB values at the magnetic zenith obtained by the Nikon D5 in about 10 minutes from 16:19:17 UT on 2 November 2022. Each time series has error bars of the standard deviation obtained from the optical calibration experiment. The lower panel shows the time series of the absolute optical intensities in the unit of Rayleigh (the Rayleigh values) at 557.7 nm and 427.8 nm obtained by the photometer in the same interval. Comparing these time series, we can see that the Nikon D5 at least qualitatively reproduces the temporal variation in the auroral brightness obtained by the photometer.

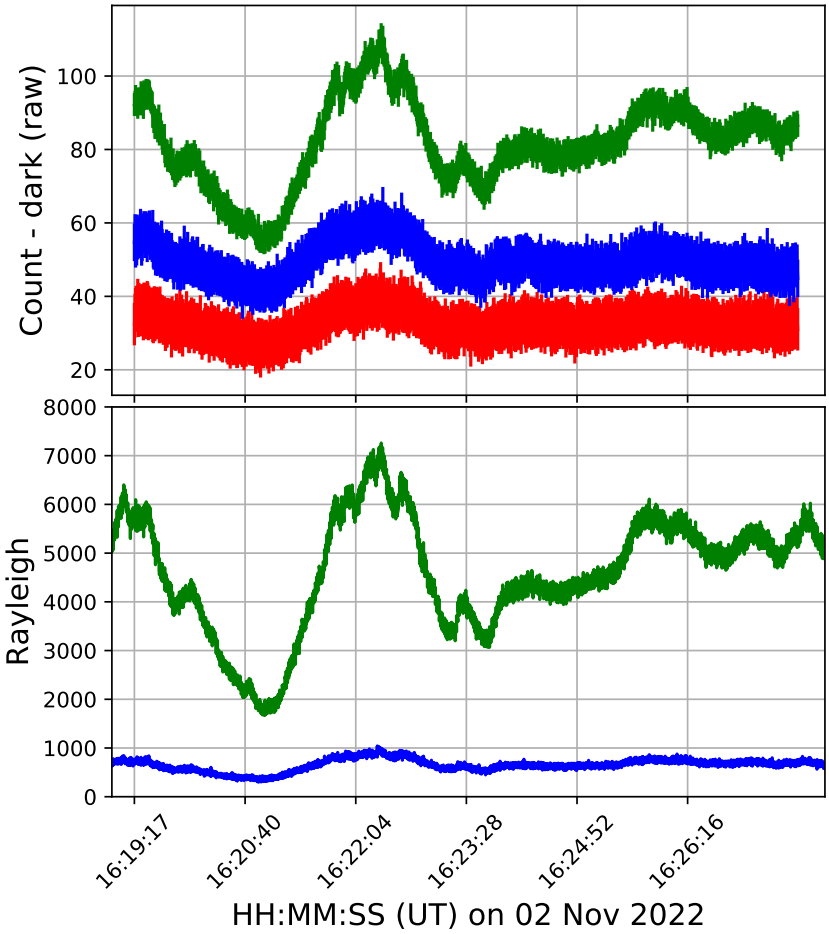

Figure 3.15: (Top) The time series of the RGB count values from Nikon D5. (Bottom) The time series of the Rayleigh values at 557.7 nm (green) and 427.8 nm (blue).

Figure 3.16 shows the correlation between the count values from the Nikon D5 and the Rayleigh value from the photometer. The green channel of the Nikon D5 shows a linear positive correlation with the Rayleigh value at 557.7 nm in the range of 1000–58000 R, while the blue channel shows a linear correlation between the Rayleigh value at 427.8 nm in the range of 100–8000 R. From this result, it is suggested that the B/G ratio is linearly correlated with the ratio of the emission intensity at 427.8 nm to that at 557.7 nm and would be used as an indicator of the average energy of the auroral electrons.

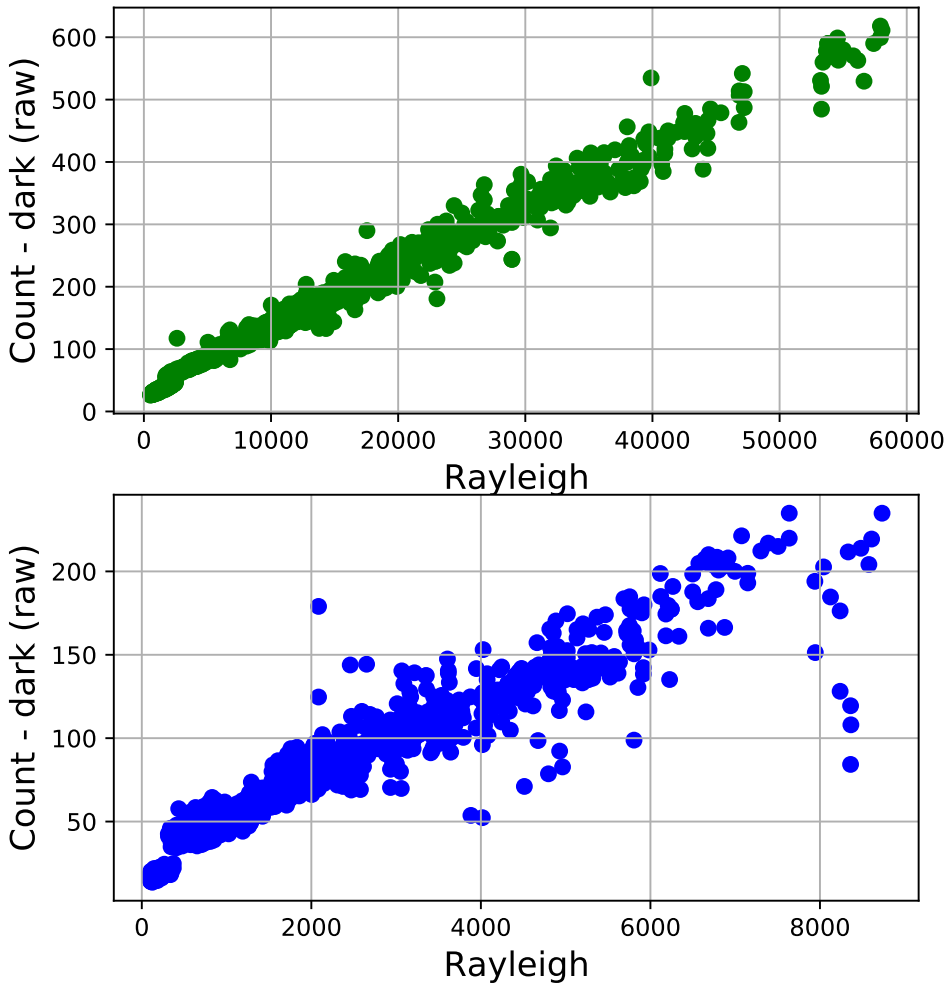

Figure 3.16: The correlations between the count values of the G and B channels and the Rayleigh values at 557.7 nm and 427.8 nm, respectively.

3.4 Summary

In order to quantitatively evaluate the implication from Chapter 2 that the B/G values of auroras in color digital camera images may correlate with the average energy of the auroral electrons, we tried to observe the aurora simultaneously with the Nikon D5 and EISCAT radar in Tromsø. In preparation for the observations, optical calibration experiments were performed to investigate how the RGB values respond to standard light sources. After evaluating the linearity of the count values to the light intensity and the transmission characteristics of the color filter, the Nikon D5 was installed at the Ramfjordmoen research station near Tromsø. In this observation, the camera took photographs only during the appearance of auroras to reduce the wear and tear of the shutter unit and the storage. The appearance of auroras was detected using a deep learning model for multi-class classification of images. Since this model can calculate the auroral occurrence rate, the image classification was carried out on the last ten years of data. Then, we conducted a statistical analysis of the occurrence rate. The results showed good agreement with those from the visual detection, indicating that automatic detection of auroras can be performed at a high level over a long period. Furthermore, a web application, "Tromsø AI," was released to allow users to get real-time notifications of the appearance of auroras, making it easier for tourists and photographers to take pictures of auroras. With this model, the Nikon D5 observed the aurora only during its appearance. Although simultaneous observations of auroras with the EISCAT radar have not been made yet, comparisons with observations by the all-sky camera and photometer were conducted. Compared to the all-sky camera, the Nikon D5 has a narrower FoV. However, the spatial resolution is higher, and thanks to its short exposure time, the Nikon D5 can capture the pink emission of nitrogen molecules, possibly manifesting highly energetic electron precipitation. Comparison with the photometer showed that the G and B channel counts correlate positively with the Rayleigh value at 557.7 nm and 427.8 nm, respectively. This result confirms the feasibility of using the B/G ratio as an indicator of the average energy of the auroral electrons. The still imaging described in this chapter indicates that the data from the commercial digital camera can be used quantitatively for scientific research on auroras. Following these results, in Chapter 4, we will capture videos of auroras to

further evaluate to what extent commercial digital cameras can visualize the fast temporal variation of auroras.

Chapter 4

Video Recording by the Sony α7SIII and Evaluation of Data

4.1 Aim and observation workflow

The observations performed in Tromsø, described in Chapter 3, were intended to evaluate the accuracy of the auroral colors as an indicator of the average energy of the auroral electrons. So far, no comparison with the measurement from the EISCAT radar has been made, but comparisons with the photometer showed that the count values in the green and blue channels of the Nikon D5 correlate linearly with the Rayleigh values at 557.7 nm and 427.8 nm, respectively. This result indicates that the data from the commercial digital camera can be used for quantitative analyses of several auroral emission lines. For these quantitative observations in Tromsø, we carried out the still imaging to clone the digital camera observations from ISS. Following these results, in this Chapter, we took videos of auroras using the Sony α7SIII camera in Kiruna, Sweden, to evaluate the performance of commercial digital cameras further, for example, for detecting fast variations of auroras. The reason for using the Sony camera is that it is easy to record a video by a Linux machine using the official software development kit (SDK). Nikon has not published such an SDK.

In Tromsø, the camera was fixed toward the zenith because the primary purpose of that measurement was to compare the data with the EISCAT radar and the photometer in the same location. By contrast, for the observations in Kiruna, we try to change the direction of the camera to the direction of an aurora to increase the number of data

because auroras move rapidly and appear anywhere in the sky. In order to achieve this, we first divided the real-time all-sky image from a different all-sky camera in the same observatory into 49 small regions and then classified each region into four classes: the strong, moderate, weak auroras, and no aurora classes. ResNet-50, the same as the one used for Tromsø AI, was trained with the training dataset and used as the model. When auroras appear in multiple regions, priority is given to a region close to the zenith (with the largest elevation angle), as the emission at the magnetic zenith purely responds to electron precipitation along a single magnetic field line. The camera was installed on the gimbal DJI RS 2 to control the camera orientation. It was controlled by giving the gimbal the elevation and azimuth angles obtained from the above procedure. The gimbal control program was from the method developed by Yamashina et al. (2022) with minor modifications, where the gimbal communicates with a computer via a Controller Area Network (CAN) converter for the CAN communication.

Figure 4.1 shows the overall workflow of the observation. The observation starts with downloading the latest all-sky image, as shown in the red square in the upper left corner. Then, the model determines if the aurora appeared anywhere in the image. If an aurora appears and the video recording has not already begun, the observation starts as shown in the yellow square. The all-sky image is then divided into 49 regions to estimate the locations of auroras, and the gimbal is controlled to point the camera in the direction of the aurora. Since the time resolution of the all-sky image is one minute, the program stops for one minute here and returns to the red square if the recording time does not exceed 60 minutes. The recording will stop either when the auroras disappear or when 60 minutes have elapsed from the start of the recording. The reason for stopping at 60 minutes is that it is difficult to handle and analyze video files that are too long, and there is concern that the camera will heat up and increase noise in the video.

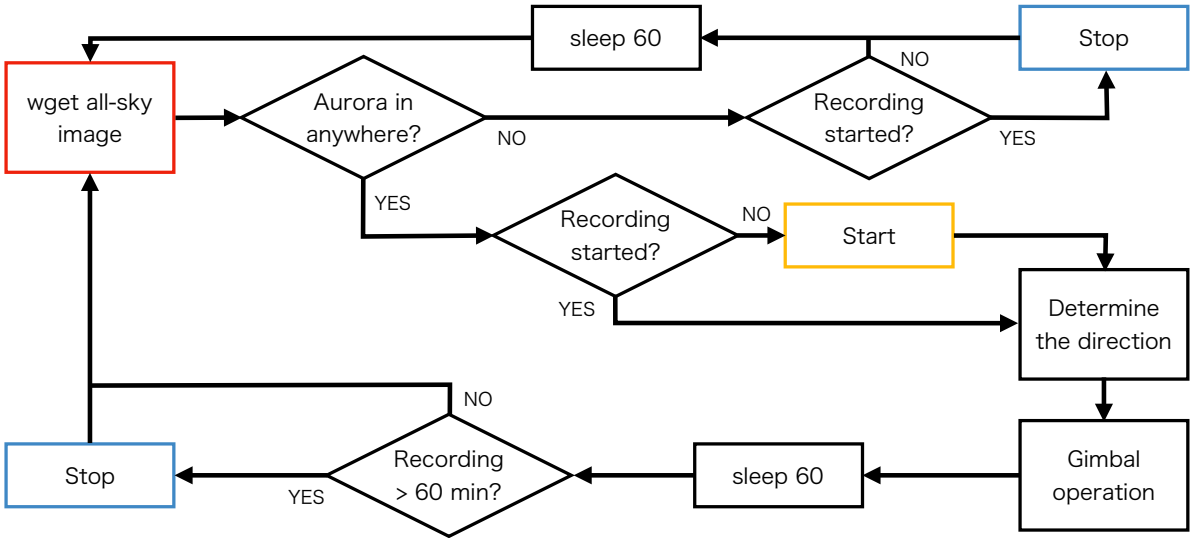

Figure 4.1: The workflow diagram of the observation in Kiruna, Sweden.

Figure 4.2 shows an example result of auroral region detection (left) and a snapshot of the video obtained with the Sony α7SIII at the same time as the left panel (right). In the left panel, the auroral breakup occurs in the south (lower side), and several regions are colored red, orange, and yellow. Each color corresponds to strong, moderate, and weak auroras, respectively. The breakup aurora is colored red, indicating that the detection was generally successful. The area marked with a cross, where both the brightness and elevation angle are large, was selected as the pointing direction of the camera. The white line indicates the FoV of the Sony α7SIII, and the snapshot of the actual movie is shown on the right. Compared to the all-sky camera, the FoV of this camera is narrower, but the spatial resolution is higher; thus, the structure along the magnetic field lines of the breakup aurora is finely visualized.

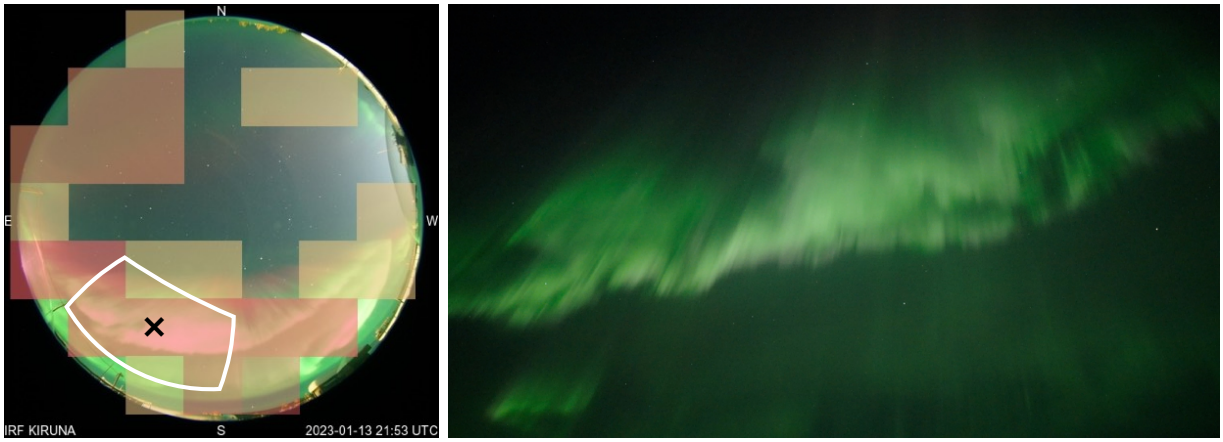

Figure 4.2: (Left) The estimation of the regions of auroral appearances. The red, orange, and yellow regions correspond to strong, moderate, and weak auroras, respectively. The cross-mark indicates the region that was chosen as the observation point. The white region represents the FoV of the Sony α7SIII. (Right) A snapshot taken by the Sony α7SI II at the same time as the left panel.

4.2 Optical calibration

The settings of the Sony α7SIII for the observations are as follows:

- Frame rate (time resolution): 30 frames per second
- Exposure duration: 1/30 sec
- ISO sensitivity: 80000
- Number of pixels: 1920×1080 pixels
- Bit depth of the RGB values: 8 bits (0–255) for each RGB
- Picture profile: S-Log3

While it was possible to store the counts of RGB values in the still imaging, most commercial digital cameras cannot store the counts in the video recording. When commercial digital cameras convert count values to an 8-bit depth quantity, such as JPEG or mp4, they adjust the colors to a shade that humans feel beautiful. The mapping function

used for this procedure is generally private. Besides, since the adjusted RGB values are not linear to the light intensity, it is difficult to use the converted RGB values in images for scientific research.

Some Sony cameras can invert the 8-bit RGB values into quantities that have linearity to the light intensity by recording a video as an mp4 file with a picture profile called S-Log3. Sony's official white paper provides a mapping function for carrying out a conversion between RGB and count values when capturing the S-Log3 profile. Figure 4.3 is the mapping function, where the horizontal axis represents the RGB values in the mp4 file, and the vertical axis represents the reconstructed count values. To evaluate whether the reconstructed count values are linear to the light intensity, the same experiment as in Section 3.5.1 was performed at the NIPR. The left panel of Figure 4.4 shows the spectra of the light in the integrating sphere, and the right panel shows the response of the reconstructed count values. In all the RGB channels, the reconstructed count values have linearity to the light intensity within a standard deviation.

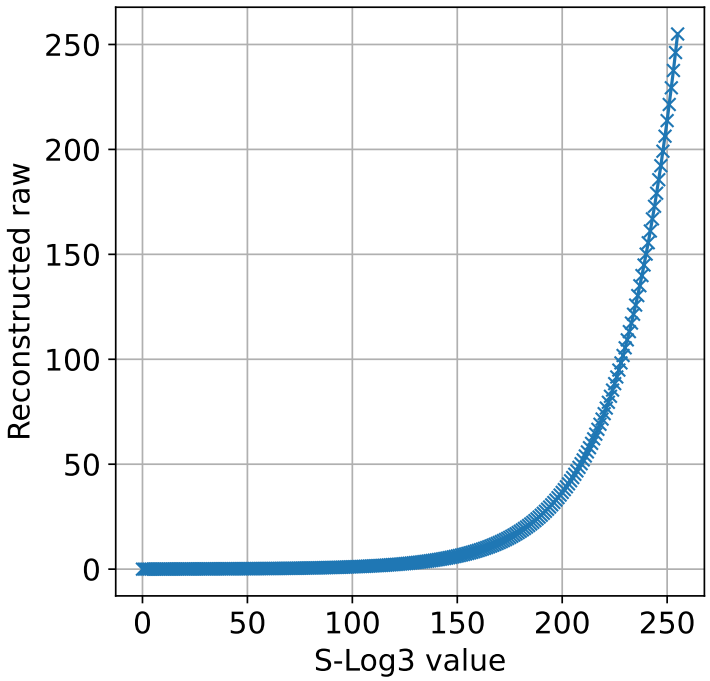

Figure 4.3: The mapping function between the S-Log3 value and the reconstructed raw value.

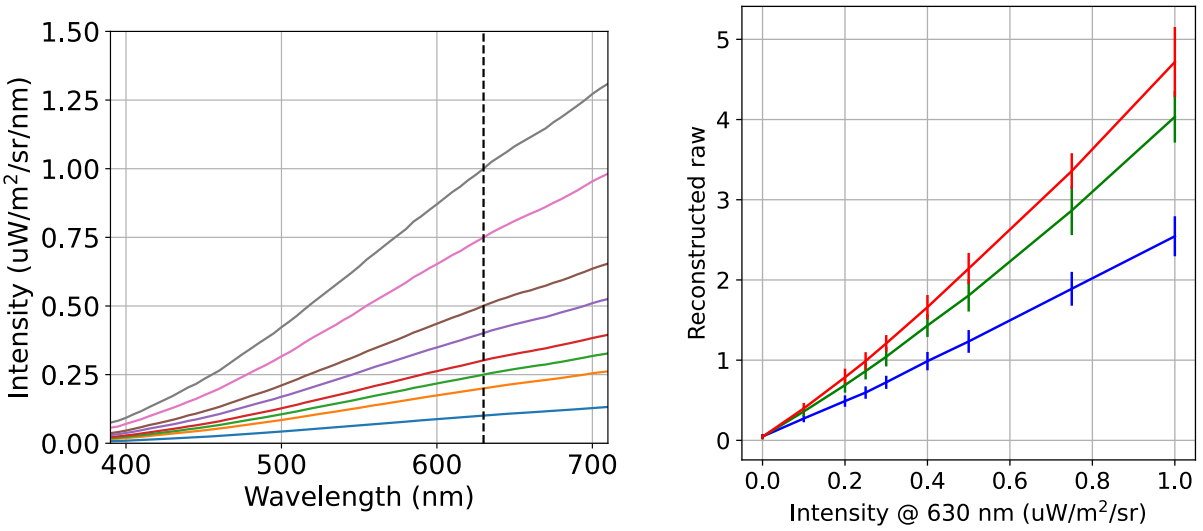

Figure 4.4: (Left) The spectra inside the integrating sphere for various representative intensities. (Right) The reconstructed raw values in the RGB channels of Sony α7SII I. The horizontal axis represents the intensity of light at 630.0 nm inside the integrating sphere. The error bars have been derived as standard deviation values of the reconstructed raw count at the center pixel among 1,000 images.

Figure 4.5 shows the profiles of the standard deviation of the reconstructed count values estimated from the experiment with the integrating sphere. In the integrating sphere, the light intensity was varied in 8 steps, as shown in the left side of Figure 4.4. A movie was taken for each of them, 1000 snapshots were sampled from each movie, and the standard deviation of the total 1000 values at each coordinate was calculated repeatedly to obtain the scatter plots in Figure 4.5. The solid line is a quadratic fitting to each scatterplot. The wavy signature in the scatterplots means that the standard deviation of the count values varies with the intensity of light. This may be due to the fact that S-Log3 sampling is not linear with the light intensity, as suggested in Figure 4.3 because this occurs even before the reconstruction of the RGB values.

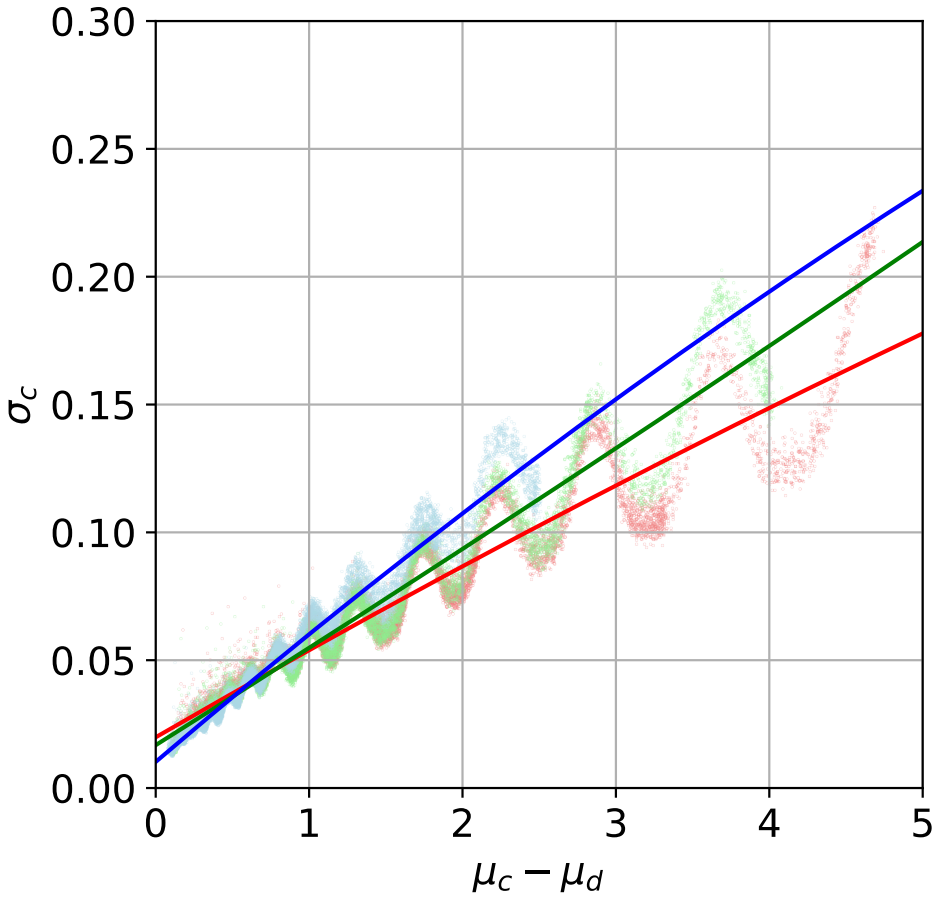

Figure 4.5: Evaluation of the standard deviation of the reconstructed raw values from Sony α7SIII. The horizontal axis represents values subtracted by the dark count from the original count values. The vertical axis represents the standard deviation at each pixel in the center column among 1000 images.

Averaging the counts at neighboring pixels (called binning) reduces the variance of the RGB values. Figure 4.6 shows the relationship between the number of averaged pixels and the standard deviation. The solid lines were obtained by averaging the RGB values at the pixels around the center of the images and then calculating the standard deviation among the 1000 images. The dashed lines are the curves when the standard deviation decreases with the square root of the number of averaged pixels. These are the curves for an ideal sensor without readout and dark current noise. The SNR of the count value in a

normal (non-ideal) sensor is expressed by the following equation:

$$\mathrm{SNR} = \frac{Q_E N_P}{\sqrt{\sigma_D^2 + \sigma_R^2 + \sigma_S^2}} \tag{4.1}$$

where Q_E is the quantum efficiency, N_P is the number of photons incident on the sensor, and σ_S, σ_D and σ_R are the shot noise, dark current noise, and readout noise, respectively. The shot noise is the variation due to the fact that the number of photons emitted from the light source follows the Poisson distribution. Thus, the shot noise is expressed by $\sigma_S = \sqrt{Q_E N_P}$, and then Equation 4.1 is:

$$\mathrm{SNR} = \frac{\sigma_S^2}{\sqrt{\sigma_D^2 + \sigma_R^2 + \sigma_S^2}}. \tag{4.2}$$

The dark current noise occurs even when no light penetrates the sensor and is affected by the heat on the sensor. The readout noise is generated when the number of photons incident on the sensor is converted to a count value and is affected by the design of the sensor and the electronic components of the camera. In an ideal sensor, the dark current and readout noise can be ignored. Thus, the SNR is:

$$\mathrm{SNR}_{\mathrm{ideal}} = \sigma_S = \sqrt{Q_E N_P}. \tag{4.3}$$

This equation indicates that the SNR increases according to the square root of the number of coordinates N used in binning. If we want to increase the SNR by a factor of 10, we can bin the count values between 100 pixels. However, the SNR did not increase by a factor of 10 unless 34^2 pixels were binned together in the experimental values, shown by the solid lines in Figure 4.6. This would be because the actual measurement is affected by dark current and readout noise. In particular, in this experiment, binning was achieved by averaging pixels after the imaging (called software binning). As a result, the substantial influence of readout noise would lead to a considerable difference between the ideal and experimental values.

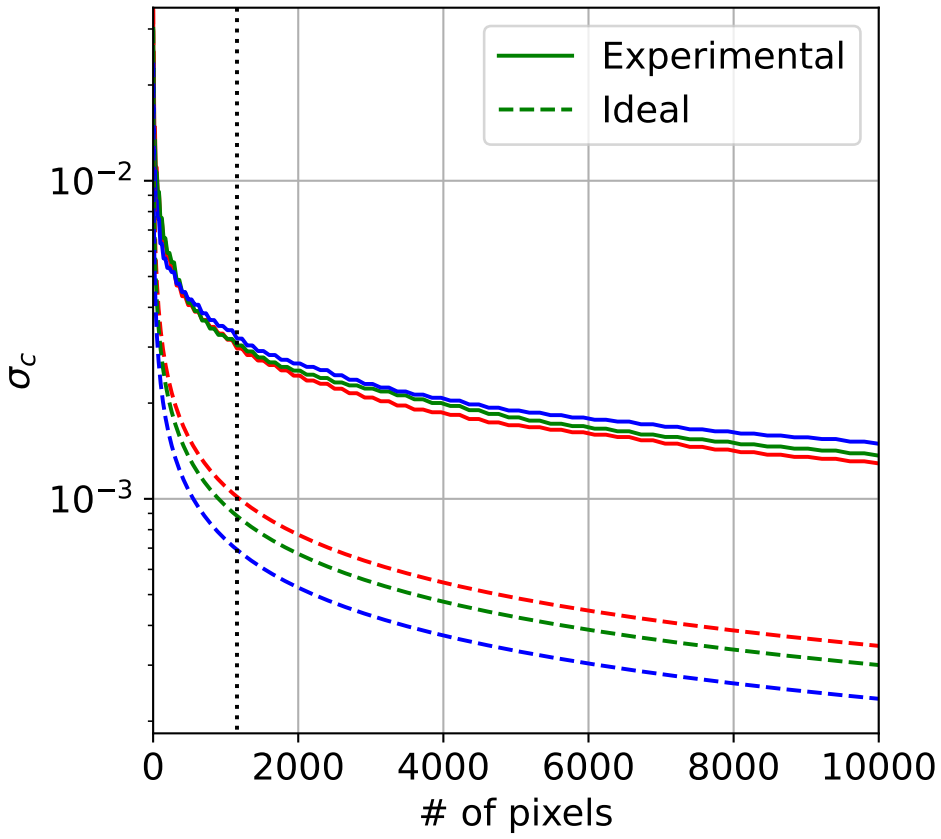

Figure 4.6: The relationship between the number of the averaged pixel and the standard deviation. The solid lines indicate the experimental values and the dashed lines indicate the equation $\sigma_c = \sigma_0/\sqrt{N}$, where σ_0 is the standard deviation of one pixel.

Similar to the optical calibration for the Nikon D5, the transmission characteristics of the color filter were derived using the monochromator at NIPR, as shown in Figure 4.7. Compared to the Nikon D5, the transmission curve of the red channel is distributed over a wide range from 470 nm, but the sensitivity of the green to the 557.7 nm emission and that of the blue to the nitrogen band emission are almost similar to those of the Nikon D5.

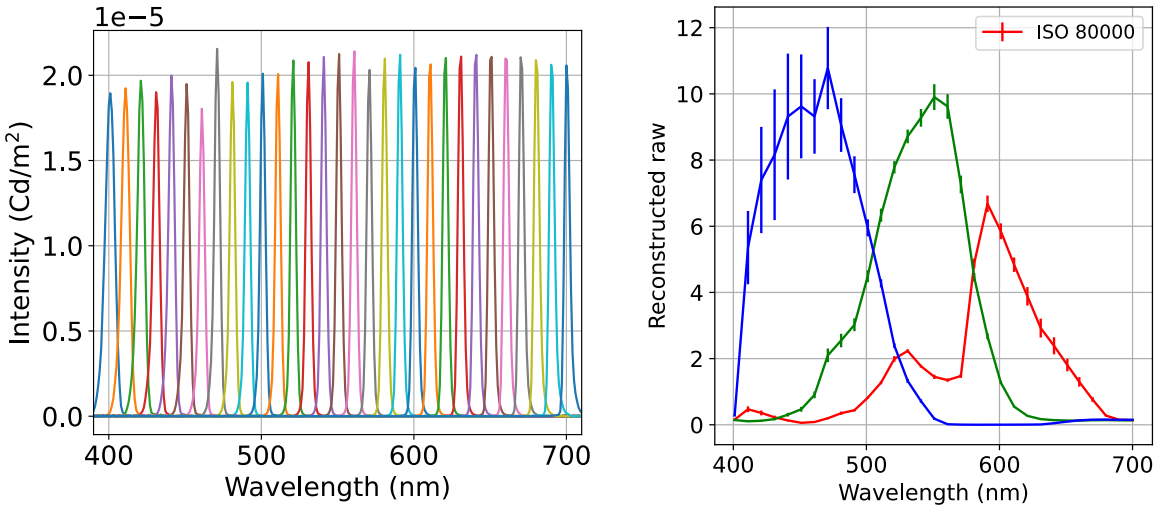

Figure 4.7: (Left) The spectrum of the light source from the monochrometer. The measurements have conducted with 31 individual spectra. (Right) The transmission characteristics of the color filter of the Sony α7SIII measured using the light source from the monochrometer.

After the calibration experiments, the Sony α7SIII and gimbal were installed at the Swedish Institute of Spece Physics (IRF) in Kiruna, Sweden, and observations were made. The geometrical calibration was performed in the same way as for the Nikon D5. Now, the data were comparable with those from ALIS, the other auroral camera installed at IRF, as shown in Figure 4.8. Because the ALIS camera has a wider FoV than the Sony α7SIII, we can put an image from the Sony α7SIII on the image from the ALIS camera observed at the same timing. The image from the ALIS camera was derived with a narrow-band filter, which enables it to detect only the green line emissions. The shape of the aurora was generally consistent around the edge of the image from Sony α7SIII, suggesting the geometrical calibration worked well. In the following sections, we introduce the scientific results of the observations.

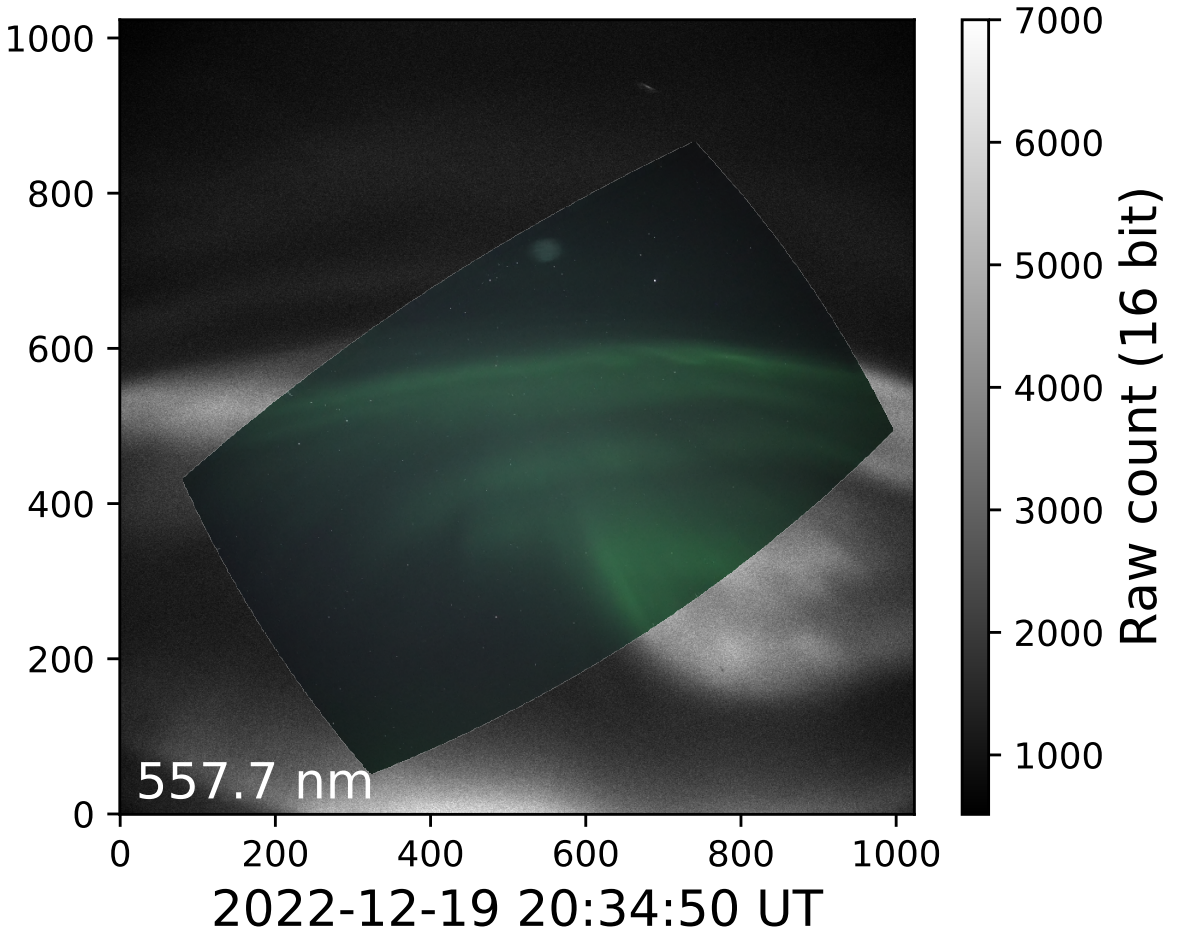

Figure 4.8: The comparison between an image from the ALIS camera and one from the Sony α7SIII. The image from the Sony α7SIII is embedded in the image from the ALIS camera because the ALIS camera has a wider FoV.

The targets of this video recording measurements are 1) the shock aurora, which will be reported in Section 4.3, and 2) the internal modulation of PsAs, which will be briefly introduced in Section 4.4. Both the scientific targets are known to move dynamically and change their brightness quite rapidly; thus, the tests using these phenomena would help evaluate the performance of this system itself and the commercial digital camera for high-speed imaging of auroras.

4.3 An observation case: the shock aurora

4.3.1 Introduction to the shock aurora

Geomagnetic sudden commencement (SC), caused by a rapid increase in solar wind dynamic pressure, consists of a stepwise increase and subsequent bipolar spike in the geomagnetic field (Araki, 1994, and references therein). The resultant geomagnetic Disturbances are detected both at Low latitudes, DL, and the Polar regions, DP. DP is normally divided into two parts: the preliminary pulse, PI, and the main pulse, MI. Following the model of Araki (1994), PI is associated with a pair of field-aligned currents (FACs) flowing into (out of) the afternoon (morning) auroral zone near the polar cap boundary while traveling anti-sunward. PI is replaced some minutes later by MI, that is, stationary FACs flowing in the opposite direction from PI.

Both disturbances are ultimately caused by an intensification of the magnetopause current, of which the information related to DL propagates globally across the geomagnetic field as the compression carrying FACs at dawn and dusk edges and appears almost simultaneously (less than tens of seconds) at all magnetic local time (MLT) regions. The information related to DL propagates as the Alfvén mode that carries FACs along the geomagnetic field, creating the dusk-to-dawn and dawn-to-dusk ionospheric electric fields and other related current systems. DP (actually the PI part) also appears nearly simultaneously at all latitudes, although it is related to a current system that takes time to develop. This is because the related electric field in the ionosphere can propagate almost instantaneously as a waveguide mode (Kikuchi, 2014).

Directly related to the SC, an optical aurora, called the "shock aurora" (Zhou et al., 2003) has been observed from space (e.g., Craven et al., 1986; Zhou and Tsurutani, 1999) and ground (e.g., Kozlovsky et al., 2005; Zhou et al., 2009; Liu et al., 2011). It is typically colocated with the intensification of the SC-related FACs in the dayside (Motoba et al., 2009). Nishimura et al. (2016) obtained the spatial distribution of FACs and their temporal development using the magnetometer network in the northern hemisphere and compared it with images from an all-sky camera (ASC) in Antarctica. They concluded that the afternoon PI and MI likely correspond to diffuse and discrete auroras, respec-

tively. Motoba et al. (2014) examined a shock aurora at 15 MLT under the southward interplanetary magnetic field (IMF) and identified three successive transient arcs (at 557.7 nm: green) shifted equatorward with an abrupt jump. These arcs appeared during the PI phase but could also be related to DL, which is hidden in the PI signature at such an MLT region. For the northward IMF, the MI-related arc may appear poleward of or overlap with the pre-existing arc, resulting in an enhancement of the oval (Nishimura et al., 2016).

Optical observations of auroras provide finer FAC information, such as location and structure, than a network of geomagnetic field measurements. Thus, the optical observation should have been conducted on the nightside to understand how the SC current system develops as it propagates to the nightside or whether the auroral morphology is the same after long propagation from the dayside to the nightside. However, it is difficult to observe a shock aurora on the nightside due to the convolution of the nightside-driven aurora. Only a photometer observation with a narrow and zonal field-of-view (FoV) has been reported for the nightside observation of the shock aurora (Holmes et al., 2014).

According to the global imaging from the satellite, the MI(PI)-related electron aurora propagates anti-sunward at about 4–6 km/s (10 km/s) on the duskside (dawnside) ionosphere (Zhou and Tsurutani, 1999; Holmes et al., 2014), and the shock aurora can extend to the midnight sector. Utilizing multiple scanning photometers installed independently, with approximately 1100 km separation in the evening sector and 900 km in the morning sector, Holmes et al. (2014) have demonstrated that the anti-sunward propagation speed of the shock aurora is consistent with the result from satellite observations. The derived propagation speed towards the evening sector was constant on a global scale at about 1–1.5 MLT/min, taking 8 min for propagation from dayside to nightside (20–22 MLT). This is roughly consistent with the 6-min delay of the start of the observed MI signature in the nightside after the SC onset (Holmes et al., 2014).

Holmes et al. (2014) also detected the red (630.0 nm) aurora 1 min before the appearance of the green (557.7 nm) aurora. This result indicates that low-energy electrons may have precipitated into the ionosphere 1–3 min before the high-energy ($>$ 1 keV) electrons if we consider the average relaxation time of the 630-nm emission of about 110 sec. The FAC associated with the duskside red aurora must have arrived much earlier

than the source FAC for the green aurora in Holmes et al. (2014), giving a quite different anti-sunward propagation speed between the sources of the red and green auroras.

To summarize our understanding, there are two forms of shock aurora in addition to the pre-existing arc: diffuse aurora and discrete arc. However, our knowledge of the differences in the propagation speed, local development, forms in the dayside and nightside, and relationship to the geomagnetic signature for these auroral types remain incomplete. Fortunately, these different auroral forms might have different propagation speeds (Holmes et al., 2014), making a larger difference in the appearance timing on the nightside than on the dayside. With modern high spatial- and temporal-resolution cameras and a dense magnetometer network in the auroral region, we must observe shock auroras on the nightside sector without the contamination of nightside-driven auroras such as substorm-related auroras.

On 26 February 2023, right after an SC onset was detected at 19:24 UT, a color ASC in Kiruna (65°geomagnetic latitude) that was located at 21 MLT detected the following signatures: (1) intensification of the pre-existing green arc at 19:25 UT, (2) appearances of a red diffuse aurora at 19:28 UT, and (3) secondary green arcs at 19:31 UT. The MI peak was detected at 19:27 UT with ground-based magnetometers in northern Scandinavia. In addition, the development of the fine structure, i.e., vortex motion, of the secondary arcs was further analyzed using a high-speed wide-angle camera. The shock aurora was weakened within 20 min, and this interval was isolated from the subsequent substorm growth phase. The shock aurora appeared above the densely distributed magnetometer network (IMAGE), and the relative location of FACs and aurora can be derived in good resolution. Both SYM-H and ASM-D indices were close to zero during this interval, indicating that the shock aurora was not contaminated by nightside-driven auroras. Here, we report these combined observations of the shock aurora seen three hours before the magnetic midnight.

4.3.2 Instruments

All-sky cameras (ASCs)

We have analyzed all-sky color images from commercial digital cameras in Kiruna, Sweden (67.83°N, 20.42°E) and Skibotn, Norway (69.35°N, 20.36°E). In Kiruna, the Sony α7S with the Nikkor 8mm F2.8 lens was installed and aligned to the geomagnetic north. The camera's ISO was set at 4000, and the exposure time was 10–13 sec. At Skibotn Observatory, the Sony α6400 with the MEIKE MK-6.5mm F2.0 lens was used. The ISO was set at 8000, and the exposure time was 8 sec. Images were taken every 30 sec. We used these images to geolocate and identify spatiotemporal variations of the shock aurora.

Wide-angle camera (WAC)

The Sony α7SIII with the FE 24mm F1.4 GM lens was installed in a dome where the Kiruna ASC was located. This camera called the wide-angle camera (WAC), was faced in the north-northeast direction at a low elevation with an angle of view of $\sim$73 degrees horizontally. A white rectangle in the last panel of Figure 4.10 marks the actual observation area. The data is available only after 18:32 UT due to an operational issue. WAC recorded a video at 30 frames per second, offering a high temporal resolution for visualizing auroral movement within one minute. WAC has an image size of 1920 $\times$ 1080 pixels, an ISO sensitivity of 80000, and a 1/30 second exposure time. We averaged 15 images (for 0.5 seconds) to make snapshots to reduce noise, as shown in Figure 4.11.

Magnetometers

A selection of magnetometers from the IMAGE network has been applied in the study. These are stable flux-gate magnetometers that provide 10-second resolution data. Additionally, in the low latitude, an Intermagnet magnetometer at Huancayo has been used.

4.3.3 Observation results

Figures 4.9a and 4.9b show the IMF (total in black and the z component in red) and solar wind dynamic pressure, respectively, from the Deep Space Climate Observatory

(DSCOVR) at the L1 point. A stepwise increase in the IMF intensity and dynamic pressure was observed around 18:40 UT. Other solar wind parameters shown in Figure S1 were also enhanced, a common signature of the interplanetary shock. Figure 4.9c shows the H component of the geomagnetic field recorded by magnetometers located in Sørøya (SOR), Norway (67.8 MLAT, 21.2 MLT); Tromsø (TRO), Norway (67.0 MLAT, 21.0 MLT); Kilpisjärvi (KIL), Finland (66.3 MLAT, 21.1 MLT); Kiruna (KIR), Sweden (65.1 MLAT, 21.0 MLT); and Huancayo (HUA), Peru (-0.6 MLAT, 14.2 MLT). Their locations, except HUA, are shown in Figure 4.9h. HUA is instead located on the dayside equator at $\sim$14.2 MLT, which is close to the impact local time of 11–14 MLT. The impact region can be estimated from Figure S2. All the stations exhibited the SC signature starting at around 19:24 UT.

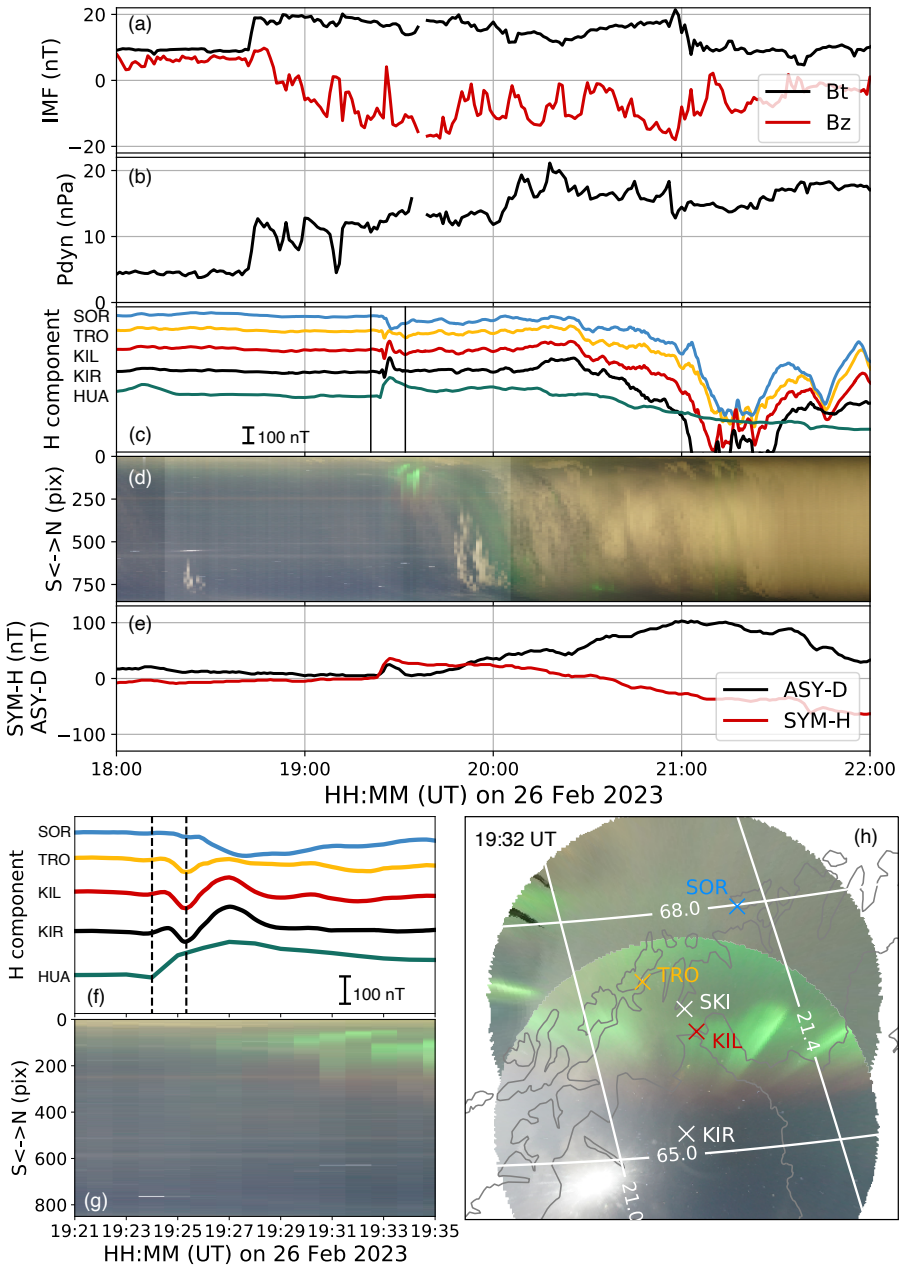

Figure 4.9: (a–b) The intensity (black) and z component (red) of the interplanetary magnetic field and solar wind dynamic pressure from DSCOVR. (c) Magnetometer data from the stations in the auroral and equatorial regions. A scale of 100 nT is shown in the lower left. (d) North-to-south keogram from the Kiruna ASC. (e) The ASY-D and SYM-H indices. (f–g) Close-up views of panels (c) and (d) from 19:21 to 19:35 UT. Vertical dashed lines indicate the onset of the SC and peak time of the PI. (h) Projection of all-sky images from the Kiruna and Skibotn ASCs. The location of the magnetometers is also shown. The grid line gives the magnetic local time and latitude.

In panel (e), both ASY-D and SYM-H were close to zero before the SC onset, and then ASY-D decreased together with the DP signature, and SYM-H kept stable positive values. All these behaviors indicate that the entire event, about 20 min after SC onset, is free from magnetotail-initiated activities, such as substorms. In the close-up data from 19:21 to 19:35 UT in panel (f), the onset time at ∼19:24:00 UT is marked by the left-side dashed line. Similarly, the peak time of the PI at ∼19:25:20 UT is also marked by the right-side dashed line. The MI peak was around 19:27 UT. According to Ampere's law, the convergence of the H component means the existence of upward FACs in the northern hemisphere, and its intensity became largest at ∼19:27 UT, i.e., 3 min after the onset, between SOR and KIL.

Figures 4.9d and 4.9g show the keogram, the time series of the geomagnetic north-south cross-section of the all-sky images from the ASC in Kiruna. Note that the exposure time changed from 10 sec to 13 sec at 19:28 UT. The keograms show that the aurora appeared several minutes after the SC onset, and its brightness gradually enhanced for the first ∼10 min. In Figure 4.9h, all-sky images obtained by the ASCs in Kiruna and Skibotn at 19:32 UT are projected on the map, showing the locations of the magnetometers and cameras. Coordinates with an elevation angle of more than 20 degrees were used for the projection, and the auroral emission layer was assumed to be at 100 km altitude. The projected aurora was distributed close to the zenith of Kilpisjärvi and Tromsø. In addition, we projected the all-sky image at 250 km altitude, and it is available as Figure S3.

Figure 4.10 is a minute-by-minute all-sky image from 19:23 to 19:34 UT. The upper side of each image is north, and the right side is west and sunward. The solid white line in the first panel shows the cross-section used to make the keograms shown in Figure 4.9. The first all-sky image taken before the SC onset already shows a weak arc-like aurora as circled by the white dashed line in the northeast direction. In this paper, we refer to this aurora as the pre-existing arc. The third all-sky image at 19:25 UT, taken 1 min after the onset, shows that the pre-existing arc was getting brighter than before, as indicated by the yellow arrow.

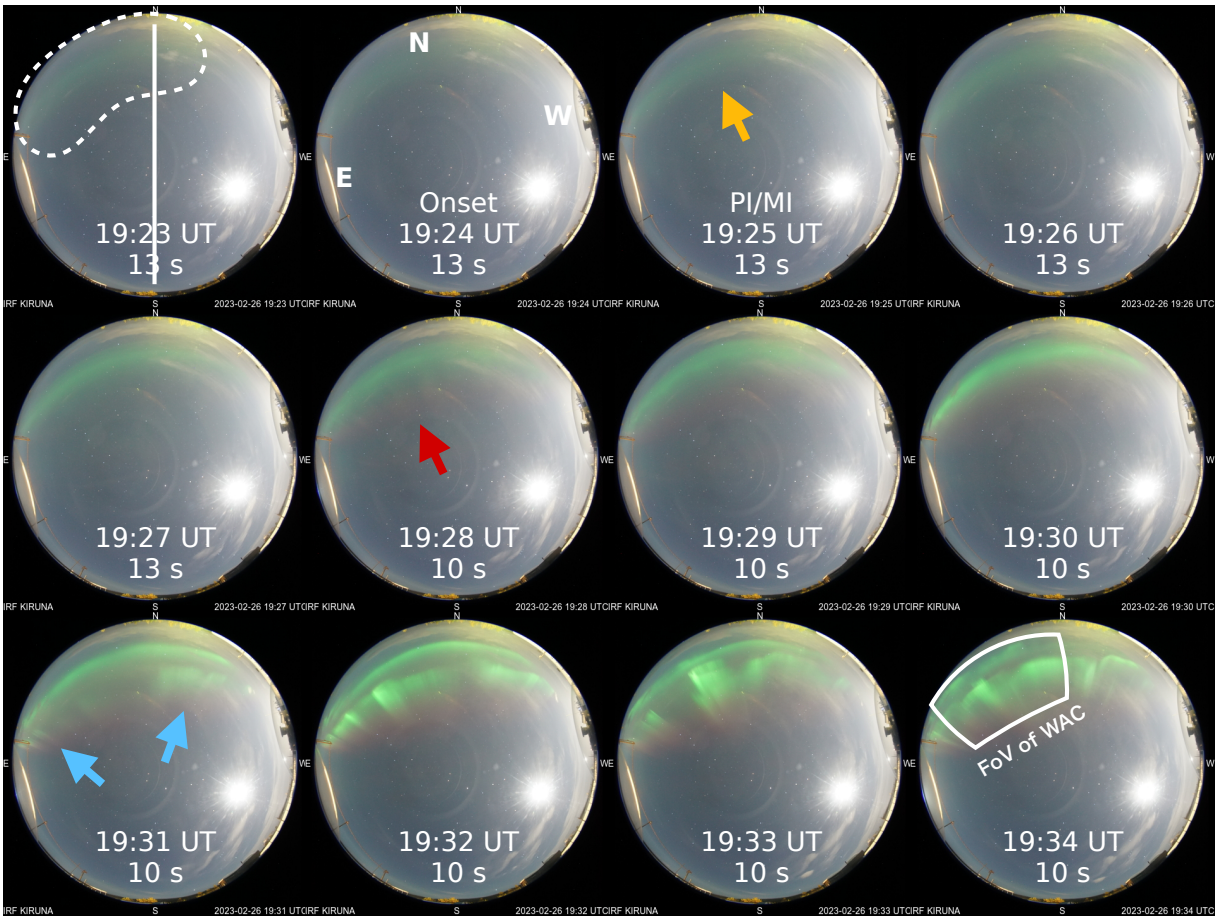

Figure 4.10: The ASC images from Kiruna during 19:23–19:34 UT on 26 February 2023. The top is the geomagnetic north, and the left is the east. The white dashed region in the first panel shows the pre-existing arc. The appearance of the red aurora and secondary arc is marked by red and blue arrows, respectively. The white rectangle region in the last panel is the FoV of the images shown in Figure 4.11.

At 19:31 UT, discrete green arcs with wavy structures were detected southward (equatorward) of the pre-existing arc at the west (right) and east (left) sides. In this paper, we refer to these arcs as the secondary arcs. Both the secondary arcs were brightened at 19:32 UT and formed a complex structure from west to east afterward. The last four all-sky images (19:31–19:34 UT) show the quick evolution of the secondary arc and the gradual northward shift of the pre-existing arc.

In addition to these green auroras, a red aurora, as indicated by the red arrow, became visible at 19:28 UT. The red aurora gradually intensified until 19:33 UT and stayed at

the same location without any distinct structure. In the all-sky images, the red aurora is located southward of both green arcs. However, it can also be a high-altitude extension of the secondary arc, i.e., green and red auroras might be on the same magnetic field lines because the red aurora was projected at the same location as the secondary arcs in Figure 4.9h with the assumed emission layer of 250 km, as illustrated in Figure 4.12. This co-location is discussed in the Discussion section.

We can further examine the exact fine spatiotemporal evolution of the secondary arc with a 30-Hz video taken by WAC. WAC captured the white rectangle region in the last all-sky image in Figure 4.10. Figure 4.11 shows the snapshots of the video. The images obtained from 19:34.12.1 to 19:35:08.1 UT are shown every 8 sec. Note that both the east-west and north-south directions are reversed from the all-sky images in Figure 4.10. The meridian with an azimuth angle of 0 degrees (northward) is shown as a dotted line in panel (a).

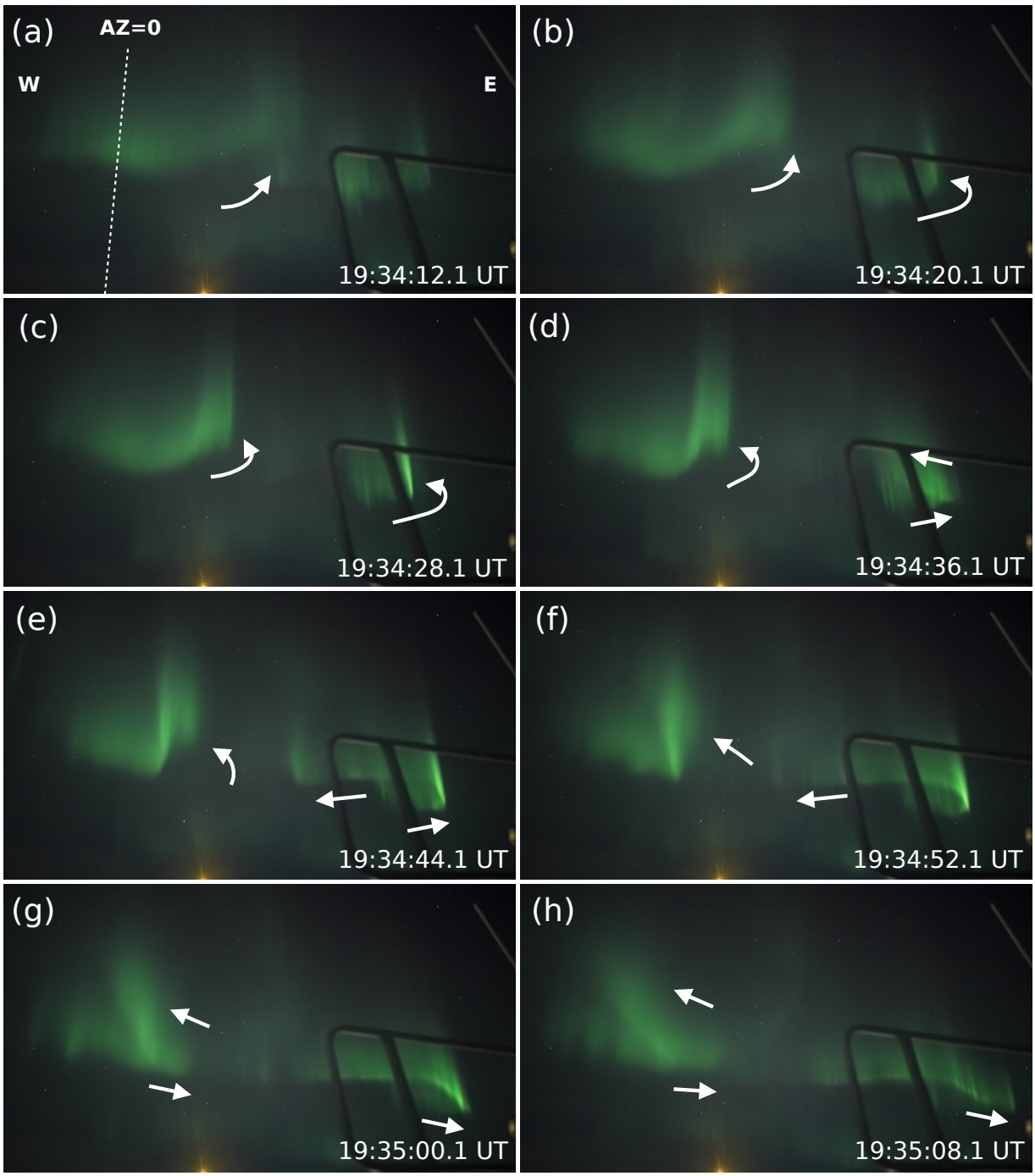

Figure 4.11: The images captured by WAC from 19:34:12 to 19:35:08 UT. The right side is east (different from the ASC image). The white dashed line in the first panel indicates the meridian, which has an azimuth angle of 0 degrees (towards the geographic north). The white arrows guide the vortex motion.

In each snapshot, two auroral structures shown as secondary arcs in the ASC are visible with a spatial gap near the center of the image. Both wavy structures gradually fold by the combination of westward motion on the front side (low latitude side) and eastward motion on the back side (high latitude side), as indicated by the white arrows. As this folding developed, these structures consequently formed a vortex shape.

We also examined a video from the EMCCD ASC in Tjautjas, Sweden, and found that the western and eastern arcs seen at 19:31 UT in Figure 4.10 appeared at around 19:30:52 and 19:31:12 UT, respectively. Both arcs appeared suddenly with a temporal gap and leaped eastward (anti-sunward) rather than propagated gradually. After both spotted arcs appeared, they started expanding in the east-west direction, as shown in Figure 4.12b, and connected to each other. Given the anti-sunward travel direction and the absence of any geomagnetic signature associated with nightside activity such as substorms, these spiraled arcs are still the dayside-origin shock aurora without influences of nightside geomagnetic activities. The modulation in the shape was also seen in the pre-existing arc, although it was less clear than the secondary arc.

4.3.4 Interpretation of the development of the shock aurora

A shock aurora was observed by ASCs and the high-speed WAC in the evening sector in response to the SC detected at 19:24 UT during quiet geomagnetic conditions. Their temporal developments are summarized in Figure 4.12, in which the locations of the aurora are illustrated in the polar view.

1. The pre-existing weak arc (green, most likely 557.7 nm) was gradually intensified right after the SC onset and then gradually shifted northward after 19:30 UT.

2. Red aurora (apparently 630.0 nm) without distinct structures gradually appeared widely in the longitudinal direction. This aurora became visible 4 min after the onset (19:28 UT), and its location was stable.

3. The discrete green secondary arcs appeared at two separated spots (west and east in the WAC images) on the equatorward of the pre-existing arc at 19:31 UT, i.e., 7 min after the SC onset and 4 min after the MI peak at Kiruna. They developed

locally to form a spiral-like structure. Afterward, both arcs stretched in the east-west direction and connected, as shown in Figures 4.12c and 4.12f.

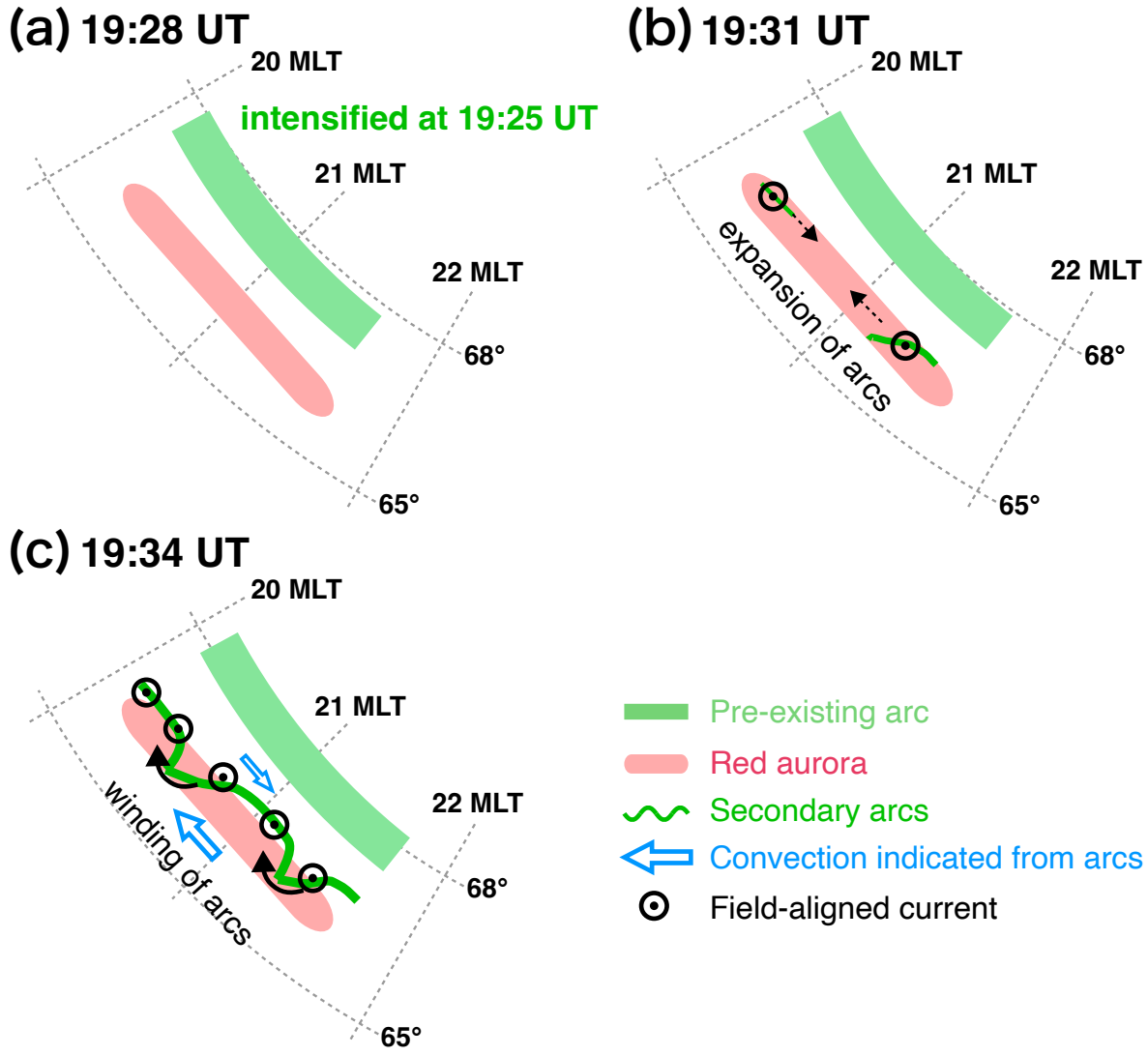

Figure 4.12: Schematic illustration of the relative locations of pre-existing arc, red diffuse aurora, and secondary arc. The coordinates of auroras were calculated by assuming the altitudes of green and red emissions were at 100 km and 250 km, respectively. The blue arrows indicate the convection directions suggested by the vortex motion of the secondary arc.

There are several unexpected features: (a) three aurora forms appeared instead of the previously reported two forms: PI-related diffuse aurora and MI-related discrete arc;

(b) secondary arcs developed as local vortexes at two spots that leaped eastward (anti-sunward) before the connection of arcs; and (c) the secondary arc appeared as late as 4 min after the MI peak. Although we do not have any statistics to prove commonness, there is no reason to deny the observed aurora as the nightside extension of the shock aurora.

The first feature raises a question about the relative location of the red aurora. Comparing Figures 4.9h (projection to 100 km altitude) and S3 (projection to the 250 km altitude), the red aurora is likely distributed at the same latitude as the secondary arcs, i.e., both auroras were on the same magnetic field line, as illustrated in Figure 4.12. Then, the first question is rephrased as whether the red aurora and the secondary arc were driven by independent mechanisms or the same acceleration mechanism. We consider both possibilities: (1) the red aurora and the secondary arc were vertically connected on the same field lines resulting from the same electron acceleration mechanism, and (2) they were independent, and a different mechanism from the secondary arc caused the red aurora. In both cases, the secondary arcs should be the MI-related aurora because this form and MI are the last signature of the optical signature and SC, respectively.

In case 1, it is possible to interpret this shock aurora as the same as the previous reports (PI-related diffuse aurora and MI-related discrete aurora). In this case, the intensification of the pre-existing arc is related to PI, whereas both the red aurora and the secondary arc are related to MI, and their auroral electrons are precipitated by the same mechanism. In this case, the question is how the red aurora of most likely 630.0 nm emission (110 sec lifetime caused by low-energy electrons) can appear before the secondary arcs of obvious 557.7 nm emission (0.7 sec lifetime caused by high-energy electrons). In this scenario, low-energy electrons must precipitate into the ionosphere several minutes before high-energy electrons. Although we have not yet identified a responsible mechanism, there could be some scenarios: the upward field-aligned electric field slowly developed after the passage of the MI signature in the magnetosphere, or wave scattering plays a role.

In case 2, the red aurora and the secondary arcs may correspond to the PI-related diffuse aurora and the MI-related discrete arc, respectively. Note that these previously reported pairs may overlap for northward IMF conditions (Nishimura et al., 2016). In this case, the intensification of the pre-existing arc could be triggered by DL, for example,

by changing the size of the magnetic flux of the existing FAC. In this case, we should re-examine the shock aurora observed by the meridian scanning photometers in Holmes et al. (2014) because we have one more choice (DL-related) in addition to two (PI-related and MI-related).

The second feature (vortex development and leap of the secondary arcs; cf., Figure 4.12c) suggests that the anti-sunward convection poleward of the arc and sunward convection equatorward of the arc have similar speeds. In the northern hemisphere, such a convection shear means a converging electric field and an upward field-aligned electric field. This is consistent with a converging Pederson current (and hence an upward FAC) that is indicated from the $\frac{d}{dx}\Delta B_x < 0$ sense of the observed MI at Kiruna in Figure 4.9f, where x is northward, and ΔB_x is a deviation of the northward geomagnetic component. The observation suggests that such an electric field is developed as a leap of local development before becoming a continuous arc. We have no answer as to how such a leap can be connected to the anti-sunward propagation of the SC signatures.

Here, we should note that the leaping speed of the secondary arcs (1.5 MLT/min estimated from the EMCCD ASC data) is consistent with the 7-min delay between the SC onset at 11–14 MLT (1–1.5 MLT/min) and also consistent with those of the reported MI-related arc in the afternoon sector (Motoba et al., 2009; Holmes et al., 2014; Nishimura et al., 2016). This value is closer to the fast-mode propagation of magnetosonic waves in the magnetosphere than to the speed of solar wind plasma through interplanetary space. Such an agreement strengthens the above assumption that the observed secondary arcs with the leaping characteristic are related to MI and indicates that the propagation of the MI-related aurora may be in the form of a leap rather than a gradual propagation.

The third feature is the time delay between the aurora and the geomagnetic signature (or ionospheric current). The intensity of FAC mentioned above was intensified at 19:26 UT with a peak at 19:27 UT (cf. Figure 4.9f), i.e., 2–3 min after the SC onset (19:24 UT). This means that the upward FAC (or MI signature) propagated from the dayside to 21 MLT faster than the MI-related arcs by 4–5 min (delay of the red aurora is 1–2 min, supporting case 1 in the first question). We have no solid answer to explain such a significant difference in the anti-sunward propagation speeds. This question also remains for future investigation.

The present observation raises many questions: development of the ionospheric convection, leap-like propagation of FAC, the relation between the aurora and the current system, etc. Fortunately, modern optical instruments are rapidly improving their sensitivity, and the number of optical stations is increasing. Furthermore, the upcoming SMILE (Solar wind Magnetosphere Ionosphere Link Explorer) mission to be launched in 2025 would give a long-time global UV monitor from almost the same location. Combining its image with improved ground-based optical observations will allow systematic studies of the shock aurora on the nightside. For example, the difference in latitude between the intensified pre-existing arc and MI-related aurora will help to interpret satellite images and improve numerical simulations.

4.4 An observation case: the internal modulation of PsA

As introduced in Section 4.2, the observations by the Sony α7SIII have a time resolution of 1/30 second, which, according to the sampling theorem, can capture fast modulations up to 15 Hz. An example of such fast auroral modulation is the internal modulation of PsAs (Hosokawa et al., 2020). The internal modulation is a temporal modulation in brightness at a few Hz seen during the brighter time of PsAs. Test observations of the internal modulation of PsAs with the Sony α7SIII will evaluate to what extent an optical measurement with commercial digital cameras can be used for capturing sub-second rapid variations of faint auroras.

Figure 4.13 shows the time series of the reconstructed RGB values when the Sony α7SIII observed a PsA on 28th February 2023. Panel (a) is a time series at a single pixel, and the error bars are given by the standard deviation determined by the fitting curves in Figure 4.5. In all RGB channels, the large error bars make it difficult to detect the characteristic temporal variations of the PsA. Panel (b) shows the averaged time series among 34^2 pixels where a standard deviation was decreased to 1/10. The main pulsation, periodicities of a few to a few tens of seconds, was clearly captured in all RGB channels. Panel (c) is an enlarged image of the area indicated by the black vertical dashed lines in panel (b). As indicated by the black arrows, brightness modulation at several Hz was

visualized in the blue and red channels but not in the green channel.

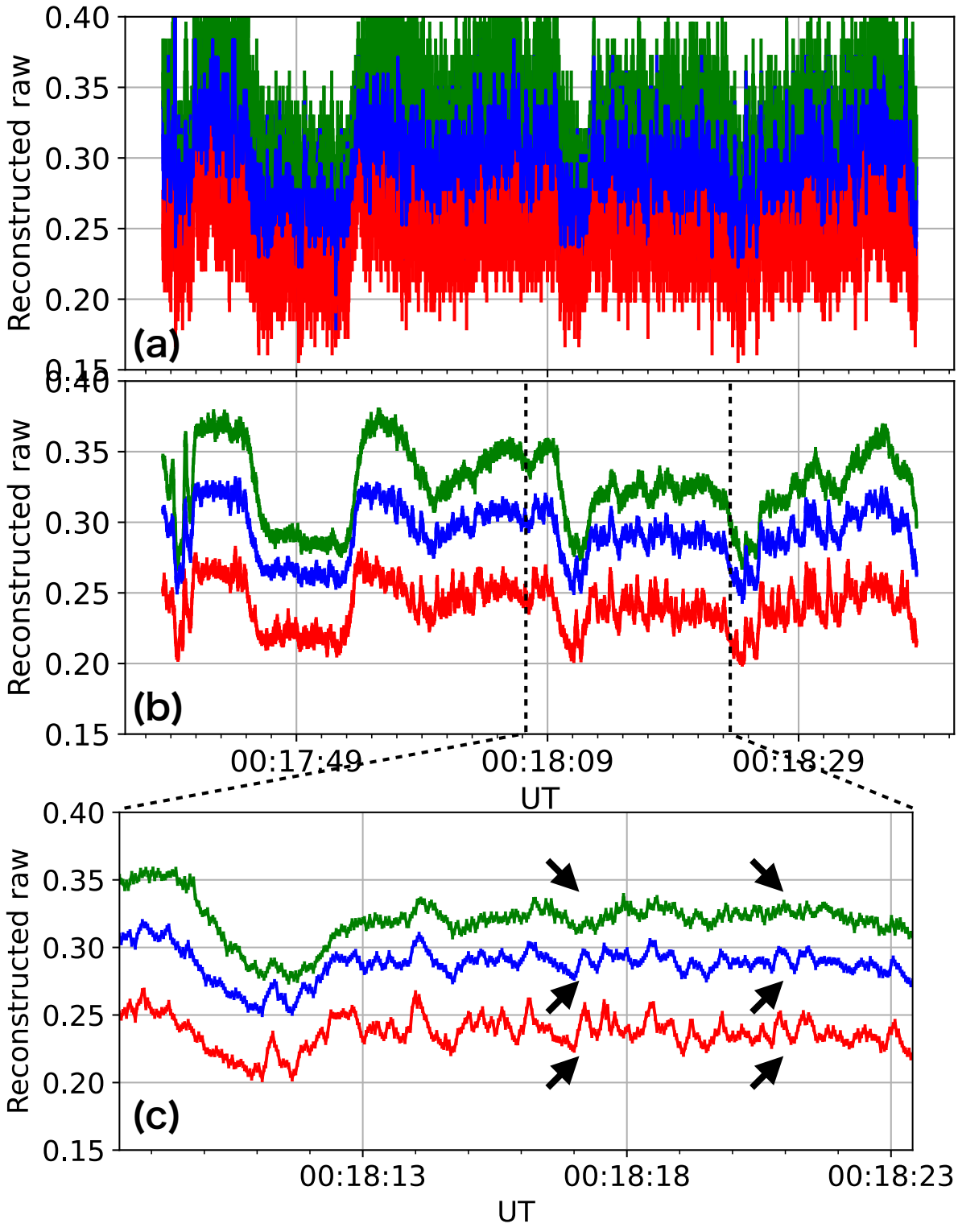

Figure 4.13: (a) The time-series of the intensity of the PsA derived for one pixel of images from the Sony α7SIII. (b) Same as the panel (a), but derived by averaging the values in 34^2 pixels. (c) The close-up view of the dashed interval in panel (b).

The less distinct internal modulation in the green channel may be because the green channel is sensitive to the emission at 557.7 nm, which has a finite lifetime, i.e., delay time before producing emission, from the excited state. Figure 4.7 shows that the green channel is most sensitive to emissions at around 550 nm. This means the green channel responds strongly to the 557.7 nm emission, which has an average relaxation time of 0.7 s. In contrast, the blue channel is hardly sensitive to the emission at 557.7 nm and, instead, it represents the band emission of the nitrogen at around 400–440 nm. The red channel is also sensitive to 557.7 nm, but it may respond effectively to the band emission of nitrogen molecules. Observing internal modulation at 557.7 nm is difficult because the relaxation time of 0.7 s is long compared to the periodicity of the internal modulation at $\sim$0.3 s. In particular, as documented by Kawamura et al. (2020), the relaxation time is distributed in a wide range from 0.5 to 1 s, and such scattering would smear out the sub-second modulation of PsAs. Therefore, observing the internal modulation in the green channel is difficult compared to the other channels. In conclusion, the Sony α7SIII can detect the internal modulation of PsAs, at least in the R and B channels, both of which represent prompt emissions of nitrogen molecules. In Chapter 5, we will discuss what can be inferred from capturing the internal modulation of PsAs on the ground.

4.5 Summary

The deep learning model was used to automatically detect the direction of aurora appearance for the first time in the history of aurora observations from the ground. Controlling the gimbal enabled pointing the camera in the direction of auroras adaptively. Further, the picture profile S-Log3 allowed quantitative measurements of auroral brightness in the video recordings at 30 FPS. The use of S-Log3 solved the problem of conventional commercial cameras being unable to evaluate the intensity of auroras quantitatively and allowed us to confirm that quantitative video recording is possible even with commercial digital cameras. This means that commercial digital cameras can be regarded as proper high-speed cameras that can observe auroras at a sampling rate of 30 Hz. In the actual observations, we visualized the fast propagation of the shock aurora and the internal modulation, which is the sub-second temporal variation of PsAs. Although the shock aurora

appears only in a limited region for a short period, we tracked its propagation with a higher spatial resolution than ordinary all-sky cameras by controlling the angle of view using a combination of the gimbal and deep learning model. The internal modulation was seen only in the R and B channels, and the results of optical calibration experiments suggested that these channels were responding to the prompt emission. It was also shown that the difficulty in seeing the internal modulation in the G channel may be due to the widely distributed lifetime of the green line, which is 0.5–1.0 sec. These observations indicate that commercial digital cameras have a temporal resolution comparable to ordinary high-speed cameras, and when mounted on a gimbal, they can provide higher spatial resolution than all-sky cameras. Here, it should be borne in mind that, because of the heavy weight of expensive cameras, it is difficult to mount them on a gimbal and change the angle of view. In Chapter 5, we analyze a conjugate observation of the internal modulation of PsAs by a ground-based high-speed camera and the Arase satellite to verify how the ability to observe the internal modulations of PsAs can contribute to a better understanding of the magnetospheric dynamics and wave-particle interactions in the magnetosphere.

Chapter 5

Scientific Values of Detecting the Internal Modulation in PsAs

5.1 Introduction

In Chapter 4, it was shown that commercial digital cameras can detect the internal modulation of PsAs. Chapter 5 discusses the scientific value of observing the internal modulation by analyzing an event where ground-based high-speed cameras and the Arase satellite observed the PsAs. Here, note that the high-speed cameras employed for this observation are not commercial digital cameras but dedicated high-speed cameras for scientific optical imaging.

PsA is known to show several periodicities, but the ones often discussed are the main pulsation, whose period ranges from a few to a few tens of seconds (Yamamoto, 1988), and the internal modulation, whose frequency ranges from 2 to 4 Hz (Nishiyama et al., 2014). These two types of fluctuations have a hierarchical structure. The bright and dark periods of the main pulsation are called the ON and OFF phases, respectively, and the internal modulation is embedded in the ON phase. However, PsAs are not always accompanied by internal modulation; for example, Royrvik and Davis (1977) reported that approximately more than 50% of PsAs in the midnight and morning sectors show signatures of internal modulation from the narrow field-of-view (FoV) television data.

The driver of PsA has been considered the wave-particle interaction between chorus waves and electrons in the vicinity of the equatorial plane in the magnetosphere. For a long time, it has been pointed out that there is a similarity in the periodicity of chorus waves

and PsAs from ground-based observations (e.g., Tagirov, 1993). A conjugate observation of the Time History of Events and Macroscale Interactions during Substorms (THEMIS) satellite and the ground-based camera revealed the one-to-one correspondence between the periodicity of the chorus waves in the magnetosphere and the main pulsation of PsA (Nishimura et al., 2010). From this observational result, Nishimura et al. (2010) predicted that the cyclotron resonance between electrons and chorus waves causes the precipitation of PsA electrons into the ionosphere. According to Kennel and Petschek (1966), the resonance energy E_R of an electron interacting with a whistler mode wave with frequency ω is calculated by the following theoretical equation:

$$E_R = \frac{B^2}{2\mu_0 N}\frac{\Omega_{ce}}{\omega}\left(1 - \frac{\omega}{\Omega_{ce}}\right)^3 \tag{5.1}$$

where B, μ_0, N, and Ω_{ce} are the background magnetic field intensity, vacuum permeability, electron density, and electron cyclotron angular frequency, respectively. Since the frequency of chorus waves typically ranges from several hundred to a few thousand Hz, assuming $B = 100$ nT and $N = 2$ /cc, the resonance energy is from several hundred to a few tens of keV. This value is consistent with the energy band of PsA electrons detected at low altitudes by satellite and rocket observations (Nishiyama et al., 2011; Sandahl et al., 1980; Miyoshi et al., 2020). In addition, Jaynes et al. (2013) demonstrated that the ON and OFF phases of PsA correlate with an increase and decrease in the flux of a few tens of keV electrons by examining the observation from the geostationary orbit satellite. More recently, the wave and electron measurements by the Arase satellite verified the prediction of Nishimura et al. (2010) and Miyoshi et al. (2015b) by observing that the loss cone was filled through the pitch-angle scattering driven by the chorus wave (Kasahara et al., 2018a). Furthermore, conjugate observations with a ground-based high-speed all-sky camera and the wave measurements by the Arase satellite have shown that the periodicity of the internal modulation shows one-to-one correspondence with that of the chorus elements (Hosokawa et al., 2020). These results are consistent with the model of Miyoshi et al. (2015b), which proposed that chorus bursts cause the main modulation of PsA and the internal modulation of PsA is caused by the rising tone elements embedded in the chorus bursts. According to Hosokawa et al. (2020), the internal modulation is visualized when the chorus elements are well-grown and discrete, while that is invisible when the element structure is unclear, which is called the hiss-like emission.

A computer simulation by Katoh et al. (2018) suggested that parameters such as the density and temperature anisotropy of hot electrons are important for enhancing chorus elements. An injection of electrons with a disturbance such as a substorm often makes the higher temperature anisotropy in the inner magnetosphere. In such a situation, the linear growth rate ω_i, expressed by the following equation, increases (Kennel and Petschek, 1966).

$$\omega_i = \pi|\Omega_{ce}|\left(1-\frac{\omega}{|\Omega_{ce}|}\right)^2 \eta(V_R)\left[A(V_R)-\frac{1}{|\Omega_{ce}|/\omega-1}\right] \tag{5.2}$$

Here V_R is the resonance velocity. $\eta(V_R)$ and $A(V_R)$ are expressed as follows:

$$\eta(V_R) = 2\pi\frac{|\Omega_e|-\omega}{k}\int_0^\infty v_\perp dv_\perp F\Big|_{v_\perp, v_\parallel = V_R}, \tag{5.3}$$

$$A(V_R) = \frac{\int_0^\infty v_\perp dv_\perp \left(v_\parallel \frac{\partial F}{\partial v_\perp} - v_\perp \frac{\partial F}{\partial v_\parallel}\right)\frac{v_\perp}{v_\parallel}}{2\int_0^\infty v_\perp dv_\perp F}\Bigg|_{v_\parallel = V_R}. \tag{5.4}$$

$\eta(V_R)$ can be interpreted as the fraction of the total electron distribution that satisfies the resonance condition and depends on the density of hot electrons. $A(V_R)$ is a measure of the pitch angle anisotropy. Thus, in Equation (5.2), an increase in the density of hot electrons and the electron temperature anisotropy causes an increase in the linear growth rate.

Coherent waves increase their amplitude following the linear growth rate. According to the nonlinear growth theory of whistler mode waves by Omura (2021), their amplitude is strengthened nonlinearly once the amplitude exceeds "threshold amplitude." The wave in the beginning phase of the nonlinear growth is called the triggering wave. Sometimes, the triggering wave is formed with an increase (rising tone) and decrease (falling tone) of frequency (Hikishima et al., 2009; Omura, 2021), and these are the chorus elements. The normalized threshold amplitude is expressed as follows:

$$\tilde{\Omega_{th}} = \frac{100\pi^3\gamma^4\xi}{\omega\omega_{ph}^4(\chi\tilde{U}_{\perp 0})^5}\left(\frac{\tilde{a}s_2\tilde{U}_{t\parallel}}{Q}\right)^2 \exp\left(\frac{\gamma^2\tilde{V}_R^2}{\tilde{U}_{t\parallel}^2}\right) \tag{5.5}$$

where the parameter ω_{ph} is the plasma frequency of hot electrons given by $\omega_{ph}^2 = N_h e^2/(m_0\epsilon_0)$ and N_h is the density of hot electrons. $U_{\perp 0}$ is the average momentum perpendicular to the magnetic field, and $U_{t\parallel}$ is the parallel component of the thermal momentum. γ is the

Lorentz factor, and ξ and χ are dimensionless coefficients for describing the dispersion relation. For more details and other parameters, see Omura (2021). ω_{ph} depends on the density of hot electrons, and the threshold amplitude becomes small, i.e., the chorus is more easily excited when the density of hot electrons increases. The threshold amplitude also becomes smaller when only the perpendicular component of the momentum increases, i.e., when the temperature anisotropy is enhanced. Katoh et al. (2018) has shown that chorus elements are more likely to grow when the temperature anisotropy of injected electrons and the ratio of the hot electron density to the cold electron density are high.

The parameters such as the temperature anisotropy and the density of hot electrons may cause the difference between chorus waves with the discrete elements and hiss-like chorus waves. Thus far, however, such a relationship has not yet been confirmed by actual observation. In this Chapter, we investigate the parameters that affect the presence or absence of the internal modulation of PsA by analyzing a conjugate observation event of PsAs by the high-speed all-sky cameras and the Arase satellite. During this event, the PsA showed little internal modulation in the first half. However, internal modulations were frequently observed in the second half. We also evaluate the condition required to detect internal modulation from the ground and discuss the meaning of detecting internal modulation of PsA in the dynamics of the inner magnetosphere.

5.2 Instruments

5.2.1 EMCCD all-sky imagers

For the optical observation of PsA, we used electron-multiplying CCD (EMCCD) all-sky cameras installed at Sodankylä (67.37°N, 26.63°E) in Finland and Tjautjas (67.28°N, 20.72°E) in Sweden, as described in Hosokawa et al. (2023). The all-sky cameras capture auroral images with 256 × 256 pixels at a sampling rate of 100 Hz. Both cameras used a BG3 optical filter (Samara et al., 2012) to exclude the bright forbidden lines, for example, at 557.7 nm and 630.0 nm; thus, they can be more sensitive to prompt emissions, for example, radiating from nitrogen molecules and molecular nitrogen ions. Note that the raw count recorded in 16 bits cannot be converted to the Rayleigh value since the BG3 filter covers multiple emission lines. The locations of the cameras and their field-of-view

(FoV) at an altitude of 100 km with an elevation angle of 20 degrees are drawn by solid black lines in Figure 5.1. For the camera in Sodankylä, FoVs with elevation angles of 10 and 15 degrees are also drawn with gray dotted lines.

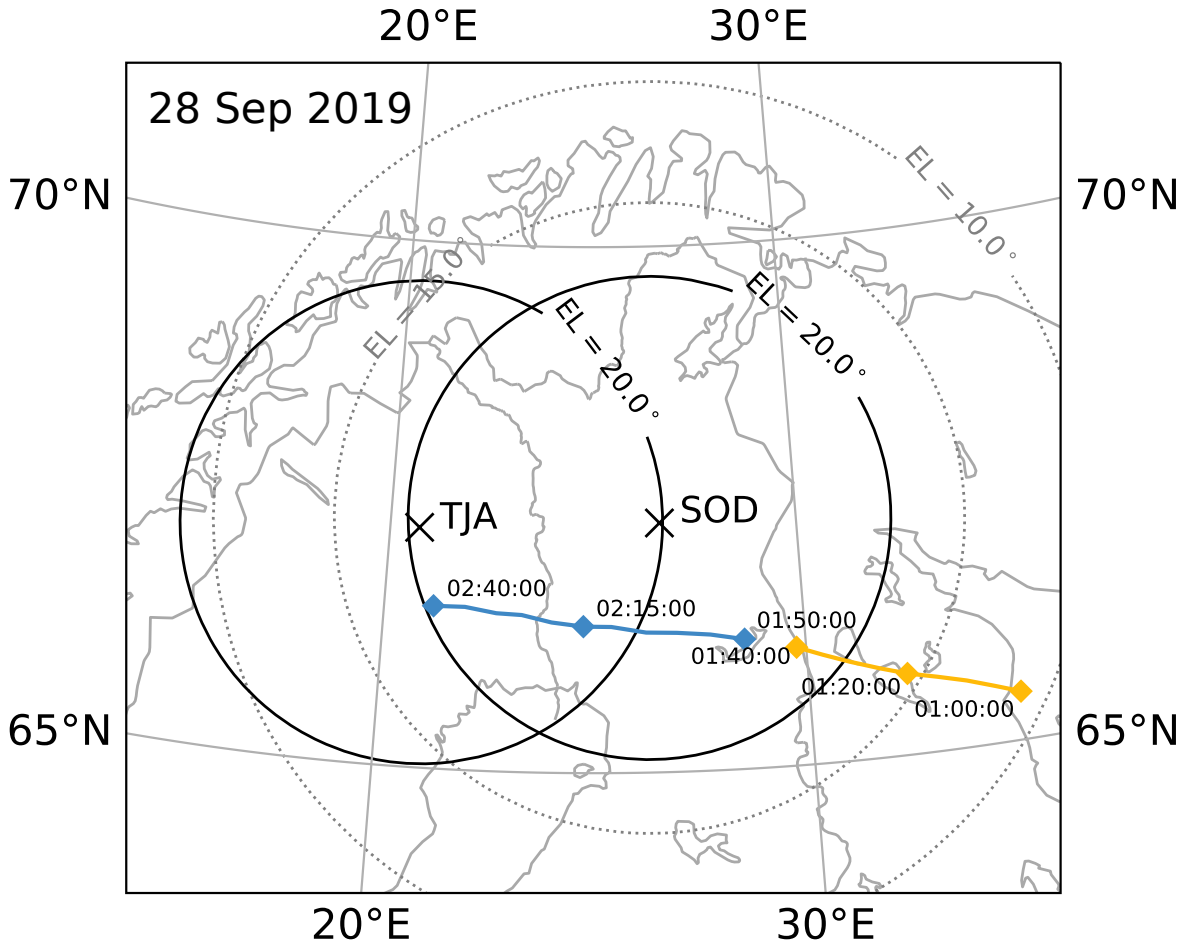

Figure 5.1: Locations and fields of view (FoVs) of the ground-based cameras and the footprint of the Arase satellite projected using the TS05 model (Tsyganenko and Sitnov, 2005). The FoVs are projected to an altitude of 100 km. The black contour lines show the FoVs calculated using an elevation angle of 20 degrees. The gray contour lines show those of the camera at Sodankylä calculated by elevation angles of 15 degrees and 10 degrees. The satellite's footprint is colored in yellow and blue for periods A and B, respectively. UTs on 28 September 2019 are labeled every 25 minutes.

5.2.2 The Arase satellite

The instruments onboard the Arase satellite (Miyoshi et al., 2018) used for comparison with the ground-based optical observation are introduced separately. The conjugate points (magnetic footprints) of the Arase satellite estimated by the semi-empirical model (Tsyganenko and Sitnov, 2005) are shown by yellow and blue lines in Figure 5.1. The universal time (UT) is labeled every 25 minutes starting at 01:00 UT. During this event, the Arase satellite was in the morning side where PsA was most clearly observed. The chorus wave, generated through the wave-particle interaction, is most frequently observed near the magnetic equatorial plane (Tsurutani and Smith, 1974, 1977). Thus, it is favorable for this study since the magnetic latitude (MLAT) value of the satellite's location was close to 0.

Plasma Wave Experiment (PWE)

The PWE is an instrument for measuring the DC electric field and plasma waves, covering the range from DC to 10 MHz for electric fields and from a few Hz to 100 kHz for magnetic fields (Kasahara et al., 2018c). The PWE consists of several instruments, but only the onboard frequency analyzer (OFA) and waveform capture (WFC) were used in this study (Matsuda et al., 2018). OFA provides frequency-time diagrams of electromagnetic fields with a time cadence of 1 second, while WFC provides waveforms of electromagnetic fields with a sampling rate of 65 kHz for a limited time interval (typically 8–64 seconds). Data from OFA and WFC were used to evaluate the presence or absence of the chorus waves and discrete chorus elements, respectively.

Low-Energy Particle Experiments - Electron Analyzer (LEP-e)

The LEP-e is an instrument for obtaining three-dimensional (3D) fluxes of low-energy electrons, covering from 19 eV to 19 keV in 32 steps by the electrostatic analysis (Kazama et al., 2017). The relative energy resolution $\Delta K/\langle K \rangle$ is 9.2%. The sensors mounted in 16 directions are rotated by the spin of the satellite body and cover all solid angles. Data is sampled in 16 spin phases per rotation. The 3D flux is obtained with a time resolution of 8 seconds, and angular resolution (full width at half maximum: FWHM) is 2.89 and

21.5 degrees in the elevational/azimuthal angles, respectively. In this study, we used the omnidirectional and 3D flux to investigate how the distribution of electrons changed during the event.

Medium-Energy Particle Experiments - Electron Analyzer (MEP-e)

The MEP-e is an instrument for obtaining the 3D flux of medium-energy electrons, covering from 10 keV to 80 keV in 16 steps by electrostatic analysis (Kasahara et al., 2018b). The energy resolution $\Delta K/\langle K \rangle$ is 8.0%. The sensors mounted in 16 directions cover all solid angles by rotation, as in LEP-e, but MEP-e has 32 spin phases. The 3D flux is obtained with the same time resolution of 8 seconds as LEP-e, and the angular resolution (FWHM) is 3.5 degrees in the azimuthal angle. The omnidirectional flux and the 3D flux were used for the same purpose as LEP-e.

Magnetic Field Experiment (MGF)

The MGF is a fluxgate magnetometer that samples 256 vectors per second (Matsuoka et al., 2018). In this study, the background magnetic field vectors were used to calculate the pitch angles of the electrons. We also used the background magnetic field intensity to calculate the electron cyclotron frequency.

5.3 Results

5.3.1 Background conditions

This study analyzed PsA that appeared after midnight on 28th September 2019. Figure 5.2 shows the background conditions for several days, including the interval of the event. The top panel shows the SYM-H index (Iyemori and Rao, 1996) for six days. The black dotted lines roughly mark the optical observation period by the EMCCD cameras. The top panel shows that a typical magnetic storm had occurred over several days, beginning on the 27th. An initial phase started in the morning of the 27th, followed by the main phase that continued until immediately before midnight on the 28th, the SYM-H reaching -60 nT. After that, a recovery phase continued for several days, even after the end of the

event. The interval of current interest between the dotted lines corresponds to the main and early recovery phases of this magnetic storm.

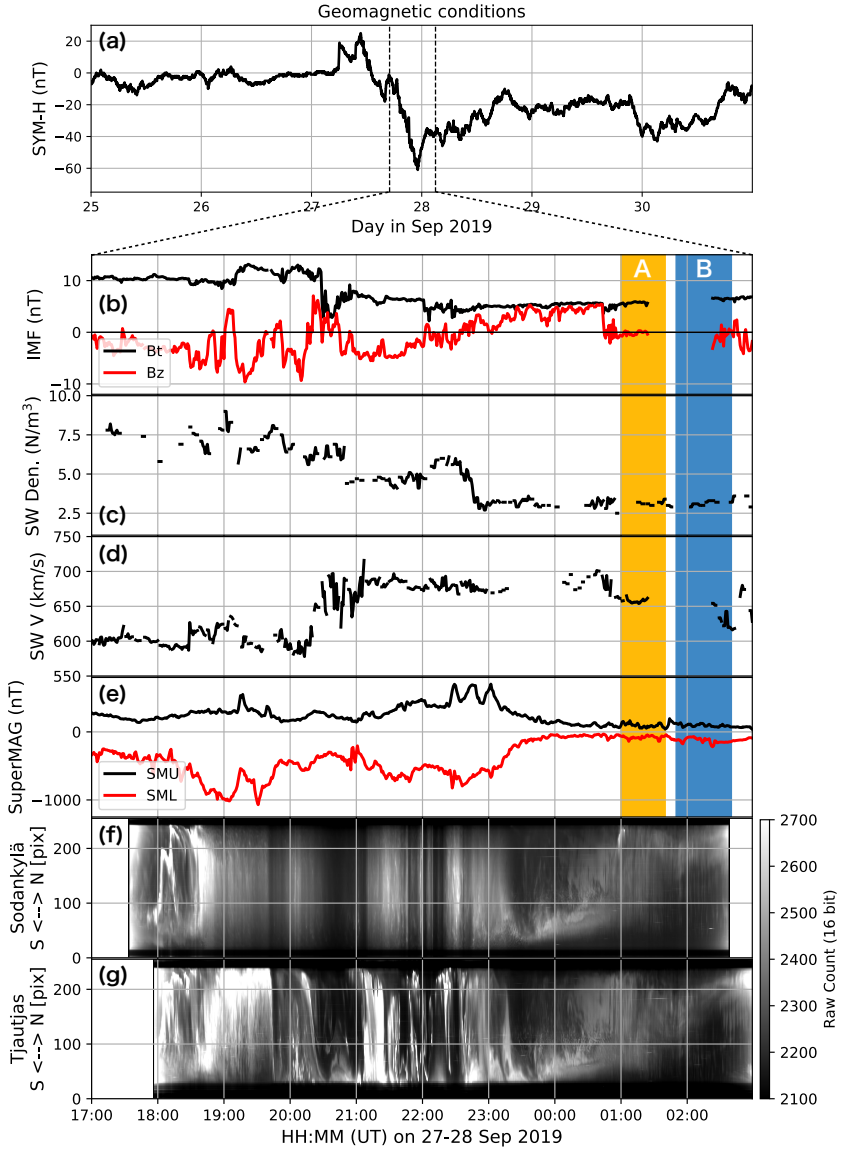

Figure 5.2: Background geomagnetic conditions during the event. (a) SYM-H index for six days, including the event on 28 September 2019. Two black dotted lines roughly mark the start and end times of the optical observation. Intensity (black) and z-component (red) of the interplanetary magnetic field (b), solar wind density (c), solar wind speed (d), SuperMAG upper (black)/lower (red) (e) from 17:00 UT on 27 September to 03:00 UT on 28 September. Periods A and B are hatched in yellow and blue, respectively. (f) The north–south keogram at Sodankylä. (g) The north–south keogram at Tjautjas.

The second to last panels of Figure 5.2 summarize the solar wind parameters, geomagnetic indices, and optical observations from dusk on the 27th to dawn on the 28th. Period A, where little internal modulation was observed, and Period B, where much internal modulation was observed, are hatched in yellow and blue, respectively (see Section 5.3.2 for details). The panels show the interplanetary magnetic field (black: intensity, red: z component), solar wind plasma density, solar wind speed, SuperMAG indices (Newell and Gjerloev, 2011; Gjerloev, 2012) (black: SuperMAG Upper (SMU), red: SuperMAG Lower (SML)), and so-called keograms which are the time-series of a north-south cross-section of the all-sky images, obtained at Sodankylä and Tjautjas. The z component of the interplanetary magnetic field was negative for many hours from 17:00 to 22:00 UT, sometimes reaching -10 nT. The SMU/SML shows strong substorms occurred several times before 23:00 UT. Although data have some gaps, the solar wind speed was high throughout the night, especially after 21:00 UT, which increased to 650–700 km/s. Sodankylä was cloudy from 19:00 UT until 23:00 UT, but several intense discrete auroras appeared until 23:00 UT at both locations. The video from the EMCCD cameras is also available as supporting information in the electric version of this paper. During the following hours, no significant disturbances in the SuperMAG indices were detected; however, PsA was observed continuously until dawn.

5.3.2 Optical signature of PsA

Figure 5.3 shows four keograms for representative 5-minute intervals during Periods A and B from the observatories. The panels from top to bottom are Period A from Sodankylä (SOD-A), Period A from Tjautjas (TJA-A), Period B from Sodankylä (SOD-B), and Period B from Tjautjas (TJA-B). The ticks on the horizontal axis are given every 10 seconds. Although Sodankylä and Tjautjas are distant, separated by $\sim$250 km in the longitudinal direction, typical main pulsations with a period of several to a few tens of seconds were observed from both the stations in Period A. In the panels SOD-A and TJA-A, most ON phases did not have a temporal fluctuation of less than one second within themselves; i.e., internal modulation rarely occurred. This can be seen more clearly in the video attached as Supporting Information. However, some ON phases, e.g., 66.5°N at 01:19–01:20 UT in TJA-A (indicated by the white arrow), showed tiny fluctuations,

and these may be the internal modulation. Meanwhile, in Period B, there were many tiny fluctuations within at least a few seconds compared to Period A. The white arrows indicate several examples of this fluctuation in the panels. Besides, the average size of PsA patches was smaller in the latitudinal direction during Period B compared to Period A. There are differences in the morphology of the PsA between Periods A and B. Importantly, fine-scale modulation is observed in Period A, whereas many tiny modulations are detected in Period B.

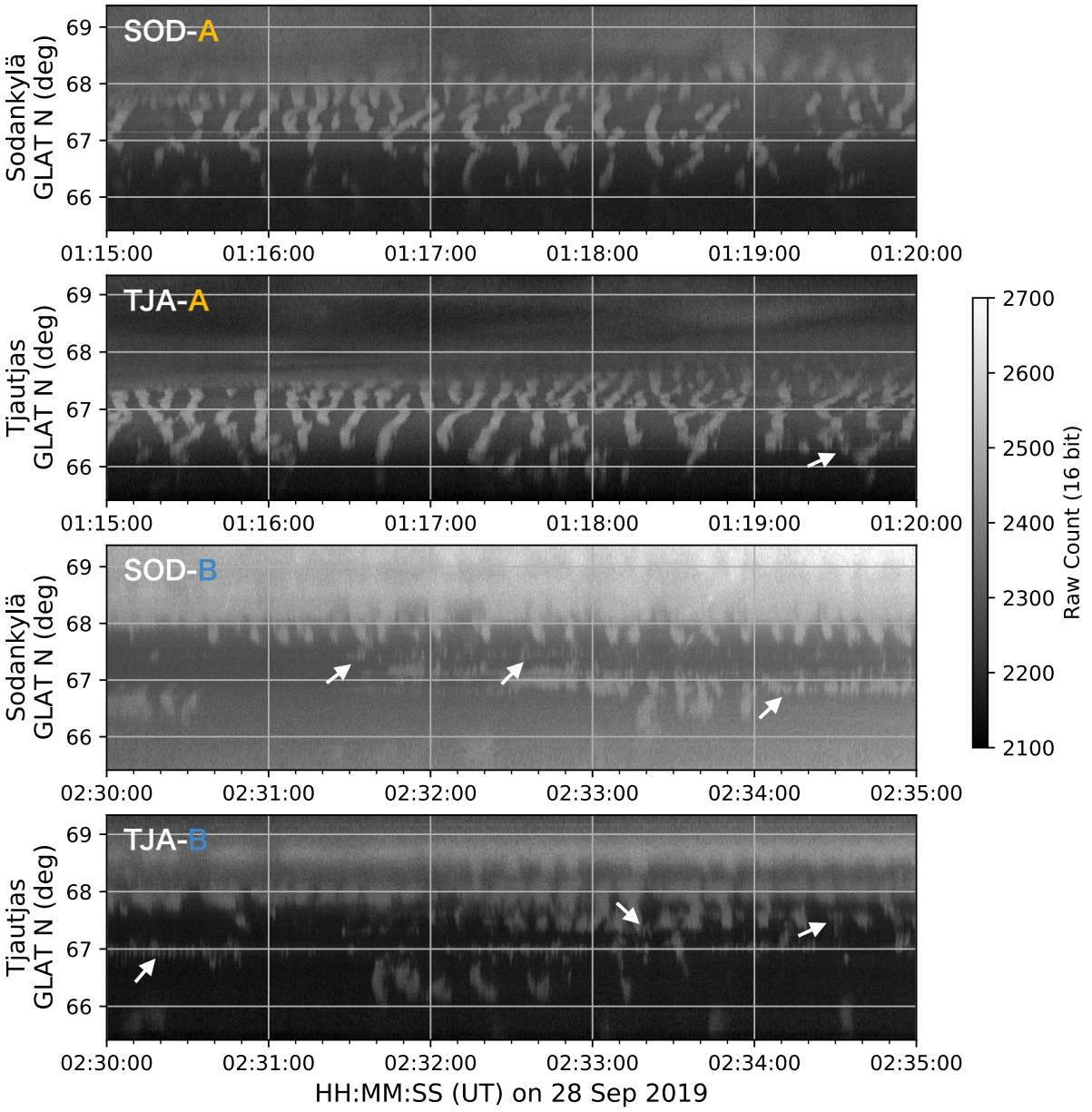

Figure 5.3: The north–south keograms at Sodankylä and Tjautjas at periods A and B. From top to bottom: Sodankylä at period A (SOD-A) and Tjautjas at period A (TJA-A), and Sodankylä at period B (SOD-B), and Tjautjas at period B (TJA-B). The original sampling rate of 100 Hz was downsampled to 10 Hz. Note that the background in SOD-B is generally brighter due to the contamination of sunlight. White arrows indicate examples of tiny modulation.

To investigate when these fine-scale modulations appeared frequently, we applied a

frequency analysis to the data acquired by the two cameras from 01:00 to 02:30 UT. Two procedures were performed before the fast Fourier transform (FFT) to improve the SNR of the data: the temporal resolution was reduced from 0.01 s to 0.1 s by averaging 10 consecutive images, and images were spatially smoothed with a 4×4 median filter. Now, the data size from each camera is 256×256×54000 for 90 minutes. In other words, we have 256×256×2 time series with a length of 54000. Of the 256×256×2 1D time series obtained by the above procedure, the coordinates with elevation angles greater than 20 degrees were used for the analysis. The 90-minute time series was divided every 2 minutes, and then FFT was applied, i.e., 45 times FFT was performed for each coordinate. After the FFT, we calculated the sum of the amplitudes from 2 to 40 seconds and from 2 to 4 Hz and defined these as the main pulsation component and the internal modulation component, respectively. Figure 5.4 shows the time series of the sum of each component in the pixel where the elevation angle was greater than 20 degrees. The upper and lower panels are the main pulsation and internal modulation components. The time series from the cameras in Sodankylä and Tjautjas are plotted in each panel. By referring to the movie, we considered each component zero with a threshold in the pixel where the aurora did not appear for 2 minutes. We excluded these from the time series in Figure 5.4. Due to the sunlight, the internal modulation component at the eastern edge of the FoV became significantly larger after 02:20 UT (hatched in panels). We set a threshold to exclude it as much as possible but could not completely remove it. In the main pulsation component in Figure 5.4 (upper panel), the intensity maxima were at around 01:15 and 01:35, reaching a minimum at 01:40 UT. The aurora appeared very little from 01:38 to 01:43 UT. After 01:45 UT, the intensity increased or decreased in a few minutes compared to the interval before 01:40 UT. The internal modulation component (lower panel) showed a remarkable change, with the component becoming several to ten times larger after 01:46 UT, while the main pulsation component was $\sim$1.5–3.0$\times10^9$ throughout the event. After 01:46 UT, intensity fluctuations at intervals of a few minutes were observed, which generally corresponded to the main pulsation component in peak-to-peak. This correlation would be reasonable since internal modulation is generally embedded in the main pulsation. Based on these characteristics, we defined Period A as 01:00–01:40 UT and Period B as 01:50–02:40 UT.

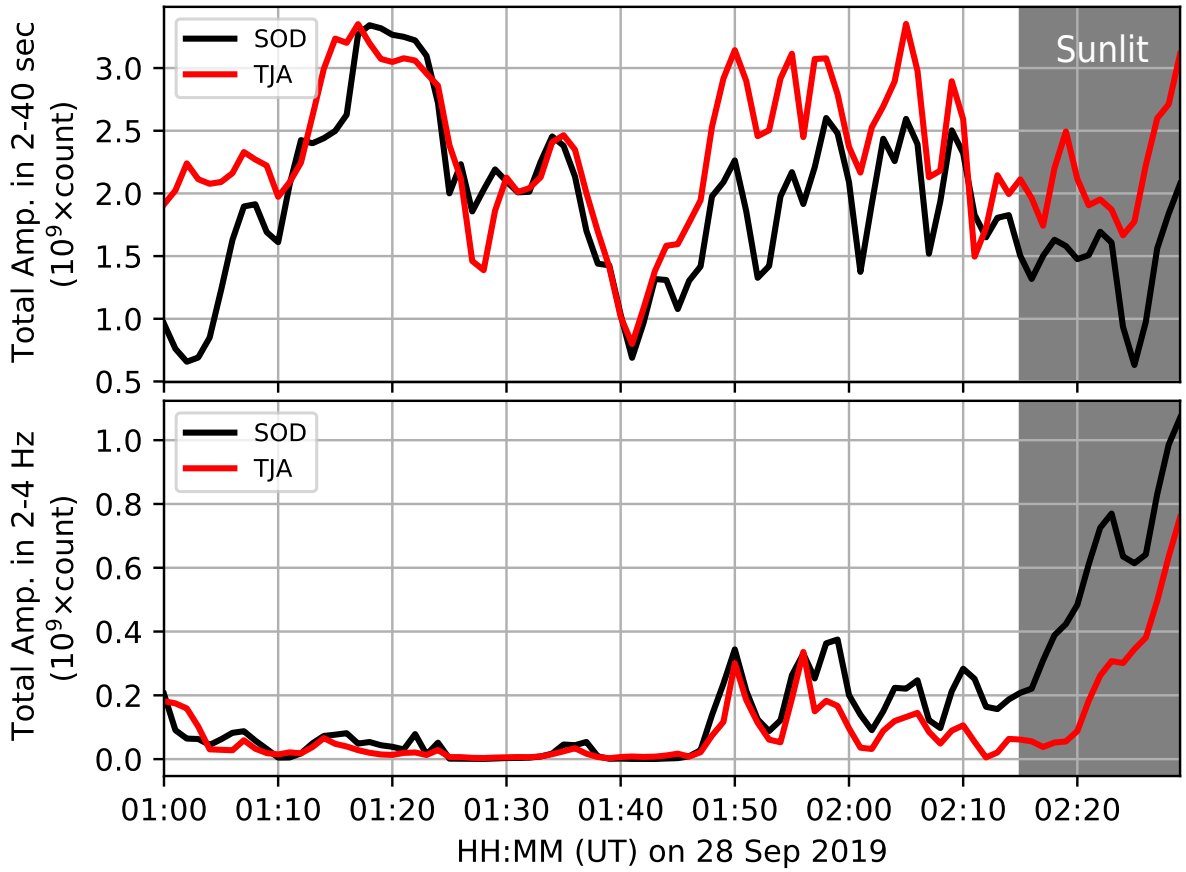

Figure 5.4: Temporal variation of the total amplitude of the main pulsation (upper panel) and internal modulation (lower panel). The time-series data from the cameras in Sodankylä and Tjautjas were taken every 2 minutes. The sum of the amplitudes for 2–40 s and for 2–4 Hz, obtained by performing a Fast Fourier Transform, is represented as the main pulsation component and the internal modulation component, respectively. The time series represents the sum of the main pulsation and the internal modulation components at pixels where aurora was observed for two minutes at an elevation angle of at least 20 degrees. The hatched interval is affected by the sunlight.

Figures 5.3 and 5.4 demonstrate the temporal difference in the frequency of internal modulation. To investigate its spatial difference, we conducted an additional frequency analysis. As in Figure 5.4, the 100 Hz time-series data were down-sampled to 10 Hz, and a 4×4 median filter was applied. The pre-processed 1D time-series signal was sampled in 30 minutes for both periods (A: 01:10–01:40 and B: 01:50–02:20) and input to the FFT. The

difference between Figure 5.4 and the present analysis is the length of the time series used for FFT; a 2-minute time series was used in Figure 5.4, whereas a 30-minute time series was used this time. From the obtained spectra, the amplitudes of the main pulsation (2–40 s) and the internal modulation (2–4 Hz) were integrated. Then, the integrated spectra were normalized to evaluate the spatial difference in the occurrence frequency of main pulsation and internal modulation in Periods A and B. The normalization was performed using different values for the main pulsation and internal modulation components; however, we used the same values for each component through Periods A and B. Figure 5.5 shows the intensity maps of the main pulsation and internal modulation components in Periods A and B. The left panels show the main pulsation component in Period A (MAIN-A) and the internal modulation component in Period A (INTR-A). Those for Period B are shown on the right panels. The main pulsating component was consistently strong in Periods A and B in 66–68°N. A comparison of the panels MAIN-A and MAIN-B revealed that the intensified region varied within the FoV of the camera in Tjautjas (west side). In Period A, the intensity was higher east of 20°E. However, in Period B, the intensity increased over a broader range of longitudes. Inside the FoV of the camera in Sodankylä, there was no temporal change in the high-intensity region, and the intensity generally weakened in Period B. This trend is consistent with the decrease in the SOD value in the upper panel of Figure 5.4.

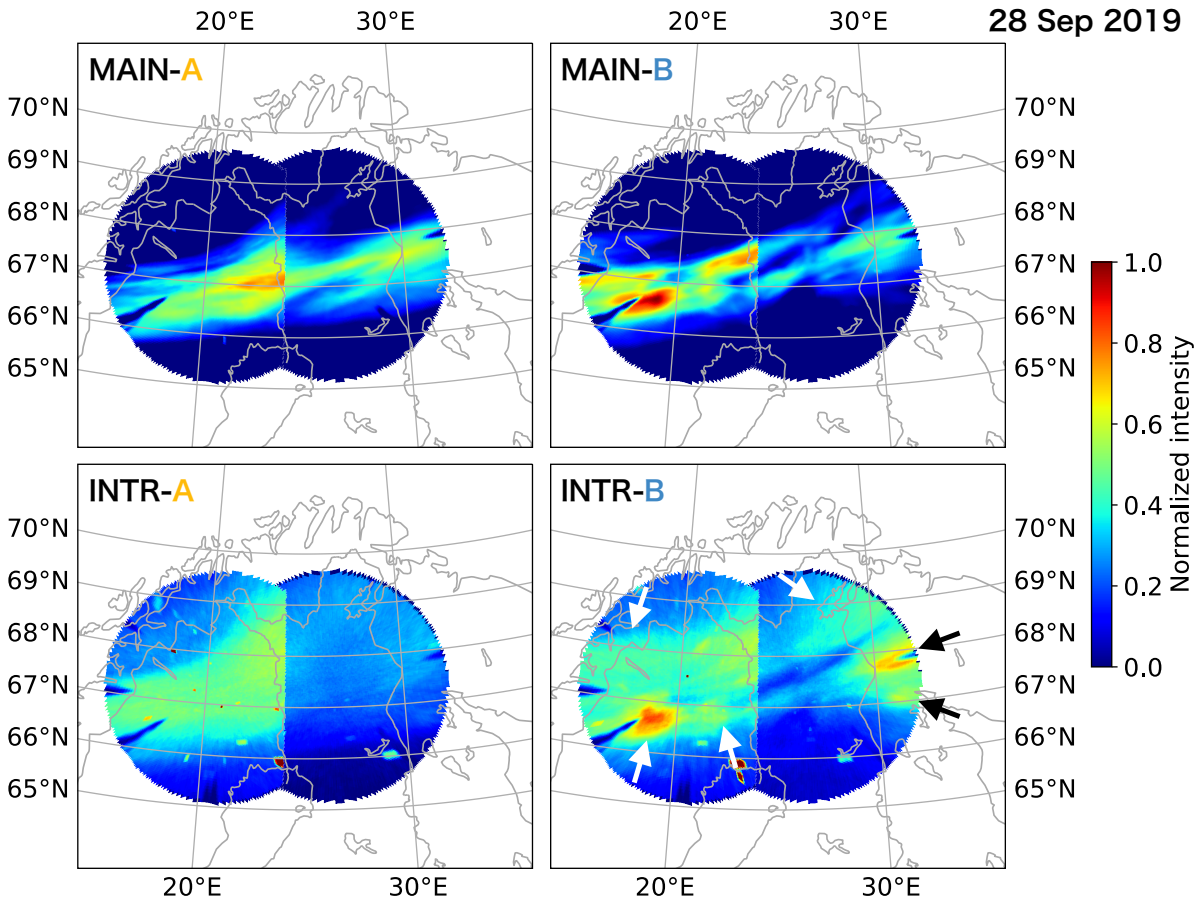

Figure 5.5: Intensity maps of the main pulsation (2–40 sec, top) and the internal modulation (2–4 Hz, bottom) components of the FFT spectrum for periods A (left) and B (right). The components in each frequency range were normalized using common values for the two top and bottom panels. Data from Sodankylä and Tjautjas were plotted for regions with longitude greater than 24°E and less than 24°E, respectively.

The intensified areas of the internal modulation component did not necessarily coincide with areas where the main pulsation component was stronger. In particular, there was no intensity difference above 69°N where PsA was rarely seen and 67°N where the main pulsation component was enhanced, indicating that little internal modulation occurred in the FoV of the camera in Sodankylä. In the FoV of the camera in Tjautjas, the internal modulation component was intensified in the region where the main pulsation component was strong. However, there was no longitudinal difference in intensity east of 20°E, which was observed for the main pulsation component. A comparison of the panels INTR-A and

INTR-B revealed that the internal modulation component was generally high in both the FoVs, as indicated by the black and white arrows in panel INTR-B. In particular, there are two spot-like intensifications in the regions of 66.5°N/19°E and 68°N/31°E, where PsA patches with internal modulation were observed for a long time in Period B. In conclusion, the increase in the internal modulation component observed in Period B is not due to the contribution of a narrow region but a change that occurred over a wide area within the two FoVs.

5.3.3 Comparison of the optical signature with in-situ observation by Arase

As already shown in Figure 5.1, we conducted a conjugate observation of ground-based cameras in Lapland and the Arase satellite in the magnetosphere. The results of the wave and particle observations by the Arase satellite during Periods A and B are shown in Figure 5.6. The panels show, from top to bottom, the electric and magnetic field components of waves detected by PWE/OFA, the omnidirectional flux of electrons from the MEP-e and LEP-e, the differential energy flux inside the loss cone (within a pitch angle of 4 degrees) from the MEP-e, and a north-south keogram sampled along a meridian including the instantaneous magnetic footprints of the satellite. The white line in the bottom panel indicates the magnetic footprints calculated by the semi-empirical model (Tsyganenko and Sitnov, 2005). The vertical white dotted lines mark 01:40 and 01:50 UT, giving the transition timing between Periods A and B. The horizontal axis shows not only the UT but also the magnetic local time (MLT), MLAT, and radial distance at the location of the satellite. In this event, MLAT is close to 0, meaning the Arase satellite was near the magnetic equator. Therefore, we used the magnetic field intensity measured by MGF to calculate the cyclotron frequency of electrons f_{ce}.

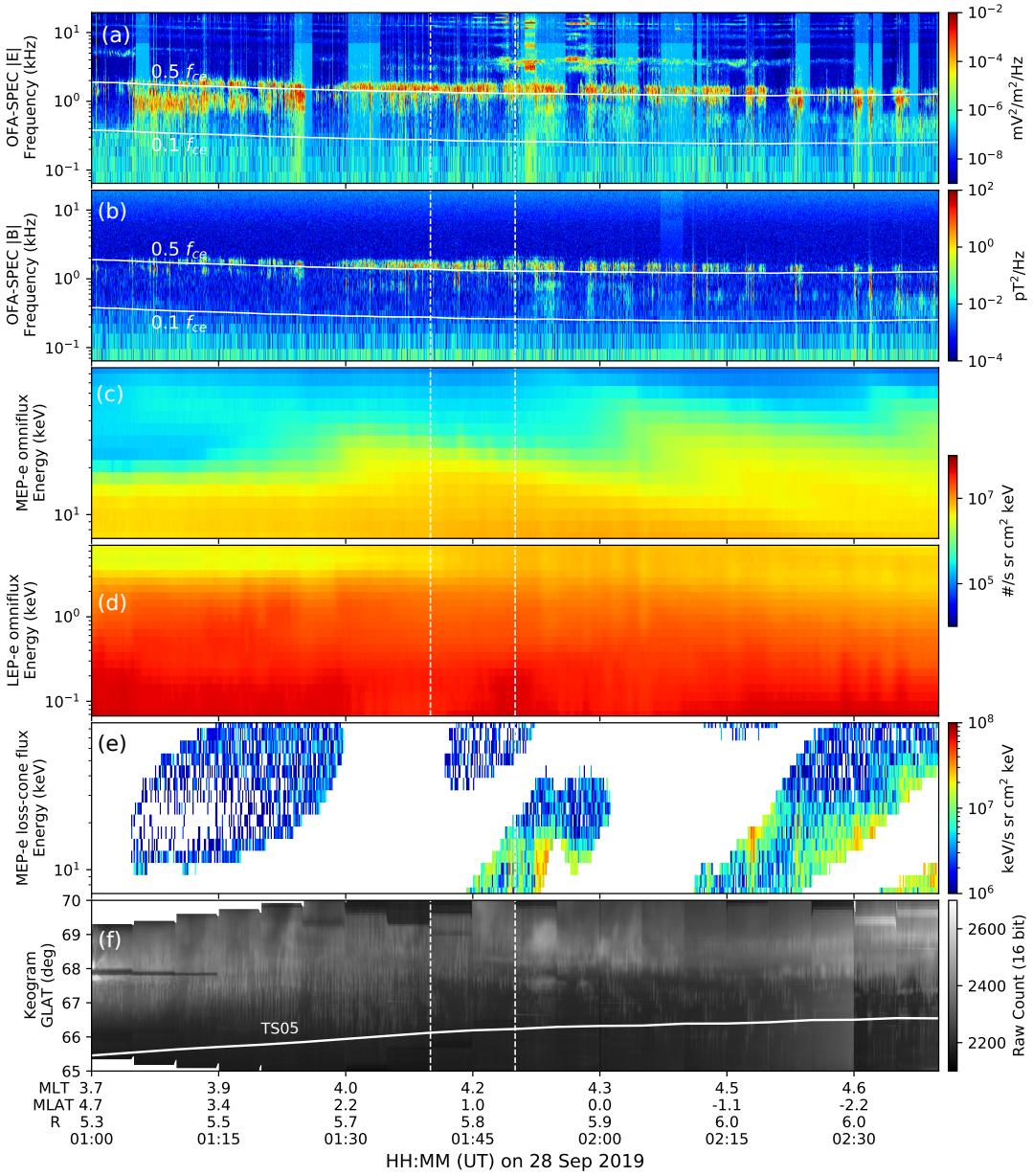

Figure 5.6: Comparison of wave and particle observations by the Arase satellite with ground-based optical observations. (a–b) electric and magnetic field strength by PWE/OFA, (c) unidirectional electron number flux by MEP-e, (d) unidirectional electron number flux by LEP-e, (e) electron energy flux inside the loss cone (within 4 degrees of pitch angle) by MEP-e, (f) the north–south keogram including the satellite footprint estimated by the TS04 model. The white line in the keogram is the footprint of the satellite. The white areas before 01:20 UT have an elevation angle below 10 degrees.

The first and second panels in Figure 5.6 show that lower band chorus waves in 0.1–0.5 f_{ce} were more prominent from around 01:30 UT. Until 01:30 UT, the magnetic field component of the waves was weak, and it was difficult to see PsA at the satellite's footprint. In this event, the frequency band of the chorus wave gradually decreased, and f_{ce} became smaller at the same time so that the resonance energy calculated from the equation (5.1) was about 5–40 keV in both Periods A and B, assuming the electron density of $N = 2$/cc. The electron density should be calculated by detecting the electron plasma frequency f_{pe} from the High-Frequency Analyzer (HFA) of the PWE (Kumamoto et al., 2018), but it was difficult to trace the upper-hybrid resonance frequency during this time; thus, the electron density could not be derived from the observation. In the third panel, electrons with energies ranging from 10 to 60 keV were injected three times, respectively, at 01:20, 01:50, and 02:30 UT, starting from the highest energy. From the LEP-e observation shown in the fourth panel, such variations were difficult to identify, especially below 1 keV. Although only less than half of the data are shown in the fifth panel due to the non-uniformity of the satellite's spin, there was almost no increase in the loss cone flux above 10 keV from 01:05 to 01:30 UT. By contrast, the flux increased from 01:45 UT in the energy range of 10–40 keV. The energy range of high flux inside the loss cone after 01:45 UT is consistent with the resonance energy estimated from the wave data. An active PsA was observed throughout the entire interval in the bottom panel. Although no clear signature of PsA was observed at the footprint in the early part of Period A, clear vertical stripes, which are indications of PsA, appeared on the footprint from 01:30 UT. In addition, as already seen in Figure 5.3, PsAs were seen continuously over a wide latitudinal area during Period A, whereas those were seen more sporadically during Period B.

5.3.4 Periodicity of the chorus element and electron distribution in the velocity space

In Sections 5.3.2 and 5.3.3, we introduced that PsA patches without internal modulation and sporadic PsA patches with internal modulation were observed frequently in Periods A and B, respectively. Panels (b)–(d) of Figure 5.7 show typical signatures of chorus elements obtained from WFC during these Periods. Panel (a) was obtained when no

chorus wave was detected and is shown for comparison with the other panels. Panels (a) and (b) were observed during Period A, while panels (c) and (d) were observed during Period B. To see how the interaction with electrons enhanced the chorus waves, we plot the phase space density of electrons as panels (e)–(h). The radial direction of the panels is the energy, and the angular direction represents the local pitch angle. The phase space density was calculated using the number flux from LEP-e and MEP-e. The number flux measured for 8 seconds, and the starting time of the measurements is written at the top of panels (e)–(h). In addition, the ratio of panel (e), which was obtained when no chorus waves were detected, to panels (f)–(h) is shown in panels (i)–(k) on a scale of 1/5 to 5 times for demonstrating how the distribution changed during the intervals of the chorus.

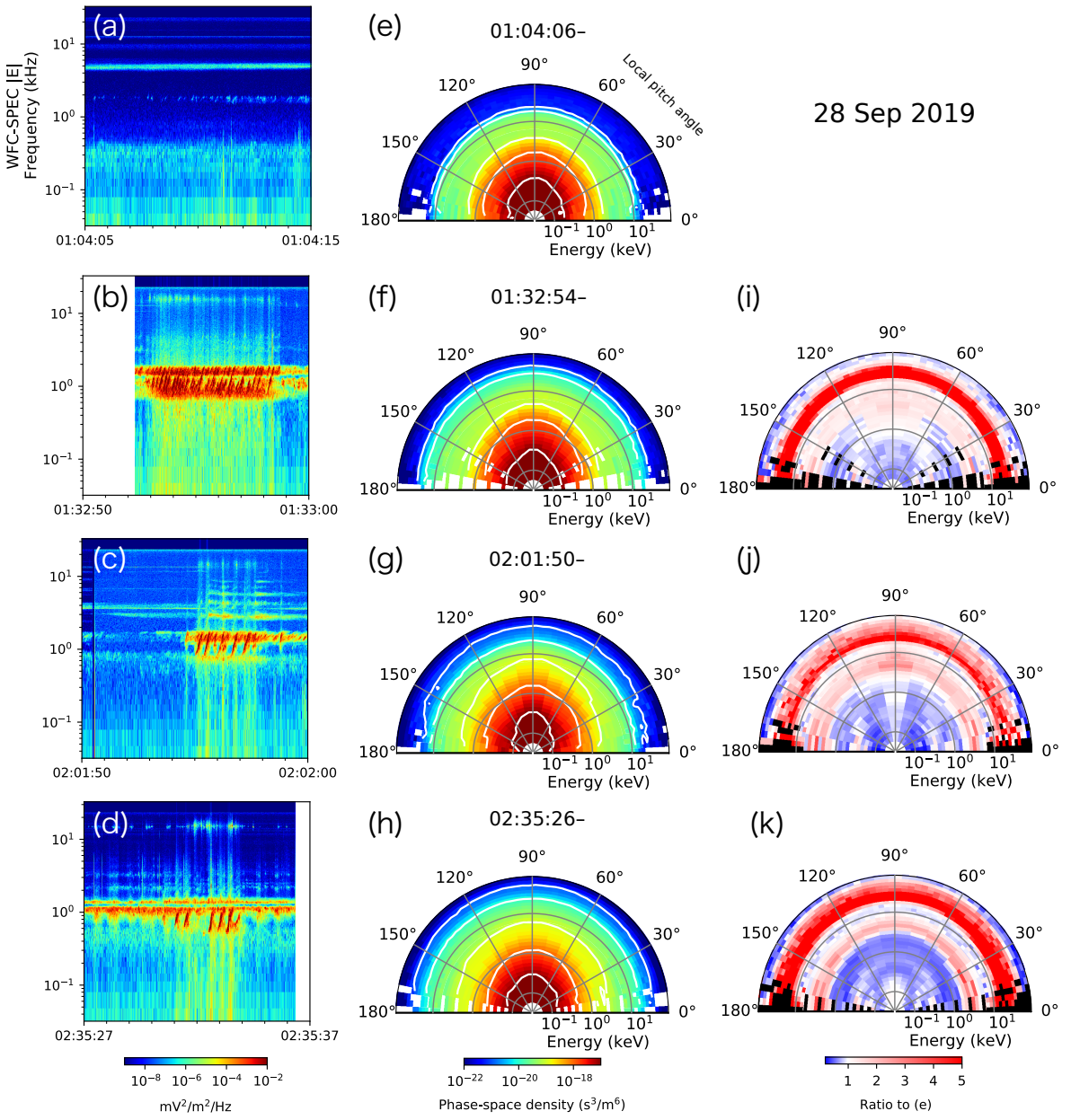

Figure 5.7: Waveforms of chorus elements (panels (a)–(d)) and phase space densities (panels (e)–(h)) observed by WFC and LEP-e/MEP-e, respectively. Measured times of panels (e)–(h) is the closest to those of panels (a)–(d), respectively. In panels (e)–(h), white contour lines are drawn every ten times from 10^{-21} to 10^{-18} s^3/m^6. These panels are obtained for 8 seconds and the starting times of the scan are labeled above. Panels (i)–(k) are the ratios of panels (f)–(h) to panel (e). The red/blue regions have a higher/lower phase space density than panel (e). Bins with no data in panel (e) or (f)–(h) are filled in black in panels (i)–(k).

No chorus waves were observed in panel (a) of Figure 5.7, whereas discrete rising tone elements were observed in panels (b)–(d). The ticks on the horizontal axis in these panels are spaced one second apart. Panel (b) displays approximately six element structures per second, faster than the typical internal modulation repetition period of 2 to 4 Hz. In comparison to panel (b), panels (c) and (d), obtained during Period B, demonstrate a repetition period of the element of approximately 3 Hz, which is similar to the periodicity of the internal modulation. Focusing on the lower limit of the frequency range where the chorus waves occurred ($\sim$700 Hz), there are linear growth phase waves, which are considered to be the triggering waves in panels (b) and (c). In contrast, triggering waves were less evident in panel (d). In panels (i)–(k), the density of electrons with energies above 10 keV increased at all pitch angles. The phase space density in such an energy range increased by a factor of four or more. On the other hand, the number density of electrons below one keV decreased with time, and the phase space density decreased by about 50%. The phase space density at all panels, including panel (e), has a stronger component perpendicular to the magnetic field lines, indicating the temperature has an anisotropy.

In order to infer the factors responsible for the change in the periodicity of the chorus elements between Periods A and B, the density of hot electrons and temperature anisotropy were calculated from the MEP-e data and are shown as Figure 5.8. Here, hot electrons are defined as those measured by the MEP-e (10–80 keV). For these calculations, we used the ERG part_products running on the analysis software "the Space Physics Environment Data Analysis System (SPEDAS) (Angelopoulos et al., 2019)." This program calculates the moment density of hot electrons (top panel) by integrating the 3D phase space density from MEP-e in the energy direction. The temperature components perpendicular and parallel to the magnetic field (middle panel) are derived by the pressure tensor derived from the three-dimensional phase space density. The vertical dotted lines labeled by (a)–(d) correspond to the times when the wave data in panels (a)–(d) in Figure 5.7 were obtained. In the top panel, the partial density of hot electrons increased significantly around 01:20 UT following the first injection, then showed a gradually decreasing trend and increased again around 02:00 UT at the time of the second injection. After 02:20 UT, it decreased again, and following the third injection, it increased again after 02:35

UT. In the middle panel, the temperature component perpendicular to the magnetic field line was dominant throughout the event. The ratio of the perpendicular to the parallel component (temperature anisotropy) in the bottom panel exceeded 1.0 during the entire period. Unlike the density of hot electrons shown in the upper panel, the temperature anisotropy did not change in response to the injections, reached a peak around 02:00 UT, and then decreased monotonically. The density of hot electrons at time (a) was smaller than those at time (b)–(d). At the time (b), we can see little difference in the temperature anisotropy from time (a). However, the density of hot electrons increased by a factor of 1.8 with the first injection. The hot electron density at the time (c) was slightly lower than that in (b) but higher than that in (a), and the anisotropy was largest among (a)–(d). The hot electron density at the time (d) was almost the same as at the time (c), but the temperature anisotropy was the smallest among the four times. Comparing these characteristics with those of the chorus elements shown in Figure 5.7, the density of hot electrons was high at times (b)–(d) when the chorus waves were observed and, more importantly, it was maximum at the time (b) when the element structures appeared most densely. In addition, when the triggering waves were observed, which correspond to times (b) and (c), either the hot electrons or the temperature anisotropy was higher. At the time (d), when both parameters were relatively low, no triggering wave was observed.

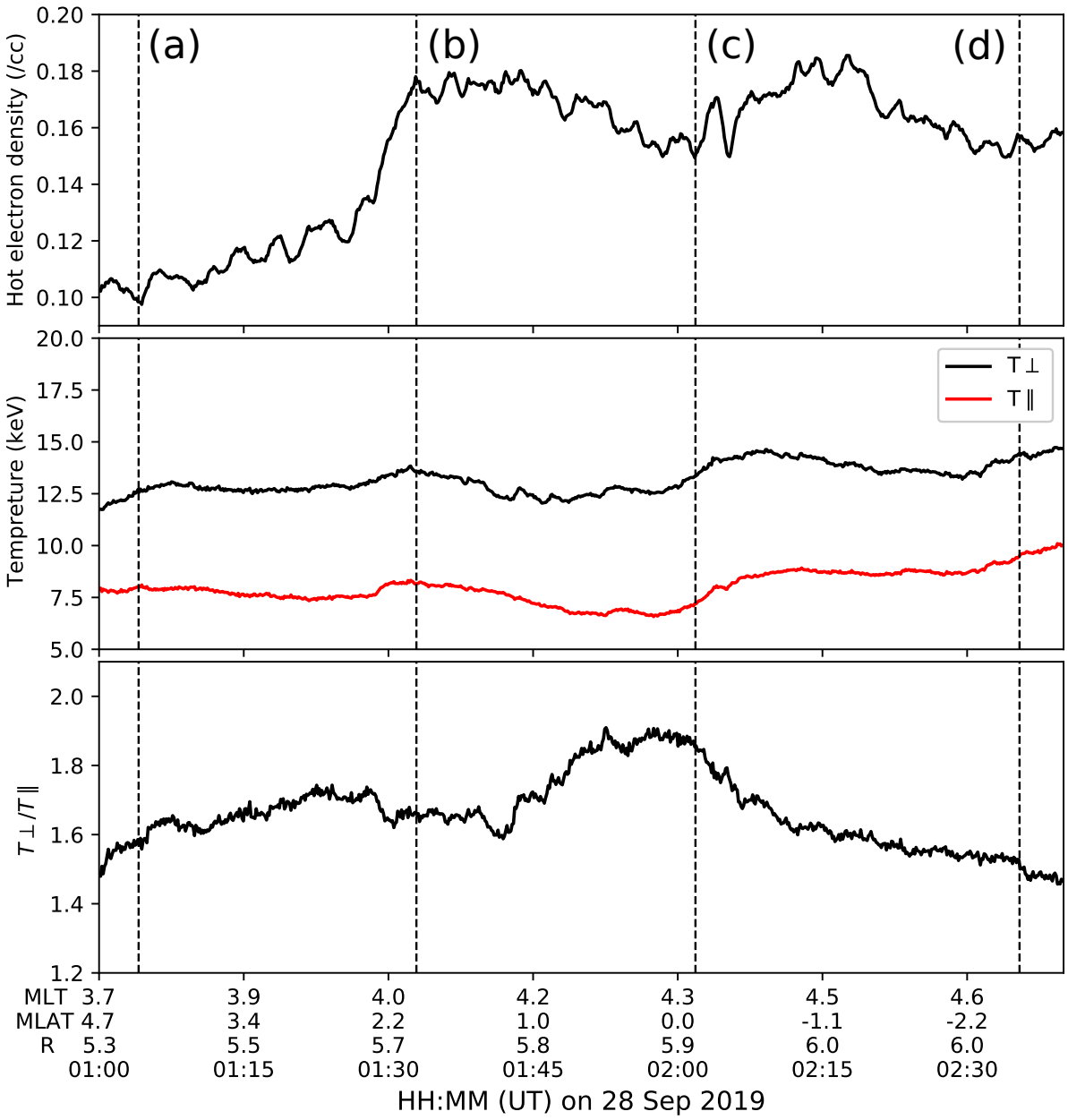

Figure 5.8: The density of hot electrons (top panel), vertical and horizontal components of temperature relative to magnetic field lines (middle panel), and the ratio of vertical and horizontal components (bottom panel) calculated from the MEP-e data using the ERG part_products. The middle panel shows the temperature component multiplied by Boltzmann's constant in units of keV. The time from (a) to (d), indicated by the vertical dotted line, corresponds to the start time of panels (a) to (d) in Figure 5.7.

5.4 Discussion

During the event, many main pulsations without internal modulation were observed in the first half (Period A), and those with internal modulation were frequently observed in the second half (Period B). Since the magnetic footprint of the Arase satellite was within the FoVs of the all-sky cameras during the event, we analyzed the wave and particle data to investigate the factors responsible for the changes in the optical characteristics of the PsA. The results showed that the partial density of hot electrons increased due to the injection when the PsA began to be observed at the footprint (01:30 UT). During Period A, when internal modulation was not evident, the repetition frequency of the chorus element was about 6 Hz, the density of hot electrons was particularly high, and the triggering waves also increased their intensity. In Period B, when internal modulation was observed frequently, the repetition frequency of the chorus element was 3 Hz, close to that of the internal modulation. The density of hot electrons was relatively low compared to Period A. A perpendicular component dominated the electron temperature throughout the event, but the anisotropy gradually decreased in Period B. At the same time, the intensity of the triggering wave weakened.

The reason why the frequency component of the internal modulation increased in Period B shown in Figure 5.4 may be due to a decrease in the linear growth rate and an increase in the threshold amplitude of the chorus wave. As shown in panels (a)–(d) of Figure 5.7, the intensity of the triggering wave weakened with time. It is expected that the intensity of the triggered emission is too low to grow nonlinearity. According to the nonlinear growth theory by Omura (2021), the wave amplitude intensified by the linear growth rate must exceed a threshold amplitude to start the nonlinear growth. The linear growth rate, represented by Equation (5.2), decreases as the hot electron density decreases and the temperature anisotropy is relaxed. The threshold amplitude expressed by Equation (5.5) increases as those values decrease. Thus, nonlinear growth is less likely to occur when the hot electron density decreases or temperature anisotropy is relaxed. From Figure 5.8, both the parameters show a decreasing trend in the second half of Period B (from 02:15 UT), so the triggering wave may have been less prominent than in Period A. As a result, the repetition interval of the chorus elements could have been longer (sparsely

occurring) during Period B and optically visualized as an internal modulation. Katoh et al. (2018) showed in a computer simulation that the chorus is more easily enhanced when the ratio of the hot electron density to the cold electron density and the temperature anisotropy is high. Their result is qualitatively consistent with our observations.

Using the particle-in-cell (PIC) simulation, Lu et al. (2021) investigated how the repetition interval of chorus element changes when anisotropic, high-energy electrons are continuously injected. The results suggest that continuous injection of the anisotropic electron is necessary to produce a repetitive element structure and that the chorus elements are densely generated when the density is high. Our result gives observational evidence for the suggestion from their numerical simulation, as the elements were densely generated when the density of energetic electrons was high and sparsely generated when the density was low. Gao et al. (2022) suggested that the chorus element repetition period T_d is anti-correlated with the drift velocity of energetic electrons V_d as $T_d = 10^{4.905} V_d^{-1.085}$ by conducting a statistical analysis of 1.5 years of the Van Allen Probes data. Their drift velocity V_d is defined by the following formula:

$$\boldsymbol{V_d} = \frac{2E_{\parallel} + E_{\perp}}{qB_0^2} \boldsymbol{B_0} \times \nabla \boldsymbol{B_0}, \tag{5.6}$$

where $E_{\parallel} = \frac{1}{2} m v_{\parallel r}^2$ is the parallel kinetic energy of resonant electrons, and $E_{\perp}$ is the perpendicular kinetic energy. Using the TS05 model (Tsyganenko and Sitnov, 2005), we traced the location of the Arase satellite to the magnetic equator and calculated $\nabla \boldsymbol{B_0}$ to estimate the drift velocity at that location, as introduced in Gao et al. (2022). Since it was difficult to estimate the density of cold electrons from the HFA data, we assumed $n_0 = 2$/cc. To calculate wave angular frequency ω, we used the initial wave frequency f_{pini} of 700 Hz, 700 Hz, and 500 Hz from panels (b), (c), and (d) in Figure 5.7, respectively. The estimated drift velocities were 322 km/s, 245 km/s, and 596 km/s, respectively. By substituting these values into the fitted function, repetition frequencies were 12 Hz, 9 Hz, and 23 Hz, respectively, which are several times higher than the actual repetition frequencies of the elements in panels (b) through (d) of Figure 5.7. We did not derive the anti-correlation between the drift velocity and repetition period of the chorus element either. Note that the ambiguity of the electron density is not significant to derive the drift velocity. Even if the actual value were ten times larger, the velocity would change less than 1 m/s. In Figure 2-(b) of Gao et al. (2022), the fitted line is drawn for drift velocities

in the range of 20 km/s to 200 km/s, and the values in this study are outside this range. Their panel also shows several drift velocities above 200 km/s. However, many points are far from the fitted line and could need to be fitted with another curve in this range.

In the computer experiment by Katoh and Omura (2013), the chorus wave was actively generated when the spatial gradient of the background magnetic field intensity was small. Ozaki et al. (2015) observed PsAs and VLF waves simultaneously using a high-speed camera and a loop antenna on the ground. In their event, the repetition of rising-tone elements changed from sparse to dense within 16 minutes. During the event, the magnetic field inhomogeneity calculated by the empirical model decreased monotonically. In this event, however, the spatial gradient of the background magnetic field intensity at the equator traced from the location of the satellite decreased by 5% in Period B compared to Period A (data not shown). Since a decrease in the spatial gradient of the magnetic field intensity might mean that the chorus is more likely to be triggered, our result is inconsistent with the previous studies. The effect of the magnetic field inhomogeneity would be small in our case since the difference in the spatial gradient is 5% between Periods A and B.

Hosokawa et al. (2020) compared optical observations by the EMCCD cameras with the wave observation by the Arase satellite and showed that the element structure in chorus bursts corresponds to the main pulsation with internal modulation. They also demonstrated that chorus waves without clear element structure correspond to the main pulsation without internal modulation. They suggested that the hiss-like emission, where no element structure is present, is observed because the element structures occur too densely. We observed densely generated chorus elements, as shown in panel (b) of Figure 5.7 when most of the main pulsation did not have internal modulation. The repetition frequency at this time was about 6 Hz, higher than the typical internal modulation frequency of 3±1 Hz. In such a case, due to the dispersion in the time-of-flight of precipitating electrons, the corresponding variation (6 Hz periodicity in this case) cannot be identified as optical variations of PsA seen from the ground. Miyoshi et al. (2015b) conducted a computer simulation of wave-particle interactions to model PsA. They showed that the repetition interval of chorus elements changes the internal modulation of precipitating electrons. They also demonstrated that although numerous chorus elements

exhibit short-term periodicity, they do not generate comparable periodic precipitations due to the time-of-flight of precipitation.

PsA lasts 1–3 hours on average (Jones et al., 2011; Partamies et al., 2017; Bland et al., 2019) and can be observed continuously for up to 15 hours over a wide area during a magnetic storm (Jones et al., 2013). However, their characteristics, such as morphology, periodicity, and energy of precipitating electrons, are not always the same in all regions (Grono and Donovan, 2018; Tesema et al., 2020; Nanjo et al., 2021). The spatial dependence of the presence or absence of internal modulation needs to be understood more. In this event, the internal modulation became more frequent after the second particle injection. By this timing, the transient increase in the hot electron density due to the injection had peaked. Then, it had already begun to decrease. The temperature anisotropy also decreased in the later part of Period B. This suggests that internal modulation may be more frequently observed when anisotropic high-energy electrons are injected and then the anisotropy is relaxed. If this hypothesis is correct, the presence of internal modulation in PsA, manifested as discrete elements of chorus rising tone, suggests that hot electron density and temperature anisotropy become suitable values to detect individual rising tones. Furthermore, the internal modulation may be less visible for PsA intervals immediately after the substorm onset. At the onset of a substorm, the inhomogeneity of the magnetic field is reduced around the equator due to the rapid compression of the magnetosphere. Although the inhomogeneity did not change significantly in our case, the previous studies suggest that the chorus wave is enhanced when inhomogeneity is reduced (Katoh and Omura, 2013; Ozaki et al., 2015). Thus, this effect may also make internal modulations less visible just after the onset.

5.5 Summary

We investigated PsA, showing a difference in the occurrence frequency of the internal modulations, which was observed simultaneously with ground-based high-speed all-sky cameras and the Arase satellite near the magnetic equatorial plane. By analyzing the wave and particle observations from the satellite, we discussed the parameters that determine the presence or absence of internal modulation. The results are summarized as follows:

1. When a PsA without internal modulation became visible at the magnetic footprint of the satellite, the partial density of hot electrons increased by a factor of 1.8.

2. When the internal modulation was less evident, the chorus element was repeated at a high frequency of 6 Hz. When the internal modulation was clearly detected, the repetition frequency of chorus elements was around 3 Hz, which is close to the frequency of the internal modulation.

3. The temperature of the magnetospheric electrons continuously showed a larger perpendicular component. However, the anisotropy started decreasing when the internal modulation began to be observed more frequently.

4. As both the hot electron density and temperature anisotropy began to decrease, the intensity of the triggering wave decreased, making it harder to generate dense ($\sim$6 Hz) chorus elements.

Based on these observation results, when both the density and the temperature anisotropy of hot electrons are high, chorus elements can be densely generated; thus, many main pulsations without internal modulation should be observed. The internal modulation would be easily observed when both parameters show a decreasing trend. Therefore, many internal modulations may suggest that a certain time has passed since the particle injection, and then the density and temperature anisotropy of hot electrons decrease in the magnetosphere. The ground-based optical observations introduced in this chapter were not made by commercial digital cameras. As described in Chapter 4, however, commercial digital cameras can detect the internal modulation of PsA. Combining the results shown in Chapters 4 and 5, we imply the feasibility of imaging the plasma environment in the magnetosphere using commercial digital cameras.

Chapter 6

Conclusion

The most important findings of this thesis, from an experimental point of view, are that 1) the count values in the B and G channels of a commercial digital camera linearly correlate with the absolute optical intensity values in Rayleigh at 427.8 nm and 557.7 nm of a dedicated scientific instrument, and 2) commercial digital cameras can observe rapid motion of auroras such as shock aurora and the internal modulations of PsAs. Finding 1) confirms the feasibility of estimating the average energy of auroral electrons with commercial digital cameras quantitatively. Finding 2) suggests the possibility of visualizing the propagation of incoming energy from the solar wind to the magnetosphere and diagnosing the characteristics of magnetospheric electrons (density of energetic electrons and temperature anisotropy) with commercial digital cameras. These findings further expand the use of observation data from digital cameras, which have, thus far, provided only geographic location and gradual behavior of auroral phenomena. Much data from commercial digital cameras has been uploaded to social media. Scientists can utilize such data in their research if they use them appropriately by understanding the pros and cons of commercial digital camera observations. In the following, we summarize the results of each chapter, including the points described above, and discuss future prospects.

In Chapter 2, we investigated the two cases of PsAs observed from the ISS using a commercial digital camera, the Nikon D5, to evaluate the feasibility of deriving the periodicity of PsA and the energy of PsA electrons from commercial digital cameras. We succeeded in extracting the period of the main pulsation of PsA in a wide area and found that the periodicities of PsA do not depend on the large-scale structure of the magnetosphere-

ionosphere coupling system, such as the length of the local magnetic field lines. This indicates that the period of the main pulsation is determined by local parameters in the source region of chorus waves in the magnetosphere. The analyses of the ratio of counts from the B and G channels of the digital camera suggest that the average energy of precipitating electrons is higher on the morning side, which is consistent with several previous studies on the energy of PsA electrons. The average energy was estimated using the assumption that the intensity in the B channel would correspond to the band emission of nitrogen molecules, manifesting precipitations of relatively higher energy electrons, while that in the G channel to the green-line emission, representing precipitations of moderately energetic electrons. Based on this assumption, it was demonstrated that using the B/G ratio from the ISS enabled us to derive a map of the energy of PsA electrons in a wide area. At the same time, however, it was recognized that further validation in comparison with dedicated scientific instruments is required before using the B/G ratio as a proxy for the energy of PsA electrons.

In Chapter 3, to quantitatively investigate the validity of the assumption employed in Chapter 2, we installed the Nikon D5, the same camera and lens onboard the ISS, in Tromsø, Norway. We conducted simultaneous observations of auroras with the photometer in the same location. The results suggest that the Rayleigh value, an absolute optical intensity, at 427.8 nm and the raw counts in the B channel, and the Rayleigh value at 557.7 nm and the raw counts in the G channel showed positive linear correlation within a standard deviation of the count values. This indicates that the assumption made in Chapter 2 is plausible, confirming that the count values from the commercial digital camera and the corresponding B/G values can be used to quantitatively estimate the energy of precipitating auroral electrons. We developed a deep-learning model to detect the auroral appearance in real-time for efficient observations with the digital camera in Tromsø. Then, we implemented it into the system to capture images automatically only when the aurora appears. Besides the observations, a website was constructed to notify the auroral appearances automatically. This web system is the only operational image classification method that runs on real-time image data, which supports photographers, tourists, and other citizen scientists in quickly realizing photograph timing.

In Chapter 4, we captured videos of auroras in Kiruna, Sweden, to investigate to what

extent, especially how accurately, video data from commercial digital cameras can be used to study the fast-moving or quickly varying behavior of auroras. We have developed and operated an adaptive observation system that automatically identifies the direction of the aurora using a deep learning model, points the camera toward that direction by controlling the gimbal, and then takes images as a video at 30 frames per second. This chapter includes two case studies obtained from this observation system. The first target is the shock aurora, and the most crucial part, in terms of evaluating the performance of the instrument, is that we were able to detect and observe the rapid motion of the shock aurora as designed, which occurs in a narrow region and decays in about 10 minutes. Using the data from the video, several scientific findings were obtained regarding the propagation characteristics of shock aurora toward the nightside. The second target is the internal modulation of PsAs. Even though fast modulation of the aurora was mostly observed with expensive high-sensitivity cameras dedicated to scientific research, we showed that the 3 Hz internal modulation of PsAs can be detected even by the commercial digital camera with the results of the optical calibration experiment. These findings through the test measurements confirm that data from commercial digital cameras can be used to capture dynamically moving characteristics and sub-second rapid modulations of auroras.

In Chapter 5, we analyzed a case of simultaneous observation of PsAs using a high-sensitivity camera and the magnetospheric satellite Arase to examine the significance of observing the sub-second internal modulation on the ground. In this event, the internal modulation was barely visible when the PsA started to appear, and a few tens of minutes later, it became visible over the wide part of northern Scandinavia. In the wave observation by Arase in this event, the chorus elements were densely generated when the internal modulation was not visible, and they were sparsely generated when the internal modulation was visible. The particle data were also examined since the density and temperature anisotropy of hot electrons must increase to generate the waves. The results showed that the internal modulation was clearly observed when the density and temperature anisotropy of hot electrons, which had been increased by the particle injection, decreased. This indicates that observing the internal modulation of PsAs on the ground helps infer the conditions of electrons in the magnetosphere. Our result is a discovery that increases the value of ground-based observations by cameras because the internal

modulation can be visualized even by inexpensive commercial digital cameras, while it is not easy to make multipoint observations of the particles in the magnetosphere.

In Chapter 1, we raised three objectives for this study. These were 1) to verify how reliable auroral photographs and movies taken by commercial digital cameras as a data set for quantitative research of aurora, 2) to know what kind of physical parameter can be estimated from the multi-channel color observations of commercial digital camera, 3) to understand what characteristics of aurora can be captured by commercial digital cameras and how such observations can be used for studying magnetospheric dynamics. The conclusions obtained for the first objective are that RGB values correlate with Rayleigh values within their standard deviations for still images taken with the Nikon D5 and that S-Log3 can be used to reconstruct the linearity to the light intensity from RGB values in the videos taken with the Sony α7SIII. For the second objective, it was shown that the G and B count values obtained from Nikon D5 correlate with the 557.7 nm and 427.8 nm emission intensities of auroras. This result suggests that the B/G ratio may be an indicator of the average energy of the auroral electrons. The validity of this suggestion is reinforced by the result that the B/G ratio was larger in the morning sector in the observations from the ISS. The result obtained for objective three is that the video taken by the Sony α7SIII visualized the fine spatiotemporal variations of the shock aurora, which may help understand the spatiotemporal evolution of the SC current system. Another important result is that the Sony α7SIII can visualize the internal modulation of PsA. According to the observation by the Arase satellite, the internal modulation can be an indicator of the threshold amplitude in the magnetosphere. Thus, digital camera observations can be used to estimate variables of the threshold amplitude, such as the density of energetic electrons and temperature anisotropy.

Chapter 7

Future Direction

The most significant remaining task for the future is to verify the accuracy of the B/G ratio as an indicator for estimating the average energy of the precipitating electrons. Unfortunately, the aurora has never appeared during our special radar experiments, and thus, a simultaneous observation of the aurora by the Nikon D5 and EISCAT radar has not yet been made. However, the results of the special experiment conducted by other researchers will be disclosed within one year. During those experiments, as simultaneous observations might be established with the appearance of auroras, we can compare the B/G ratio and the average energy estimated from the EISCAT radar measurement. In addition, we need to verify the accuracy of the RGB values from the videos taken by the Sony α7SIII through close comparison with the ALIS camera in Kiruna. It is unclear whether the results obtained in Tromsø can also be reproduced in Kiruna since the IRF is more affected by city lights than the Ramfjordmoen field station. As described in Chapters 3 and 4, we have developed methods to control camera observations through machine learning, and then the systems worked as designed during actual operations in the field. The author hopes that the developed system for automatic detection of auroral appearances and directions will be used to trigger co-existing ground-based observations in northern Scandinavia, for example, the EISCAT_3D radar, which is the largest phased-array incoherent scatter radar in the world. Such adaptive and unified ground-based measurements with radio and optical instruments will shed new light on the aurora physics in close collaboration with observations with scientific satellites in the magnetosphere.

Here, I would like to give my personal opinion on how I expect future observations of

auroras by commercial digital cameras to advance. One of the unique features of these observations is that a large amount of data is available on social media. Although we may not be able to guarantee a sub-second time accuracy because it cannot synchronize the time with GPS, knowing the presence and form of the aurora allows for many discussions. One of the most frustrating aspects of daily work for me is that interesting phenomena, such as very active magnetic storms and auroral breakups, occur, but the sky above the observatory is too cloudy to get data. If we utilize the data from digital cameras uploaded to social media, instead of sighing deeply while checking the overcast data every morning, we might have a delightful time browsing beautiful videos while sipping coffee.

Commercial digital cameras have the advantage of being small and inexpensive compared to professional cameras while having high sensitivity to visualize the internal modulation. To take advantage of this feature, we can install multiple digital cameras at the same observatory to improve the SNR of the data. This cannot be achieved with professional cameras which have large sizes. In Chapter 4, we introduced a method of tracking the aurora with a wide-angle lens, but sometimes, the aurora appears over a larger area than can be captured by a wide-angle lens. In such cases, the multiple commercial cameras can be mounted in multiple directions to maintain the high spatial resolution of a wide-angle lens and capture auroras over a wide area without missing any parts of the aurora. In addition, the inexpensive and small size of the camera helps to install cameras at many existing observatories. Increasing the number of observation points of Tromsø AI as much as possible and providing citizen scientists with a wide range of real-time information on auroral occurrences would also increase the amount of data uploaded to social media, as mentioned above.

Another advantage of commercial digital cameras is their ability to capture auroras in color. Observing auroras in monochrome makes it difficult for those unaccustomed to aurora observation (including professional researchers) to distinguish between clouds and auroras in the captured data. Therefore, in situations where the presence or absence of auroras is crucial, such as in Tromsø AI, observing them in color is important. Moreover, if commercial digital cameras can be installed in various locations, it will be possible to create a wide-area map of the average energy of auroral electrons, as the color can estimate their average energy. Achieving this could allow commercial digital cameras to

contribute to space weather forecasting, for instance, by identifying the local time sections most likely to observe killer electrons that could destroy satellites.

Publications

Publications Related to the Thesis

1. Nanjo, S., Hozumi, Y., Hosokawa, K., Kataoka, R., Miyoshi, Y., & Oyama, S.-i. (2020). Fine-scale visualization of aurora in a wide area using color digital camera images from the International Space Station. *Journal of Geophysical Research: Space Physics*, 125, e2019JA027729. https://doi.org/10.1029/2019JA027729

2. Nanjo, S., Hozumi, Y., Hosokawa, K., Kataoka, R., Miyoshi, Y., Oyama, S.-i., et al. (2021). Periodicities and colors of pulsating auroras: DSLR camera observations from the International Space Station. *Journal of Geophysical Research: Space Physics*, 126, e2021JA029564. https://doi.org/10.1029/2021JA029564

3. Nanjo, S., Nozawa, S., Yamamoto, M. et al. An automated auroral detection system using deep learning: real-time operation in Tromsø, Norway. *Scientific Reports 12*, 8038 (2022). https://doi.org/10.1038/s41598-022-11686-8

4. Nanjo, S., Ebukuro, S., Nakamura, S., Miyoshi, Y., Kurita, S., Oyama, S.-I., et al. (2023). An implication of detecting the internal modulation in a pulsating aurora: A conjugate observation by the Arase satellite and all-sky imagers. *Journal of Geophysical Research: Space Physics*, 128, e2023JA031499. https://doi.org/10.1029/2023JA031499

5. Nanjo, S., Yamauchi, M., Johnsen, M. G., Yokoyama, Y., & Brändström, U. (2023). Propagation and development of a shock aurora toward the late evening sector observed on 26 February 2023. *Earth, Planets and Space*, Under review

References

Adachi, K., Nozawa, S., Ogawa, Y., Brekke, A., Hall, C., and Fujii, R. (2017). Evaluation of a method to derive ionospheric conductivities using two auroral emissions (428 and 630 nm) measured with a photometer at Tromsø (69.6°N). *Earth, Planets and Space*, 69(1):90.

Akasofu, S.-I. (1965). Dynamic morphology of auroras. *Space Science Reviews*, 4(4):498–540.

Akasofu, S. I. (1976). Recent progress in studies of dmsp auroral photographs. *Space Science Reviews*, 19(2):169–215.

Alken, P., Thébault, E., Beggan, C. D., Amit, H., Aubert, J., Baerenzung, J., Bondar, T. N., Brown, W. J., Califf, S., Chambodut, A., Chulliat, A., Cox, G. A., Finlay, C. C., Fournier, A., Gillet, N., Grayver, A., Hammer, M. D., Holschneider, M., Huder, L., Hulot, G., Jager, T., Kloss, C., Korte, M., Kuang, W., Kuvshinov, A., Langlais, B., Léger, J.-M., Lesur, V., Livermore, P. W., Lowes, F. J., Macmillan, S., Magnes, W., Mandea, M., Marsal, S., Matzka, J., Metman, M. C., Minami, T., Morschhauser, A., Mound, J. E., Nair, M., Nakano, S., Olsen, N., Pavón-Carrasco, F. J., Petrov, V. G., Ropp, G., Rother, M., Sabaka, T. J., Sanchez, S., Saturnino, D., Schnepf, N. R., Shen, X., Stolle, C., Tangborn, A., Tøffner-Clausen, L., Toh, H., Torta, J. M., Varner, J., Vervelidou, F., Vigneron, P., Wardinski, I., Wicht, J., Woods, A., Yang, Y., Zeren, Z., and Zhou, B. (2021). International geomagnetic reference field: the thirteenth generation. *Earth, Planets and Space*, 73(1):49.

Angelopoulos, V., Cruce, P., Drozdov, A., Grimes, E. W., Hatzigeorgiu, N., King, D. A., Larson, D., Lewis, J. W., McTiernan, J. M., Roberts, D. A., Russell, C. L., Hori, T.,

Kasahara, Y., Kumamoto, A., Matsuoka, A., Miyashita, Y., Miyoshi, Y., Shinohara, I., Teramoto, M., Faden, J. B., Halford, A. J., McCarthy, M., Millan, R. M., Sample, J. G., Smith, D. M., Woodger, L. A., Masson, A., Narock, A. A., Asamura, K., Chang, T. F., Chiang, C.-Y., Kazama, Y., Keika, K., Matsuda, S., Segawa, T., Seki, K., Shoji, M., Tam, S. W. Y., Umemura, N., Wang, B.-J., Wang, S.-Y., Redmon, R., Rodriguez, J. V., Singer, H. J., Vandegriff, J., Abe, S., Nose, M., Shinbori, A., Tanaka, Y.-M., UeNo, S., Andersson, L., Dunn, P., Fowler, C., Halekas, J. S., Hara, T., Harada, Y., Lee, C. O., Lillis, R., Mitchell, D. L., Argall, M. R., Bromund, K., Burch, J. L., Cohen, I. J., Galloy, M., Giles, B., Jaynes, A. N., Le Contel, O., Oka, M., Phan, T. D., Walsh, B. M., Westlake, J., Wilder, F. D., Bale, S. D., Livi, R., Pulupa, M., Whittlesey, P., DeWolfe, A., Harter, B., Lucas, E., Auster, U., Bonnell, J. W., Cully, C. M., Donovan, E., Ergun, R. E., Frey, H. U., Jackel, B., Keiling, A., Korth, H., McFadden, J. P., Nishimura, Y., Plaschke, F., Robert, P., Turner, D. L., Weygand, J. M., Candey, R. M., Johnson, R. C., Kovalick, T., Liu, M. H., McGuire, R. E., Breneman, A., Kersten, K., and Schroeder, P. (2019). The space physics environment data analysis system (spedas). *Space Science Reviews*, 215(1):9.

Araki, T. (1994). *A Physical Model of the Geomagnetic Sudden Commencement*, pages 183–200. American Geophysical Union (AGU).

Bartels, J. (1949). The standardized index, ks, and the planetary index, kp. *IATME Bull.*, 12b:97–120.

Baschin, O. (1900). Die ersten nordlichtphotographien etc. *Met. Z.*, 17.

Bilitza, D. (1997). International reference ionosphere—status 1995/96. *Advances in Space Research*, 20(9):1751–1754. Quantitive Description of Ionospheric Storm Effects and Irregularities.

Birkeland, K. (1913). *The Norwegian Aurora Polaris Expedition 1902–1903*. Number 1 in The Norwegian Aurora Polaris Expedition 1902–1903. H. Aschehoug & Company.

Blackie, J. (1964). *Analysis of auroral observations, Halley Bay, 1960*, volume 40 of *British Antarctic Survey Scientific Reports*. British Antarctic Survey, London.

Bland, E. C., Partamies, N., Heino, E., Yukimatu, A. S., and Miyaoka, H. (2019). Energetic electron precipitation occurrence rates determined using the syowa east superdarn radar. *Journal of Geophysical Research: Space Physics*, 124(7):6253–6265.

Blundell, G. (1967). *Analysis of auroral observations, Halley Bay, 1961 and 1962*, volume 48 of *British Antarctic Survey Scientific Reports*. British Antarctic Survey, London.

Brändström, U. (2003). *The Auroral Large Imaging System—Design, Operation and Scientific Results*. PhD thesis, Swedish Institute of Space Physics (IRF).

Brekke, A. (1997). *Physics of the Upper Polar Atmosphere*. John Wiley & Sons Ltd, Hoboken, N. J.

Broadfoot, A. L. and Bellaire Jr., P. J. (1999). Bridging the gap between ground-based and space-based observations of the night airglow. *Journal of Geophysical Research: Space Physics*, 104(A8):17127–17138.

Brown, N. B., Davis, T. N., Hallinan, T. J., and Stenbaek-Nielsen, H. C. (1976). Altitude of pulsating aurora determined by a new instrumental technique. *Geophysical Research Letters*, 3(7):403–404.

Bryce, B. (1976). Color imaging array.

Chollet, F. et al. (2015). Keras. `https://github.com/fchollet/keras`.

Chu, X., Wolter, L., Malaspina, D., Andersson, L., Connors, M., Chatfield, C., and Zeller, N. (2020). Morphological characteristics of strong thermal emission velocity enhancement emissions. *Journal of Geophysical Research: Space Physics*, 125(12):e2020JA028110. e2020JA028110 2020JA028110.

Clausen, L. B. N. and Nickisch, H. (2018). Automatic classification of auroral images from the oslo auroral themis (oath) data set using machine learning. *Journal of Geophysical Research: Space Physics*, 123(7):5640–5647.

Cortie, A. L., S. (1912). Sun-spots and terrestrial magnetic phenomena, 1898–1911: the cause of the annual variation in magnetic disturbances. *Monthly Notices of the Royal Astronomical Society*, 73(1):52–60.

Craven, J. D., Frank, L. A., Russell, C. T., Smith, E. J., and Lepping, R. P. (1986). *The Global Auroral Responses to Magnetospheric Compressions by Shocks in the Solar Wind: Two Case Studies*, pages 367–380. Tokyo.

Daubechies, I. (1990). The wavelet transform, time-frequency localization and signal analysis. *IEEE Transactions on Information Theory*, 36(5):961–1005.

Davidson, G. (1979). Self-modulated vlf wave-electron interactions in the magnetosphere: A cause of auroral pulsations. *Journal of Geophysical Research: Space Physics*, 84(A11):6517–6523.

Davis, T. N. and Sugiura, M. (1966). Auroral electrojet activity index ae and its universal time variations. *Journal of Geophysical Research (1896-1977)*, 71(3):785–801.

de Miguel, A. S., Kyba, C. C., Aubé, M., Zamorano, J., Cardiel, N., Tapia, C., Bennie, J., and Gaston, K. J. (2019). Colour remote sensing of the impact of artificial light at night (i): The potential of the international space station and other dslr-based platforms. *Remote Sensing of Environment*, 224:92–103.

Demekhov, A. G. and Trakhtengerts, V. Y. (1994). A mechanism of formation of pulsating aurorae. *Journal of Geophysical Research: Space Physics*, 99(A4):5831–5841.

Deng, J., Dong, W., Socher, R., Li, L.-J., Li, K., and Fei-Fei, L. (2009). Imagenet: A large-scale hierarchical image database. In *2009 IEEE Conference on Computer Vision and Pattern Recognition*, pages 248–255.

Duncan, C. N., Creutzberg, F., Gattinger, R. L., Harris, F. R., and Jones, A. V. (1981). Latitudinal and temporal characteristics of pulsating auroras. *Canadian Journal of Physics*, 59(8):1063–1069.

Eddy, J. A. (1976). The maunder minimum. *Science*, 192(4245):1189–1202.

Elphinstone, R. D., Murphree, J. S., Hearn, D. J., Cogger, L. L., Sandahl, I., Newell, P. T., Klumpar, D. M., Ohtani, S., Sauvaud, J. A., Potemra, T. A., Mursula, K., Wright, A., and Shapshak, M. (1995). The double oval uv auroral distribution: 1. implications for the mapping of auroral arcs. *Journal of Geophysical Research: Space Physics*, 100(A7):12075–12092.

Evans, D. S., Davidson, G. T., Voss, H. D., Imhof, W. L., Mobilia, J., and Chiu, Y. T. (1987). Interpretation of electron spectra in morningside pulsating aurorae. *Journal of Geophysical Research: Space Physics*, 92(A11):12295–12306.

Frank, L. A. and Ackerson, K. L. (1971). Observations of charged particle precipitation into the auroral zone. *Journal of Geophysical Research (1896-1977)*, 76(16):3612–3643.

Fu, R., Li, J., Gao, X., and Jian, Y. (2009). Automatic aurora images classification algorithm based on separated texture. In *2009 IEEE International Conference on Robotics and Biomimetics (ROBIO)*, pages 1331–1335.

Fukizawa, M., Sakanoi, T., Miyoshi, Y., Hosokawa, K., Shiokawa, K., Katoh, Y., Kazama, Y., Kumamoto, A., Tsuchiya, F., Miyashita, Y., Tanaka, Y. M., Kasahara, Y., Ozaki, M., Matsuoka, A., Matsuda, S., Hikishima, M., Oyama, S., Ogawa, Y., Kurita, S., and Fujii, R. (2018). Electrostatic electron cyclotron harmonic waves as a candidate to cause pulsating auroras. *Geophysical Research Letters*, 45(23):12,661–12,668.

Fukizawa, M., Sakanoi, T., Miyoshi, Y., Kazama, Y., Katoh, Y., Kasahara, Y., Matsuda, S., Matsuoka, A., Kurita, S., Shoji, M., Teramoto, M., Imajo, S., Sinohara, I., Wang, S.-Y., Tam, S. W.-Y., Chang, T.-F., Wang, B.-J., and Jun, C.-W. (2020). Pitch-angle scattering of inner magnetospheric electrons caused by ech waves obtained with the arase satellite. *Geophysical Research Letters*, 47(23):e2020GL089926. e2020GL089926 2020GL089926.

Gao, X., Chen, R., Lu, Q., Chen, L., Chen, H., and Wang, X. (2022). Observational evidence for the origin of repetitive chorus emissions. *Geophysical Research Letters*, 49(12):e2022GL099000. e2022GL099000 2022GL099000.

Gillies, D. M., Knudsen, D. J., Donovan, E. F., Spanswick, E. L., Hansen, C., Keating, D., and Erion, S. (2014). A survey of quiet auroral arc orientation and the effects of the interplanetary magnetic field. *Journal of Geophysical Research: Space Physics*, 119(4):2550–2562.

Gjerloev, J. W. (2012). The supermag data processing technique. *Journal of Geophysical Research: Space Physics*, 117(A9).

Grandin, M., Kero, A., Partamies, N., McKay, D., Whiter, D., Kozlovsky, A., and Miyoshi, Y. (2017). Observation of pulsating aurora signatures in cosmic noise absorption data. *Geophysical Research Letters*, 44(11):5292–5300.

Grono, E. and Donovan, E. (2018). Differentiating diffuse auroras based on phenomenology. *Annales Geophysicae*, 36(3):891–898.

Gurnett, D. A. (1972). Electric field and plasma observations in the magnetosphere. *Critical Problems of Magnetospheric Physics*, pages 123–138.

Gurnett, D. A. and Frank, L. A. (1973). Observed relationships between electric fields and auroral particle precipitation. *Journal of Geophysical Research (1896-1977)*, 78(1):145–170.

He, K., Zhang, X., Ren, S., and Sun, J. (2016). Deep residual learning for image recognition. In *2016 IEEE Conference on Computer Vision and Pattern Recognition (CVPR)*, pages 770–778.

Hedin, A. E. (1991). Extension of the msis thermosphere model into the middle and lower atmosphere. *Journal of Geophysical Research: Space Physics*, 96(A2):1159–1172.

Hikishima, M., Yagitani, S., Omura, Y., and Nagano, I. (2009). Full particle simulation of whistler-mode rising chorus emissions in the magnetosphere. *Journal of Geophysical Research: Space Physics*, 114(A1).

Holmes, J. M., Johnsen, M. G., Deehr, C. S., Zhou, X.-Y., and Lorentzen, D. A. (2014). Circumpolar ground-based optical measurements of proton and electron shock aurora. *Journal of Geophysical Research: Space Physics*, 119(5):3895–3914.

Hosokawa, K. (2002). *Observational Studies on the High-Latitude Ionospheric Plasma Irregularities*. PhD thesis, Kyoto University.

Hosokawa, K., Miyoshi, Y., Ozaki, M., Oyama, S.-I., Ogawa, Y., Kurita, S., Kasahara, Y., Kasaba, Y., Yagitani, S., Matsuda, S., Tsuchiya, F., Kumamoto, A., Kataoka, R., Shiokawa, K., Raita, T., Turunen, E., Takashima, T., Shinohara, I., and Fujii, R. (2020). Multiple time-scale beats in aurora: precise orchestration via magnetospheric chorus waves. *Scientific Reports*, 10(1):3380.

Hosokawa, K. and Ogawa, Y. (2015). Ionospheric variation during pulsating aurora. *Journal of Geophysical Research: Space Physics*, 120(7):5943–5957.

Hosokawa, K., Oyama, S.-I., Ogawa, Y., Miyoshi, Y., Kurita, S., Teramoto, M., Nozawa, S., Kawabata, T., Kawamura, Y., Tanaka, Y.-M., Miyaoka, H., Kataoka, R., Shiokawa, K., Brändström, U., Turunen, E., Raita, T., Johnsen, M. G., Hall, C., Hampton, D., Ebihara, Y., Kasahara, Y., Matsuda, S., Shinohara, I., and Fujii, R. (2023). A ground-based instrument suite for integrated high-time resolution measurements of pulsating aurora with arase. *Journal of Geophysical Research: Space Physics*, 128(8):e2023JA031527. e2023JA031527 2023JA031527.

Hozumi, Y., Saito, A., and Ejiri, M. K. (2016). Calibration of imaging parameters for space-borne airglow photography using city light positions. *Earth, Planets and Space*, 68(1):155.

Humberset, B. K., Gjerloev, J. W., Mann, I. R., Michell, R. G., and Samara, M. (2018). On the persistent shape and coherence of pulsating auroral patches. *Journal of Geophysical Research: Space Physics*, 123(5):4272–4289.

Hutchinson, J. A., Wright, D. M., and Milan, S. E. (2011). Geomagnetic storms over the last solar cycle: A superposed epoch analysis. *Journal of Geophysical Research: Space Physics*, 116(A9).

Iyemori, T. and Rao, D. R. K. (1996). Decay of the dst field of geomagnetic disturbance after substorm onset and its implication to storm-substorm relation. *Annales Geophysicae*, 14(6):608–618.

Jaynes, A. N., Lessard, M. R., Rodriguez, J. V., Donovan, E., Loto'aniu, T. M., and Rychert, K. (2013). Pulsating auroral electron flux modulations in the equatorial magnetosphere. *Journal of Geophysical Research: Space Physics*, 118(8):4884–4894.

Jia, Z., Han, B., and Gao, X. (2015). 2dpcanet: Dayside aurora classification based on deep learning. In Zha, H., Chen, X., Wang, L., and Miao, Q., editors, *Computer Vision*, pages 323–334, Berlin, Heidelberg. Springer Berlin Heidelberg.

Jones, A. V. (1971). Auroral Spectroscopy. *Space Science Reviews*, 11(6):776–826.

Jones, A. V. (1974). *Aurora*, volume 9 of *Geophysics and astrophysics monographs*. Springer, Dordrecht.

Jones, S., Lessard, M., Fernandes, P., Lummerzheim, D., Semeter, J., Heinselman, C., Lynch, K., Michell, R., Kintner, P., Stenbaek-Nielsen, H., and Asamura, K. (2009). Pfisr and ropa observations of pulsating aurora. *Journal of Atmospheric and Solar-Terrestrial Physics*, 71(6):708–716. Advances in high latitude upper atmospheric science with the Poker Flat Incoherent Scatter Radar (PFISR).

Jones, S. L., Lessard, M. R., Rychert, K., Spanswick, E., and Donovan, E. (2011). Large-scale aspects and temporal evolution of pulsating aurora. *Journal of Geophysical Research: Space Physics*, 116(A3).

Jones, S. L., Lessard, M. R., Rychert, K., Spanswick, E., Donovan, E., and Jaynes, A. N. (2013). Persistent, widespread pulsating aurora: A case study. *Journal of Geophysical Research: Space Physics*, 118(6):2998–3006.

Karlsson, T., Andersson, L., Gillies, D. M., Lynch, K., Marghitu, O., Partamies, N., Sivadas, N., and Wu, J. (2020). Quiet, discrete auroral arcs—observations. *Space Science Reviews*, 216(1):16.

Kasahara, S., Miyoshi, Y., Yokota, S., Mitani, T., Kasahara, Y., Matsuda, S., Kumamoto, A., Matsuoka, A., Kazama, Y., Frey, H. U., Angelopoulos, V., Kurita, S., Keika, K., Seki, K., and Shinohara, I. (2018a). Pulsating aurora from electron scattering by chorus waves. *Nature*, 554:337–340.

Kasahara, S., Yokota, S., Mitani, T., Asamura, K., Hirahara, M., Shibano, Y., and Takashima, T. (2018b). Medium-energy particle experiments—electron analyzer (mep-e) for the exploration of energization and radiation in geospace (erg) mission. *Earth, Planets and Space*, 70(1):69.

Kasahara, Y., Kasaba, Y., Kojima, H., Yagitani, S., Ishisaka, K., Kumamoto, A., Tsuchiya, F., Ozaki, M., Matsuda, S., Imachi, T., Miyoshi, Y., Hikishima, M., Katoh, Y., Ota, M., Shoji, M., Matsuoka, A., and Shinohara, I. (2018c). The plasma wave experiment (pwe) on board the arase (erg) satellite. *Earth, Planets and Space*, 70(1):86.

Kataoka, R., Miyoshi, Y., Shigematsu, K., Hampton, D., Mori, Y., Kubo, T., Yamashita, A., Tanaka, M., Takahei, T., Nakai, T., Miyahara, H., and Shiokawa, K. (2013). Stereoscopic determination of all-sky altitude map of aurora using two ground-based nikon dslr cameras. *Annales Geophysicae*, 31(9):1543–1548.

Katoh, Y. and Omura, Y. (2013). Effect of the background magnetic field inhomogeneity on generation processes of whistler-mode chorus and broadband hiss-like emissions. *Journal of Geophysical Research: Space Physics*, 118(7):4189–4198.

Katoh, Y., Omura, Y., Miyake, Y., Usui, H., and Nakashima, H. (2018). Dependence of generation of whistler mode chorus emissions on the temperature anisotropy and density of energetic electrons in the earth's inner magnetosphere. *Journal of Geophysical Research: Space Physics*, 123(2):1165–1177.

Kawamura, Y., Hosokawa, K., Nozawa, S., Ogawa, Y., Kawabata, T., Oyama, S.-I., Miyoshi, Y., Kurita, S., and Fujii, R. (2020). Estimation of the emission altitude of pulsating aurora using the five-wavelength photometer. *Earth, Planets and Space*, 72(1):96.

Kazama, Y., Wang, B.-J., Wang, S.-Y., Ho, P. T. P., Tam, S. W. Y., Chang, T.-F., Chiang, C.-Y., and Asamura, K. (2017). Low-energy particle experiments–electron analyzer (lepe) onboard the arase spacecraft. *Earth, Planets and Space*, 69(1):165.

Kennel, C. F. and Petschek, H. E. (1966). Limit on stably trapped particle fluxes. *Journal of Geophysical Research (1896-1977)*, 71(1):1–28.

Kikuchi, T. (2014). Transmission line model for the near-instantaneous transmission of the ionospheric electric field and currents to the equator. *Journal of Geophysical Research: Space Physics*, 119(2):1131–1156.

Kozlovsky, A., Safargaleev, V., Østgaard, N., Turunen, T., Koustov, A., Jussila, J., and Roldugin, A. (2005). On the motion of dayside auroras caused by a solar wind pressure pulse. *Annales Geophysicae*, 23(2):509–521.

Krassovsky, V. I., Shefov, N. N., and Yarin, V. I. (1962). Atlas of the airglow spectrum 3000–12400 å. *Planetary and Space Science*, 9(12).

Kumamoto, A., Tsuchiya, F., Kasahara, Y., Kasaba, Y., Kojima, H., Yagitani, S., Ishisaka, K., Imachi, T., Ozaki, M., Matsuda, S., Shoji, M., Matsuoka, A., Katoh, Y., Miyoshi, Y., and Obara, T. (2018). High frequency analyzer (hfa) of plasma wave experiment (pwe) onboard the arase spacecraft. *Earth, Planets and Space*, 70(1):82.

Kvammen, A., Wickstrøm, K., McKay, D., and Partamies, N. (2020). Auroral image classification with deep neural networks. *Journal of Geophysical Research: Space Physics*, 125(10):e2020JA027808. e2020JA027808 10.1029/2020JA027808.

Lang, D., Hogg, D. W., Mierle, K., Blanton, M., and Roweis, S. (2010). Astrometry.net: Blind astrometric calibration of arbitrary astronomical images. *The Astronomical Journal*, 139(5):1782.

Lessard, M. R. (2012). *A Review of Pulsating Aurora*, pages 55–68. American Geophysical Union (AGU).

Li, W., Bortnik, J., Thorne, R. M., Nishimura, Y., Angelopoulos, V., and Chen, L. (2011). Modulation of whistler mode chorus waves: 2. role of density variations. *Journal of Geophysical Research: Space Physics*, 116(A6).

Li, W., Thorne, R. M., Angelopoulos, V., Bortnik, J., Cully, C. M., Ni, B., LeContel, O., Roux, A., Auster, U., and Magnes, W. (2009). Global distribution of whistler-mode chorus waves observed on the themis spacecraft. *Geophysical Research Letters*, 36(9).

Liu, J. J., Hu, H. Q., Han, D. S., Araki, T., Hu, Z. J., Zhang, Q. H., Yang, H. G., Sato, N., Yukimatu, A. S., and Ebihara, Y. (2011). Decrease of auroral intensity associated with reversal of plasma convection in response to an interplanetary shock as observed over zhongshan station in antarctica. *Journal of Geophysical Research: Space Physics*, 116(A3).

Loewe, C. A. and Prölss, G. W. (1997). Classification and mean behavior of magnetic storms. *Journal of Geophysical Research: Space Physics*, 102(A7):14209–14213.

Lu, Q., Chen, L., Wang, X., Gao, X., Lin, Y., and Wang, S. (2021). Repetitive emissions of rising-tone chorus waves in the inner magnetosphere. *Geophysical Research Letters*, 48(15):e2021GL094979. e2021GL094979 2021GL094979.

MacDonald, E. A., Donovan, E., Nishimura, Y., Case, N. A., Gillies, D. M., Gallardo-Lacourt, B., Archer, W. E., Spanswick, E. L., Bourassa, N., Connors, M., Heavner, M., Jackel, B., Kosar, B., Knudsen, D. J., Ratzlaff, C., and Schofield, I. (2018). New science in plain sight: Citizen scientists lead to the discovery of optical structure in the upper atmosphere. *Science Advances*, 4(3).

Martinis, C., Griffin, I., Gallardo-Lacourt, B., Wroten, J., Nishimura, Y., Baumgardner, J., and Knudsen, D. J. (2022). Rainbow of the night: First direct observation of a sar arc evolving into steve. *Geophysical Research Letters*, 49(11):e2022GL098511. e2022GL098511 2022GL098511.

Matsuda, S., Kasahara, Y., Kojima, H., Kasaba, Y., Yagitani, S., Ozaki, M., Imachi, T., Ishisaka, K., Kumamoto, A., Tsuchiya, F., Ota, M., Kurita, S., Miyoshi, Y., Hikishima, M., Matsuoka, A., and Shinohara, I. (2018). Onboard software of plasma wave experiment aboard arase: instrument management and signal processing of waveform capture/onboard frequency analyzer. *Earth, Planets and Space*, 70(1):75.

Matsuoka, A., Teramoto, M., Nomura, R., Nosé, M., Fujimoto, A., Tanaka, Y., Shinohara, M., Nagatsuma, T., Shiokawa, K., Obana, Y., Miyoshi, Y., Mita, M., Takashima, T., and Shinohara, I. (2018). The arase (erg) magnetic field investigation. *Earth, Planets and Space*, 70(1):43.

McEwen, D. J., Duncan, C. N., and Montalbetti, R. (1981a). Auroral electron energies: comparisons of in situ measurements with spectroscopically inferred energies. *Canadian Journal of Physics*, 59(8):1116–1123.

McEwen, D. J., Yee, E., Whalen, B. A., and Yau, A. W. (1981b). Electron energy measurements in pulsating auroras. *Canadian Journal of Physics*, 59(8):1106–1115.

Mende, S. B., Harris, S. E., Frey, H. U., Angelopoulos, V., Russell, C. T., Donovan, E., Jackel, B., Greffen, M., and Peticolas, L. M. (2008). The themis array of ground-based observatories for the study of auroral substorms. *Space Science Reviews*, 141(1):357–387.

Meng, C.-I. and Liou, K. (2004). Substorm timings and timescales: A new aspect. *Space Science Reviews*, 113(1):41–75.

Millan, R. and Thorne, R. (2007). Review of radiation belt relativistic electron losses. *Journal of Atmospheric and Solar-Terrestrial Physics*, 69(3):362–377.

Miyoshi, Y., Hosokawa, K., Kurita, S., Oyama, S.-I., Ogawa, Y., Saito, S., Shinohara, I., Kero, A., Turunen, E., Verronen, P. T., Kasahara, S., Yokota, S., Mitani, T., Takashima, T., Higashio, N., Kasahara, Y., Matsuda, S., Tsuchiya, F., Kumamoto, A., Matsuoka, A., Hori, T., Keika, K., Shoji, M., Teramoto, M., Imajo, S., Jun, C., and Nakamura, S. (2021). Penetration of mev electrons into the mesosphere accompanying pulsating aurorae. *Scientific Reports*, 11(1):13724.

Miyoshi, Y., Katoh, Y., Nishiyama, T., Sakanoi, T., Asamura, K., and Hirahara, M. (2010). Time of flight analysis of pulsating aurora electrons, considering wave-particle interactions with propagating whistler mode waves. *Journal of Geophysical Research: Space Physics*, 115(A10).

Miyoshi, Y., Oyama, S., Saito, S., Kurita, S., Fujiwara, H., Kataoka, R., Ebihara, Y., Kletzing, C., Reeves, G., Santolik, O., Clilverd, M., Rodger, C. J., Turunen, E., and Tsuchiya, F. (2015a). Energetic electron precipitation associated with pulsating aurora: Eiscat and van allen probe observations. *Journal of Geophysical Research: Space Physics*, 120(4):2754–2766.

Miyoshi, Y., Saito, S., Kurita, S., Asamura, K., Hosokawa, K., Sakanoi, T., Mitani, T., Ogawa, Y., Oyama, S., Tsuchiya, F., Jones, S. L., Jaynes, A. N., and Blake, J. B. (2020). Relativistic electron microbursts as high-energy tail of pulsating aurora electrons. *Geophysical Research Letters*, 47(21):e2020GL090360. e2020GL090360 2020GL090360.

Miyoshi, Y., Saito, S., Seki, K., Nishiyama, T., Kataoka, R., Asamura, K., Katoh, Y., Ebihara, Y., Sakanoi, T., Hirahara, M., Oyama, S., Kurita, S., and Santolik, O. (2015b). Relation between fine structure of energy spectra for pulsating aurora electrons and frequency spectra of whistler mode chorus waves. *Journal of Geophysical Research: Space Physics*, 120(9):7728–7736.

Miyoshi, Y., Shinohara, I., Takashima, T., Asamura, K., Higashio, N., Mitani, T., Kasahara, S., Yokota, S., Kazama, Y., Wang, S.-Y., Tam, S. W. Y., Ho, P. T. P., Kasahara,

Y., Kasaba, Y., Yagitani, S., Matsuoka, A., Kojima, H., Katoh, Y., Shiokawa, K., and Seki, K. (2018). Geospace exploration project erg. *Earth, Planets and Space*, 70(1):101.

Motoba, T., Ebihara, Y., Kadokura, A., and Weatherwax, A. T. (2014). Fine-scale transient arcs seen in a shock aurora. *Journal of Geophysical Research: Space Physics*, 119(8):6249–6255.

Motoba, T., Kadokura, A., Ebihara, Y., Frey, H. U., Weatherwax, A. T., and Sato, N. (2009). Simultaneous ground-satellite optical observations of postnoon shock aurora in the southern hemisphere. *Journal of Geophysical Research: Space Physics*, 114(A7).

Mozer, F. S., Carlson, C. W., Hudson, M. K., Torbert, R. B., Parady, B., Yatteau, J., and Kelley, M. C. (1977). Observations of paired electrostatic shocks in the polar magnetosphere. *Phys. Rev. Lett.*, 38:292–295.

Mozer, F. S., Cattell, C. A., Hudson, M. K., Lysak, R. L., Temerin, M., and Torbert, R. B. (1980). Satellite measurements and theories of low altitude auroral particle acceleration. *Space Science Reviews*, 27(2):155–213.

Nanjo, S., Hozumi, Y., Hosokawa, K., Kataoka, R., Miyoshi, Y., Oyama, S.-i., Ozaki, M., Shiokawa, K., and Kurita, S. (2020). Fine-scale visualization of aurora in a wide area using color digital camera images from the international space station. *Journal of Geophysical Research: Space Physics*, 125(3):e2019JA027729.

Nanjo, S., Hozumi, Y., Hosokawa, K., Kataoka, R., Miyoshi, Y., Oyama, S.-i., Ozaki, M., Shiokawa, K., and Kurita, S. (2021). Periodicities and colors of pulsating auroras: Dslr camera observations from the international space station. *Journal of Geophysical Research: Space Physics*, 126(10):e2021JA029564. e2021JA029564 2021JA029564.

Nevanlinna, H. (1995). Auroral observations in finland-visual sightings during the 18th and 19th centuries. *Journal of geomagnetism and geoelectricity*, 47:953–960.

Nevanlinna, H. and Pulkkinen, T. I. (2001). Auroral observations in finland: Results from all-sky cameras, 1973–1997. *Journal of Geophysical Research: Space Physics*, 106(A5):8109–8118.

Newell, P. T. and Gjerloev, J. W. (2011). Evaluation of supermag auroral electrojet indices as indicators of substorms and auroral power. *Journal of Geophysical Research: Space Physics*, 116(A12).

Ni, B., Thorne, R., Liang, J., Angelopoulos, V., Cully, C., Li, W., Zhang, X., Hartinger, M., Le Contel, O., and Roux, A. (2011). Global distribution of electrostatic electron cyclotron harmonic waves observed on themis. *Geophysical Research Letters*, 38(17).

Nishimura, Y., Bortnik, J., Li, W., Liang, J., Thorne, R. M., Angelopoulos, V., Le Contel, O., Auster, U., and Bonnell, J. W. (2015). Chorus intensity modulation driven by time-varying field-aligned low-energy plasma. *Journal of Geophysical Research: Space Physics*, 120(9):7433–7446.

Nishimura, Y., Bortnik, J., Li, W., Thorne, R. M., Lyons, L. R., Angelopoulos, V., Mende, S. B., Bonnell, J. W., Le Contel, O., Cully, C., Ergun, R., and Auster, U. (2010). Identifying the driver of pulsating aurora. *Science*, 330(6000):81–84.

Nishimura, Y., Kikuchi, T., Ebihara, Y., Yoshikawa, A., Imajo, S., Li, W., and Utada, H. (2016). Evolution of the current system during solar wind pressure pulses based on aurora and magnetometer observations. *Earth, Planets and Space*, 68(1):144.

Nishimura, Y., Lessard, M. R., Katoh, Y., Miyoshi, Y., Grono, E., Partamies, N., Sivadas, N., Hosokawa, K., Fukizawa, M., Samara, M., Michell, R. G., Kataoka, R., Sakanoi, T., Whiter, D. K., Oyama, S.-i., Ogawa, Y., and Kurita, S. (2020). Diffuse and pulsating aurora. *Space Science Reviews*, 216(1):4.

Nishiyama, T., Sakanoi, T., Miyoshi, Y., Hampton, D. L., Katoh, Y., Kataoka, R., and Okano, S. (2014). Multiscale temporal variations of pulsating auroras: On-off pulsation and a few hz modulation. *Journal of Geophysical Research: Space Physics*, 119(5):3514–3527.

Nishiyama, T., Sakanoi, T., Miyoshi, Y., Katoh, Y., Asamura, K., Okano, S., and Hirahara, M. (2011). The source region and its characteristic of pulsating aurora based on the reimei observations. *Journal of Geophysical Research: Space Physics*, 116(A3).

Nozawa, S., Kawabata, T., Hosokawa, K., Ogawa, Y., Tsuda, T., Mizuno, A., Fujii, R., and Hall, C. (2018). A new five-wavelength photometer operated in Tromsø (69.6°N, 19.2°E). *Earth, Planets and Space*, 70(1):193.

Nozawa, S., Kawahara, T. D., Saito, N., Hall, C. M., Tsuda, T. T., Kawabata, T., Wada, S., Brekke, A., Takahashi, T., Fujiwara, H., Ogawa, Y., and Fujii, R. (2014). Variations of the neutral temperature and sodium density between 80 and 107 km above Tromsø during the winter of 2010–2011 by a new solid-state sodium lidar. *Journal of Geophysical Research: Space Physics*, 119(1):441–451.

Ogawa, Y., Kadokura, A., and Ejiri, M. (2020a). Optical calibration system of nipr for aurora and airglow observations. *Polar Science*, 26:100570.

Ogawa, Y., Tanaka, Y., Kadokura, A., Hosokawa, K., Ebihara, Y., Motoba, T., Gustavsson, B., Brändström, U., Sato, Y., Oyama, S., Ozaki, M., Raita, T., Sigernes, F., Nozawa, S., Shiokawa, K., Kosch, M., Kauristie, K., Hall, C., Suzuki, S., Miyoshi, Y., Gerrard, A., Miyaoka, H., and Fujii, R. (2020b). Development of low-cost multi-wavelength imager system for studies of aurora and airglow. *Polar Science*, 23:100501.

Omura, Y. (2021). Nonlinear wave growth theory of whistler-mode chorus and hiss emissions in the magnetosphere. *Earth, Planets and Space*, 73(1):95.

Ono, T. (1993). Derivation of energy parameters of precipitating auroral electrons by using the intensity ratios of auroral emissions. *Journal of geomagnetism and geoelectricity*, 45(6):455–472.

Ozaki, M., Miyoshi, Y., Shiokawa, K., Hosokawa, K., Oyama, S.-i., Kataoka, R., Ebihara, Y., Ogawa, Y., Kasahara, Y., Yagitani, S., Kasaba, Y., Kumamoto, A., Tsuchiya, F., Matsuda, S., Katoh, Y., Hikishima, M., Kurita, S., Otsuka, Y., Moore, R. C., Tanaka, Y., Nosé, M., Nagatsuma, T., Nishitani, N., Kadokura, A., Connors, M., Inoue, T., Matsuoka, A., and Shinohara, I. (2019). Visualization of rapid electron precipitation via chorus element wave–particle interactions. *Nature Communications*, 10(1):257.

Ozaki, M., Yagitani, S., Ishizaka, K., Shiokawa, K., Miyoshi, Y., Kadokura, A., Yamagishi, H., Kataoka, R., Ieda, A., Ebihara, Y., Sato, N., and Nagano, I. (2012). Observed

correlation between pulsating aurora and chorus waves at syowa station in antarctica: A case study. *Journal of Geophysical Research: Space Physics*, 117(A8).

Ozaki, M., Yagitani, S., Sawai, K., Shiokawa, K., Miyoshi, Y., Kataoka, R., Ieda, A., Ebihara, Y., Connors, M., Schofield, I., Katoh, Y., Otsuka, Y., Sunagawa, N., and Jordanova, V. K. (2015). A direct link between chorus emissions and pulsating aurora on timescales from milliseconds to minutes: A case study at subauroral latitudes. *Journal of Geophysical Research: Space Physics*, 120(11):9617–9631.

Palmroth, M., Grandin, M., Helin, M., Koski, P., Oksanen, A., Glad, M. A., Valonen, R., Saari, K., Bruus, E., Norberg, J., Viljanen, A., Kauristie, K., and Verronen, P. T. (2020). Citizen scientists discover a new auroral form: Dunes provide insight into the upper atmosphere. *AGU Advances*, 1(1):e2019AV000133. e2019AV000133 2019AV000133.

Partamies, N., Bolmgren, K., Heino, E., Ivchenko, N., Borovsky, J. E., and Sundberg, H. (2019). Patch size evolution during pulsating aurora. *Journal of Geophysical Research: Space Physics*, 124(6):4725–4738.

Partamies, N., Juusola, L., Whiter, D., and Kauristie, K. (2015). Substorm evolution of auroral structures. *Journal of Geophysical Research: Space Physics*, 120(7):5958–5972.

Partamies, N., Whiter, D., Kadokura, A., Kauristie, K., Nesse Tyssøy, H., Massetti, S., Stauning, P., and Raita, T. (2017). Occurrence and average behavior of pulsating aurora. *Journal of Geophysical Research: Space Physics*, 122(5):5606–5618.

Rangarajan, G. K. and Iyemori, T. (1997). Time variations of geomagnetic activity indices kp and ap: an update. *Annales Geophysicae*, 15(10):1271–1290.

Rao, J., Partamies, N., Amariutei, O., Syrjäsuo, M., and van de Sande, K. E. A. (2014). Automatic auroral detection in color all-sky camera images. *IEEE Journal of Selected Topics in Applied Earth Observations and Remote Sensing*, 7(12):4717–4725.

Rishbeth, H. and Williams, P. (1985). The eiscat ionospheric radar—the system and its early results. *Royal Astronomical Society, Quarterly Journal*, 26:478–512.

Royrvik, O. and Davis, T. N. (1977). Pulsating aurora: Local and global morphology. *Journal of Geophysical Research (1896-1977)*, 82(29):4720–4740.

Russell, C. T. and McPherron, R. L. (1973). Semiannual variation of geomagnetic activity. *Journal of Geophysical Research (1896-1977)*, 78(1):92–108.

Samara, M., Michell, R., and Hampton, D. (2012). Bg3 glass filter effects on quantifying rapidly pulsating auroral structures. *Advances in Remote Sensing*, 01:53–57.

Sandahl, I., Eliasson, L., and Lundin, R. (1980). Rocket observations of precipitating electrons over a pulsating aurora. *Geophysical Research Letters*, 7(5):309–312.

Sazhin, S. and Hayakawa, M. (1992). Magnetospheric chorus emissions: A review. *Planetary and Space Science*, 40(5):681–697.

Schröder, W. (1997). Some aspects of the earlier history of solar-terrestrial physics. *Planetary and Space Science*, 45(3):395–400.

Semeter, J., Hunnekuhl, M., MacDonald, E., Hirsch, M., Zeller, N., Chernenkoff, A., and Wang, J. (2020). The mysterious green streaks below steve. *AGU Advances*, 1(4):e2020AV000183. e2020AV000183 10.1029/2020AV000183.

Semeter, J., Lummerzheim, D., and Haerendel, G. (2001). Simultaneous multispectral imaging of the discrete aurora. *Journal of Atmospheric and Solar-Terrestrial Physics*, 63(18):1981–1992.

Shepherd, S. G. (2014). Altitude-adjusted corrected geomagnetic coordinates: Definition and functional approximations. *Journal of Geophysical Research: Space Physics*, 119(9):7501–7521.

Sheret, M. (1963). *Analysis of auroral observations, Halley Bay, 1959*, volume 37 of *British Antarctic Survey Scientific Reports*. British Antarctic Survey, London.

Shiokawa, K., Katoh, Y., Satoh, M., Ejiri, M. K., Ogawa, T., Nakamura, T., Tsuda, T., and Wiens, R. H. (1999). Development of optical mesosphere thermosphere imagers (omti). *Earth, Planets and Space*, 51(7):887–896.

Shiokawa, K., Otsuka, Y., and Connors, M. (2019). Statistical study of auroral/resonant-scattering 427.8-nm emission observed at subauroral latitudes over 14 years. *Journal of Geophysical Research: Space Physics*, 124(11):9293–9301.

Shiokawa, K., Ozaki, M., Kadokura, A., Endo, Y., Sakanoi, T., Kurita, S., Miyoshi, Y., Oyama, S.-I., Connors, M., Schofield, I., Ruohoniemi, J. M., Nosé, M., Nagatsuma, T., Sakaguchi, K., Baishev, D. G., Pashinin, A., Rakhmatulin, R., Shevtsov, B., Poddelsky, I., Engebretson, M., Raita, T., Tanaka, Y.-M., Shinohara, M., Teramoto, M., Nomura, R., Fujimoto, A., Matsuoka, A., Higashio, N., Takashima, T., Shinohara, I., and Albert, J. M. (2018). Purple auroral rays and global pc1 pulsations observed at the cir-associated solar wind density enhancement on 21 march 2017. *Geophysical Research Letters*, 45(20):10,819–10,828.

Sigernes, F., Holmes, J. M., Dyrland, M., Lorentzen, D. A., Svenøe, T., Heia, K., Aso, T., Chernouss, S., and Deehr, C. S. (2008). Sensitivity calibration of digital colour cameras for auroral imaging. *Opt. Express*, 16(20):15623–15632.

Silverman, S. M. (1992). Secular variation of the aurora for the past 500 years. *Reviews of Geophysics*, 30(4):333–351.

Steele, D. P. and McEwen, D. J. (1990). Electron auroral excitation efficiencies and intensity ratios. *Journal of Geophysical Research: Space Physics*, 95(A7):10321–10336.

Stenbaek-Nielsen, H. C., Hallinan, T. J., Osborne, D. L., Kimball, J., Chaston, C., McFadden, J., Delory, G., Temerin, M., and Carlson, C. W. (1998). Aircraft observations conjugate to fast: Auroral are thicknesses. *Geophysical Research Letters*, 25(12):2073–2076.

Stoffregen, W. (1956). *An all-sky camera for auroral research, description and operational manual*. Tech. rep., Uppsala Jonosfärsobservatorium.

Sugiura, M. (1964). Hourly values of equatorial dst for the igy. *Ann. Int. Geophys. Yr.*, 35.

Syrjäsuo, M. and Donovan, E. (2002). Analysis of auroral images: Detection and tracking. *Geophysica*, 38.

Syrjäsuo, M., Pulkkinen, T. I., Janhunen, P., Viljanen, A., Pellinen, R., Kauristie, K., Opgenoorth, H. J., Wallman, S., Eglitis, P., Karlsson, P., Amm, O., Nielsen, E., and

Thomas, C. (1998). Observations of substorm electrodynamics using the miracle network.

Syrjäsuo, M. T. and Donovan, E. F. (2004). Diurnal auroral occurrence statistics obtained via machine vision. *Annales Geophysicae*, 22(4):1103–1113.

Tagirov, V. (1993). Auroral torch structures: results of optical observations. *Journal of Atmospheric and Terrestrial Physics*, 55(14):1775–1787.

Tesema, F., Partamies, N., Tyssøy, H. N., Kero, A., and Smith-Johnsen, C. (2020). Observations of electron precipitation during pulsating aurora and its chemical impact. *Journal of Geophysical Research: Space Physics*, 125(6):e2019JA027713. e2019JA027713 10.1029/2019JA027713.

Thomas, R. W. and Rothwell, P. (1979). A latitude effect in the periodicity of auroral pulsating patches. *Journal of Atmospheric and Terrestrial Physics*, 41:1179–1184.

Thorne, R. M., Ni, B., Tao, X., Horne, R. B., and Meredith, N. P. (2010). Scattering by chorus waves as the dominant cause of diffuse auroral precipitation. *Nature*, 467(7318):943–946.

Tsuda, T. T., Nozawa, S., Kawahara, T. D., Kawabata, T., Saito, N., Wada, S., Hall, C. M., Tsutsumi, M., Ogawa, Y., Oyama, S., Takahashi, T., Ejiri, M. K., Nishiyama, T., Nakamura, T., and Brekke, A. (2015). A sporadic sodium layer event detected with five-directional lidar and simultaneous wind, electron density, and electric field observation at Tromsø, Norway. *Geophysical Research Letters*, 42(21):9190–9196.

Tsuda, T. T., Nozawa, S., Kawahara, T. D., Kawabata, T., Saito, N., Wada, S., Ogawa, Y., Oyama, S., Hall, C. M., Tsutsumi, M., Ejiri, M. K., Suzuki, S., Takahashi, T., and Nakamura, T. (2013). Decrease in sodium density observed during auroral particle precipitation over Tromsø, Norway. *Geophysical Research Letters*, 40(17):4486–4490.

Tsuruda, K., Machida, S., Oguti, T., Kokubun, S., Hayashi, K., Kitamura, T., Saka, O., and Watanabe, T. (1981). Correlations between the very low frequency chorus and pulsating aurora observed by low-light-level television at l=4.4. *Canadian Journal of Physics*, 59(8):1042–1048.

Tsurutani, B. T. and Smith, E. J. (1974). Postmidnight chorus: A substorm phenomenon. *Journal of Geophysical Research (1896-1977)*, 79(1):118–127.

Tsurutani, B. T. and Smith, E. J. (1977). Two types of magnetospheric elf chorus and their substorm dependences. *Journal of Geophysical Research (1896-1977)*, 82(32):5112–5128.

Tsurutani, B. T., Zank, G. P., Sterken, V. J., Shibata, K., Nagai, T., Mannucci, A. J., Malaspina, D. M., Lakhina, G. S., Kanekal, S. G., Hosokawa, K., Horne, R. B., Hajra, R., Glassmeier, K.-H., Gaunt, C. T., Chen, P.-F., and Akasofu, S.-I. (2023). Space plasma physics: A review. *IEEE Transactions on Plasma Science*, 51(7):1595–1655.

Tsyganenko, N. A. and Sitnov, M. I. (2005). Modeling the dynamics of the inner magnetosphere during strong geomagnetic storms. *Journal of Geophysical Research: Space Physics*, 110(A3).

Turunen, E., Kero, A., Verronen, P. T., Miyoshi, Y., Oyama, S.-I., and Saito, S. (2016). Mesospheric ozone destruction by high-energy electron precipitation associated with pulsating aurora. *Journal of Geophysical Research: Atmospheres*, 121(19):11,852–11,861.

Wang, Q., Liang, J., Hu, Z.-J., Hu, H.-H., Zhao, H., Hu, H.-Q., Gao, X., and Yang, H. (2010). Spatial texture based automatic classification of dayside aurora in all-sky images. *Journal of Atmospheric and Solar-Terrestrial Physics*, 72(5):498–508.

Yamamoto, T. (1988). On the temporal fluctuations of pulsating auroral luminosity. *Journal of Geophysical Research: Space Physics*, 93(A2):897–911.

Yamashina, S., Saito, A., Sakanoi, T., Tsuda, T. T., Takeshi, A., Ejiri, K. M., Nishiyama, T., Hozumi, Y., Naoi, T., and Nagahara, M. (2022). Observations of the ionosphere by the imager onboard the antarctic research vessel "shirase". In *Japan Geoscience Union Meeting 2022*.

Yang, Q., Liang, J., Hu, Z., and Zhao, H. (2012). Auroral sequence representation and classification using hidden markov models. *IEEE Transactions on Geoscience and Remote Sensing*, 50(12):5049–5060.

Zhong, Y., Huang, R., Zhao, J., Zhao, B., and Liu, T. (2018). Aurora image classification based on multi-feature latent dirichlet allocation. *Remote Sensing*, 10(2).

Zhou, X., Strangeway, R. J., Anderson, P. C., Sibeck, D. G., Tsurutani, B. T., Haerendel, G., Frey, H. U., and Arballo, J. K. (2003). Shock aurora: Fast and dmsp observations. *Journal of Geophysical Research: Space Physics*, 108(A4).

Zhou, X. and Tsurutani, B. T. (1999). Rapid intensification and propagation of the dayside aurora: Large scale interplanetary pressure pulses (fast shocks). *Geophysical Research Letters*, 26(8):1097–1100.

Zhou, X.-Y., Fukui, K., Carlson, H. C., Moen, J. I., and Strangeway, R. J. (2009). Shock aurora: Ground-based imager observations. *Journal of Geophysical Research: Space Physics*, 114(A12).